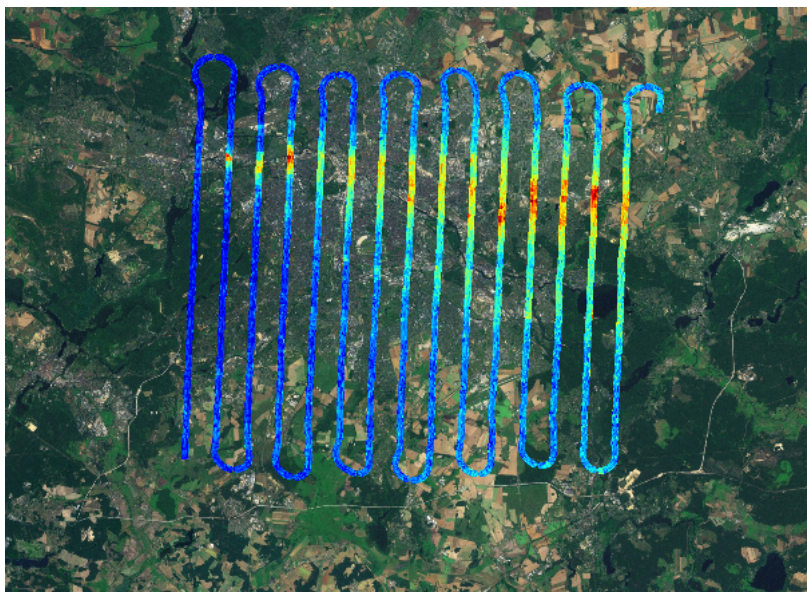


**THE RETRIEVAL OF TROPOSPHERIC NO<sub>2</sub> VERTICAL  
COLUMN DENSITY FROM SPECTROLITE  
MEASUREMENTS OVER BERLIN**



# THE RETRIEVAL OF TROPOSPHERIC NO<sub>2</sub> VERTICAL COLUMN DENSITY FROM SPECTROLITE MEASUREMENTS OVER BERLIN



**Xinrui GE**

to obtain the degree of Master of Science  
at the Delft University of Technology,  
to be defended publicly on Wednesday 16 November, 2016 at 1:00 PM.

Student number: 4403675  
Project duration: December 1, 2015 – November 15, 2016  
Thesis committee: Dr. T. Vlemmix, TU Delft, Supervisor  
Prof. dr. M. Menenti, TU Delft  
Prof. dr. P. F. Levelt, TU Delft, Committee Chair

An electronic version of this thesis is available at <http://repository.tudelft.nl/>.





# ACKNOWLEDGMENT

This graduation thesis symbolizes the end of my study of Geoscience and Remote Sensing at Delft University of Technology. During the 2-year master program, I have deepened my interest in atmospheric remote sensing and determined to continue working on this field. The graduation project has truly reflected my knowledge of atmospheric science and observation obtained in the master program. It provides a prototype to process Level 1B Spectrolite spectral measurements to NO<sub>2</sub> vertical columns. The results give confidence for the development of the instrument and offer the outlook of algorithm improvement for further study.

I would like to take the opportunity to thank some people involved in this project that offered me generous help. First and foremost, I would like to thank my daily supervisor Dr. Tim Vlemmix. He is the one who provided me with the possibility to work on the field of atmospheric remote sensing and the opportunity to meet all the researchers and engineers who share the same interest. He gives me guidance with the greatest patience throughout the project and always makes valuable critiques and suggestions to inspire me to explore the solution with innovation. Then, I would like to thank Ping Wang from KNMI for sharing her knowledge and experience of working with the radiative transfer model DAK. She patiently spent several meetings with me to go through the inputs of DAK to make sure that the settings are correctly, especially when it was the first time that I used this model. Furthermore, I would like to thank Bryan de Goeij from TNO, he provided me with the Level 1B Spectrolite radiance data and introduced the algorithm to obtain it and the overview of the AROMAPEX campaign. Besides, I would like to thank Len van der Wal from TNO to offer me a cloud platform to process the huge amount of data, which increased the efficiency to a large extent and saved a lot of time during the project. At last, I would specially thank Alexis Merlaud from Belgian Institute for Space Aeronomy and Andreas Meier from University of Bremen who offered AirMap and SWING data obtained at the same time with Spectrolite for comparisons.

Of course this acknowledgment would not be complete if I do not thank my parents and share my profound gratitude to them for providing me with unfailing support and continuous encouragement throughout my study. This accomplishment would not have been possible without them.



# ABSTRACT

Air pollution has become one of the most serious problems societies worldwide are facing, thus there is an emergent need for air quality monitoring to quantify pollution level and supervise pollution sources. One of the main pollutants, nitrogen dioxide, mostly comes from human activities such as the burning of fossil fuels, vehicle exhaust and electricity generation by power stations. In recent years, methods have been successfully developed and widely applied to monitor trace gases by measuring the vertical column density from space-borne satellites or ground-base stations. Recently, airborne observation for tropospheric trace gases column densities has become more and more popular, providing unique high spatial resolution observations that can be used for emission monitoring and for validation of satellite or ground-based observations. The Netherlands Organization for Applied Scientific Research (TNO) has developed *Spectrolite*, a compact, low cost hyperspectral imaging spectrometer based on the technological heritage from TROPOspheric Monitoring Instrument (TROPOMI).

In this project, an algorithm was developed to retrieve tropospheric NO<sub>2</sub> vertical column densities from Spectrolite spectral observations during the AROMAPEX campaign in Berlin on 21 April, 2016. We apply Differential Optical Absorption Spectroscopy (DOAS) approach to obtain differential slant column densities (dSCDs) from spectral measurements. Afterwards, a look-up table which contains radiances output as function of various parameters was derived from radiative transfer model to compute air mass factors (AMFs). However, since we do not know the surface reflectance during the measurements, Landsat observations over a homogeneous region are utilized for vicarious calibration of radiances and this allows us to retrieve surface reflectance needed for AMF calculations. Subsequently, OMI data is used in order to determine tropospheric background and to correct for effects related to stratospheric NO<sub>2</sub>.

Results of the dSCD retrieval show a pronounced NO<sub>2</sub> plume over Berlin stretching out from West to East over the city. Several hot spots can be observed and related to emission sources on the ground. They also acquire a good correspondence with the dSCDs retrieved by other instruments (AirMap, SWING) at the same time during the campaign and therefore give much confidence for the future development at TNO. In order to obtain VCDs, AMFs were derived using complementary observations for some parameters (e.g. aerosol optical). Sensitivity studies were performed to assess the impact on the retrieval accuracy of other parameters. It can come to a conclusion that aerosol and NO<sub>2</sub> vertical profiles are very essential to the VCD retrieval and need to be more well-defined in order to provide precise VCD results in absolute magnitude.

Xinrui Ge  
Delft, November 2016



# CONTENTS

<b>1</b>	<b>Introduction</b>	<b>1</b>
1.1	Air Pollution Monitoring . . . . .	2
1.2	Criteria Pollutants and Nitrogen Dioxide . . . . .	3
1.3	Concentration, Volume Mixing Ratio and Column Density . . . . .	3
1.4	Common Methods Used for NO <sub>2</sub> VCD Retrieval. . . . .	5
1.4.1	Space-borne Observation . . . . .	5
1.4.2	Ground-base Measurement . . . . .	6
1.4.3	Airborne Measurement . . . . .	6
1.5	Research Question . . . . .	7
<b>2</b>	<b>Spectrolite Instrument and AROMAPEX Campaign</b>	<b>11</b>
2.1	Spectrolite Instrument . . . . .	11
2.2	Level 0-1B Data Processing . . . . .	12
2.3	AROMAPEX Campaign . . . . .	13
<b>3</b>	<b>Methodology</b>	<b>15</b>
3.1	DOAS Fitting and Differential Slant Column Density . . . . .	16
3.2	Air Mass Factor . . . . .	19
3.2.1	Radiative Transfer Model. . . . .	20
3.2.2	Calculation of Air Mass Factor from DAK Look-up Table . . . . .	21
<b>4</b>	<b>Generation of DAK LUT and Sensitivity Study</b>	<b>25</b>
4.1	Input Parameters . . . . .	26
4.2	Parameters Settings. . . . .	27
4.2.1	Wavelength . . . . .	27
4.2.2	Altitude . . . . .	29
4.2.3	Atmospheric Profile . . . . .	30
4.2.4	Aerosol Profile . . . . .	32
4.2.5	Geometry . . . . .	35
4.2.6	Surface Reflectance . . . . .	37
4.3	Overview of Input Parameters. . . . .	37
4.4	Sensitivity Study in Radiance Output . . . . .	38
4.4.1	Geometry . . . . .	38
4.4.2	Surface Reflectance . . . . .	40
4.4.3	Aerosol Profile . . . . .	40
4.5	Sensitivity Study in Box-AMF . . . . .	43
4.5.1	Geometry . . . . .	43
4.5.2	Surface Reflectance . . . . .	46
4.5.3	Aerosol Profile . . . . .	46
4.5.4	Surface Temperature. . . . .	47

<b>5</b>	<b>Data Processing Chain</b>	<b>51</b>
5.1	Flow Charts of Data Processing Chain . . . . .	52
5.2	Spectrolite Data Processing . . . . .	54
5.2.1	Georeferencing and Data Gridding . . . . .	55
5.2.2	Differential Slant Column Density Retrieval . . . . .	64
5.3	Calculation of Solar Zenith Angle . . . . .	69
5.4	Calculation of Scaled Surface Reflectance . . . . .	71
5.4.1	Landsat Image Processing . . . . .	72
5.4.2	Calculation of Radiance Scaling Factor . . . . .	75
5.5	Calculation of Air Mass Factor . . . . .	79
5.6	Stratospheric Correction . . . . .	80
5.7	Retrieval of Tropospheric Vertical Column Density . . . . .	81
<b>6</b>	<b>Results</b>	<b>87</b>
6.1	Visualization and Interpretation . . . . .	88
6.1.1	Differential Slant Column Density . . . . .	88
6.1.2	Scaled Surface Reflectance . . . . .	92
6.1.3	Air Mass Factor . . . . .	97
6.1.4	Vertical Column Density . . . . .	103
6.2	Uncertainty Study . . . . .	105
<b>7</b>	<b>Conclusion and Outlook</b>	<b>113</b>
7.1	Conclusion . . . . .	113
7.2	Outlook . . . . .	114
	<b>References</b>	<b>117</b>
<b>A</b>	<b>Visualization of Scaled Surface Reflectance</b>	<b>121</b>
<b>B</b>	<b>Visualization of Air Mass Factor</b>	<b>127</b>
<b>C</b>	<b>Visualization of NO<sub>2</sub> Vertical Column Density</b>	<b>137</b>

# 1

## INTRODUCTION

As air quality has become one of the major issues we are facing with, academic institutions and related industries have invested considerable amount of resources and research to monitor air pollution. Netherlands Organisation for Applied Scientific Research (TNO) has developed Spectrolite, a compact, low cost hyperspectral imager based on the technological heritage of TROPOspheric Monitoring Instrument (TROPOMI) for the monitoring of air quality and land use. In April 2016, the AROMAPEX campaign was organized in Berlin, Germany to measure the air quality over the city and compare different instruments to investigate the characteristics of them.

Following the document describes the development processes and related theories to retrieve tropospheric  $\text{NO}_2$  vertical column densities (VCDs) from Spectrolite spectral measurements on 21 April during the AROMAPEX campaign. The algorithm is obtained using the Spectrolite Level 1B data provided by TNO.

## AIR POLLUTION MONITORING

Air pollution is the introduction of harmful substances such as particulates, biological molecules into the Earth's atmosphere. It can be solid particles, liquid droplets, or gases from not only industrial activities but also natural origin and can have adverse effects on humans and the ecosystem.

Air pollutants can be categorized as primary or secondary pollutants. A primary pollutant is emitted directly from a source and produced from a process which can be natural or man-made, such as the sulfur dioxide from a volcanic eruption or carbon monoxide motor vehicle exhausts. By contrast, secondary pollutants are not emitted directly but form when other pollutants (primary pollutants) react in the atmosphere. Ground level ozone is a prominent example of a secondary pollutant. Some pollutants can be emitted directly and form from other primary pollutants, thus they are both primary and secondary pollutants.

Air pollution has a wide range of impact on both humans and environment. On one hand, the deposition and absorption of inhaled chemicals can directly cause health issues. Besides, air pollutants deposited in environmental media and absorbed by plants and animals can also result in chemicals' presence in food chain and thereby increase human exposure to air pollution. On the other hand, the structure and function of ecosystems will also be affected by the plants, animals and soil that contain air pollution, thus influencing our living standard. [1]

As air pollution has become one of the major non-negligible issues that the societies worldwide are facing with, it has aroused public awareness and serious concern. The significance of air quality is generally recognized by citizens, governments and organizations, since it affects every aspect of human life and future, including personal health, economic growth, environment as well as climate change. Air pollution monitoring is therefore also becoming a topic that institutions urge to research on. Air pollution monitoring is applied for the following purposes:

- To quantify pollution level. It provides detailed and scientific information about air quality and assessment of compliance with local air quality objective in order to make further policy.
- To detect and supervise pollution sources. It can help to find out the source and amount of pollution and verify the reported pollution produced by emissions inventories by comparing it with the monitored estimate.

Air pollution monitoring is a complicated but also important task. Our understanding of air pollution currently is not sufficient to precisely predict air quality at any locations at any times. Therefore, air pollution monitoring can help to improve our understanding and fill in the gap in the unknowns. During monitoring, the raw measurements of air pollutants can be processed to concentrations or vertical column densities. After analysis and interpretation, they can offer information about air quality and pollution levels. The change of air pollutants can also tell us how air pollutants interact with each other and the relationship between the pollutants and human activities or weather conditions.[2]



## CRITERIA POLLUTANTS AND NITROGEN DIOXIDE

United States Environment Protection Agency (EPA) introduced six common air pollutants called "criteria pollutants" to protect environment and ensure public health, the presence of these pollutants in ambient air is generally due to numerous diverse and widespread sources of emissions. They are carbon monoxide, lead, ground-level ozone, particulate matter, sulfur dioxide, and nitrogen dioxide. [3]

Nitric oxide and nitrogen dioxide are emitted by vehicles and power plants which are highly related to human activities. Emitted Nitric oxide is rapidly oxidized into nitrogen dioxide in the atmosphere. Exposure to nitrogen dioxide has been associated with various health effects, including respiratory symptoms, especially among asthmatic children. [4] Among all the criteria pollutants, nitrogen dioxide is particularly important not only because of its health effects but also because it contributes to impaired atmospheric visibility after absorbing visible solar radiation and has a potential direct role in global climate change if its concentrations were to become high enough. Besides, it is a key player in atmospheric chemistry and leads amongst others to the formation of tropospheric ozone, nitrate aerosols and acid deposition.[5]

The formation of ground-level  $O_3$  relies on the photolysis of  $NO_2$  (Equation 1.1), the dissociation comes from the excitation by sunlight.



Ground-level ozone appears after the subsequent association of the photoproduct ground electronic state oxygen atom ( $O(^3P)$ ) with  $O_2$  through a termolecular reaction (Equation 1.2) where M indicates any third co-reactant (i.e. nitrogen  $N_2$ ).



After the relaxation of  $O_3$ ,  $NO_2$  is obtained again and thus the cycle can continue repeating.



Even though on a global scale, emissions of nitrogen oxides from natural sources such as stratosphere, volcanic activities, and lightnings, far outweigh those generated by human activities, occupying about 62% of the total sources[6], the background atmospheric nitrogen oxides concentrations are very small since it is distributed all over the Earth surface. The major source of anthropogenic emissions of nitrogen dioxides into the atmosphere is the burning of fossil fuels: coal, oil and gas. In industrial areas, it usually comes from vehicle exhaust and electricity generation from coal-fired power stations. Therefore, the amount of nitrogen dioxides can offer quantified information about air quality and helps to detect pollution sources.

## CONCENTRATION, VOLUME MIXING RATIO AND COLUMN DENSITY

The measures of atmospheric composition can be expressed in different ways, including concentration, volume mixing ratio and column density.

The concentration of a gas is the amount of gas in a volume of air. (Equation 1.4) The amount could be mass, number of molecules or number of moles. Common units are  $\mu\text{g}/\text{m}^3$  and  $\text{molecules}/\text{m}^3$ .

$$\text{Concentration} = \frac{\text{Amount of gas}}{\text{Volume of air}} \quad (1.4)$$

The volume mixing ratio of a gas is defined as the volume of gas per unit volume of air. The unit of volume mixing ratio is normally parts per million by volume (ppmv). (Eq. 1.5) The mixing ratio of a gas has the virtue of remaining constant when the air density changes (which happens when the temperature or the pressure changes).

$$\text{VMR} = \frac{\text{Unit volume of gas}}{10^6 \text{ units volumes of (air + gas)}} \text{ppmv} \quad (1.5)$$

Column density can refer to slant column density( $N^S$ ) or vertical column density( $N^V$ ).  $N^S$  is the volume number concentration profile for a certain trace gas along the slant photon path (Eq. 1.6): [7]

$$N^S = \sum_0^{TOA} c(z)m(z)dz \quad (1.6)$$

, where  $z$  is the altitude ([m]),  $TOA$  is the top of atmosphere,  $c(z)$  is the concentration as function of height ( $[\text{molecules}/\text{m}^3]$ ) and  $m(z)$  is the height independent air mass factor.

Vertical column density( $N^V$ ) is the total amount of molecules in a vertical column of the atmosphere (1.7): [7]

$$N^V = \sum_0^{TOA} c(z)dz \quad (1.7)$$

, where  $z$  is the altitude ([m]),  $TOA$  is the top of atmosphere and  $c(z)$  is the concentration as function of height ( $[\text{molecules}/\text{m}^3]$ ). Vertical column density is independent to measurement techniques, viewing direction and wavelength, but only refers to atmosphere itself.

It should be noted that among all the measures mentioned above that can quantify atmospheric composition, concentration and vertical column density are most commonly used. However, in the case of tropospheric trace gases measurements, VCD instead of concentration close to the Earth surface is preferable to indicate the amount of nitrogen dioxides. Although concentration is more representative for surface pollution because it is the abundance of a constituent divided by the total volume of a mixture, VCD is more important for emission estimates and air quality model validation since it is vertically integrated concentration along the atmospheric light path, making it less affected by the dynamics of boundary layer that is often not well known. [8]

## COMMON METHODS USED FOR NO<sub>2</sub> VCD RETRIEVAL

The most commonly used methods to retrieve NO<sub>2</sub> vertical column density are space-borne observation and ground base measurement, both of which have their own advantages and drawbacks, making them preferable in different conditions.

### SPACE-BORNE OBSERVATION

In space-borne remote sensing, sensors are mounted on a satellite that orbits around the earth along a general ellipse. Space-borne remote sensing has the following advantages: [9]

- It can provide large area coverage;
- It can provide frequent and repetitive observations of area of interest;
- It can quantify ground features using radiometrically calibrated sensors; and
- It is an relatively lower cost method considering the area coverage and duration of operation despite that to develop a satellite and instrument on board costs huge amount of resources.

There have been quite a lot of space-borne remote sensing instruments providing imagery for research and operational applications for air pollution (trace gases) monitoring, such as GOME, SCIAMACHY and OMI.

The Global Ozone Monitoring Experiment (GOME) is a scanning spectrometer that covers the wavelength from 240 nm to 790 nm in UV/VIS region with spectral resolution of 0.2 nm to 0.4 nm. The measured spectra are mainly used to derive ozone total column and vertical profile, nitrogen dioxide, water vapour, sulphur oxide and other trace gases, as well as cloud properties and aerosols. [10] Both GOME/ERS-2 and GOME-2/MetOp use the same theory and provide atmospheric measurements of 25 years. However, for GOME/ERS-2, there are maximum 3 steps and the field of view of each step may be varied in size from 40 km x 40 km to 320 km x 40 km. The mode with the largest footprint (three steps with the field of view 320 km x 40 km) results in a total coverage of 960 km x 40 km and thus provides global coverage at the equator within 3 days. In the case of GOME-2/MetOp, the steps can be as many as 24 and the field of view of each step varies from 5 km x 40 km to 80 km x 40 km, thus the mode with the largest footprint (twenty four steps with the field of view 80 km x 40 km) leads to a total coverage of 1920 km x 40 km and thereby provides daily near global coverage at the equator.[10] SCanning Imaging Absorption spectroMeter for Atmospheric CHartographY (SCIAMACHY) is a passive remote sensing spectrometer that measures radiation from the atmosphere and Earth's surface in nadir and limb geometry, in the wavelength range between 240 and 2380 nm.[11] Global measurement of various trace gases in the troposphere and stratosphere are retrieved from the solar irradiance and Earth radiance spectra. The large wavelength makes it possible to determine aerosols and clouds more precisely.[12]

OMI, short for Ozone Monitoring Instrument, is on board Aura satellite of NASA's Earth Observing System to continue recording total ozone and other atmospheric parameters related to ozone chemistry and climate. The near real-time measurements

from OMI contain the main components to indicate air quality - Ozone, aerosol and other trace gases such as  $\text{NO}_2$ ,  $\text{SO}_2$  and  $\text{HCHO}$ . OMI completes global coverage in one day with a spatial resolution of  $13 \times 24 \text{ km}^2$  at nadir and a spectral resolution between 0.42 nm and 0.63 nm within spectral band from 264 nm to 504 nm. OMI combines the advantages of GOME and SCIAMACHY, it measures the complete spectrum in the ultraviolet/visible wavelength range, with complete spatial coverage.[13] Thanks to the improvements of OMI, Earth observation can be conducted in 740 wavelength bands along the satellite track with global coverage in 15 orbits on daily basis. The nominal  $13 \times 24 \text{ km}^2$  spatial resolution can be zoomed to  $13 \times 13 \text{ km}^2$  for detecting and tracking urban-scale pollution sources. Daily observations of the direct solar spectrum will also allow for accurate radiometric and wavelength calibration over the long term.[13]

However, there still exist some disadvantages due to the characteristics of satellite observation. The circulation movement of air pollution is relatively rapid but the temporal resolution of satellite observation is not high enough to offer real-time measurements. In addition, the movement of polar orbiting satellite makes it impossible to measure trace gases at any desired location and time. The altitude of satellite also determines that we can only measure the total column of trace gases and a chemistry transport model (CTM) such as TM5 or CHIMERE has to be applied to separate the total column in a stratospheric and tropospheric component, which reduces both time efficiency and accuracy.

## GROUND-BASE MEASUREMENT

The various types of instruments all have their pros and cons depending on the manpower available for their operation, the location and accessibility of the measurement site. Because ground station is normally stabilized at one fixed location during measurement, it has a satisfactory temporal resolution to offer real-time observations. But in order to obtain a larger coverage of area of interest, multiple stations are required due to its low spatial resolution.

The ground-base measurements can indicate either near-surface concentration or vertical column density. Near-surface  $\text{NO}_2$  concentrations are measured by chemiluminescence detectors. After routing an air sample to a reaction chamber, it can react with ozone,  $\text{NO}_2$  changes from stable status to excited state, result in emitting radiation which will be detected by a photomultiplier tube. [14] Vertical column density, on the other hand, can be obtained by Multi Axis Differential Optical Absorption Spectroscopy (MAX-DOAS) which utilizes scattered sunlight received from multiple viewing directions. Combining several viewing directions can help to derive the spatial distribution of various trace gases close to the instrument, especially in the lowest few kilometers of the atmosphere because MAX-DOAS is highly sensitive to absorbers.[15] One of the largest differences is that in-situ concentration monitoring can be performed any-time in the period of 24 hours in one day. But MAX-DOAS instrument can only conduct measurements during daylight hours when there is sunlight.

## AIRBORNE MEASUREMENT

Combining the advantages of both satellite and ground-base observation, airborne measurement is being used more and more popularly in the investigation, testing and vali-

dation of remote sensing measurements. The advantages of aircraft measurement are:

- It offers in-situ measurement of ground and atmospheric properties with quite high spatial resolution, sometimes regardless of the presence of high clouds;
- It can be conducted flexibly along a planned flight path at a targeted location and controllable time;
- It can also be used to explore atmospheric phenomena and process, study complex and fundamental Earth–atmosphere system properties. The obtained data helps to develop, parametrize and validate atmospheric models; and,
- It is an affordable way to test instruments for further space application.

However, there also exist disadvantages. It is not efficient to observe a large area using airborne remote sensing due to its low coverage area and high cost per unit area. Airborne remote sensing missions are often carried out much less frequently, mostly in campaigns as one-time operations, meanwhile satellites and ground stations offer the possibility of continuous monitoring and measurements. [9]

The AMAX-DOAS (Airborne Multi-AXis DOAS) instrument covers the spectral range from 300 to 600 nm.[16] Several airborne measurement campaigns have successfully taken place. During the CalNex campaign in California from 19th May to 19th July, 2010, the CU AMAX-DOAS was on aboard the NOAA Twin Otter research aircraft to measure horizontal and vertical distributions of NO<sub>2</sub>, HCHO and CHOCHO. By combining the measurements in nadir and zenith direction, and analysing the spectra in the UV and the visible spectral region, spatial distributions of trace gases can be mapped, providing a better chance to test and improve atmospheric models. Additionally, the result is compared with those obtained by other instruments aboard the aircraft and those integrated from ground based stations, satellites, to explore synergies and complement verification. [17]

In conclusion, with in-situ and passive remote sensing instruments on board, aircraft acquires huge flexibility to allow users to observe atmospheric phenomena, circulation and interaction. Occasional aircraft observations are compared with the total data volume produced by daily satellite or ground-based measurements, functioning as complementary measurements in either small or huge spatial scales with minimum disturbances by the atmosphere between sensor and object. At the same time, airborne instruments will also be improved and further developed. It might be much more convenient and operational if the techniques are successfully applied to drones.

## RESEARCH QUESTION

In summary, airborne measurements currently are regarded as a complementary method for satellite and ground-base observations due to its drawbacks. Spectrolite is newly developed and seen as an improved, compact and low cost hyperspectral imaging spectrometer. Through the test measurements during the AROMAPEX campaign, an algorithm is developed to retrieve NO<sub>2</sub> vertical column density in the troposphere. Therefore, the research question of this project is:

**Research Question:** Are the spectral measurements from Spectrolite instrument and the developed data processing algorithm sufficiently accurate to retrieve tropospheric NO<sub>2</sub> vertical column densities at high spatial resolution, in order to identify important emission sources on the ground?

In order to answer the main research question and present the report in an understandable way, the chapters are organized in the following order according to sub-research question.

This chapter (Chapter 1) introduces the background of this research, illustrating the significance and urgency to retrieve tropospheric NO<sub>2</sub> VCD and the common techniques to obtain it.

In the second chapter, Spectrolite instrument is introduced and an overview of the AROMAPEX campaign is given.

**Sub Question 1:** What is Spectrolite? When, where and what does it measure in this project to obtain NO<sub>2</sub> vertical column densities?

The Spectrolite instrument measures radiance, but it has to be linked to the amount of NO<sub>2</sub> in the troposphere (vertical column density). Thus, the concepts and methodology are demonstrated, including Differential Optical Absorption Spectroscopy (DOAS), radiative transfer model (RTM) and air mass factor (AMF). Besides, the particularity of tropospheric NO<sub>2</sub> VCD retrieval from airborne measurement, namely the reason why the processing algorithm used in this paper is different from those utilized in satellite and ground-base observations is also clarified. Chapter 3 answers Sub Question 2:

**Sub Question 2:** What is the general approach to retrieve NO<sub>2</sub> vertical column densities from spectral measurements? What is the particularity in airborne (Spectrolite) observations?

The atmosphere has a direct impact on what radiances the instrument measures (Sub Question 3). The fourth chapter studies the influence by looking into the generated Look-up Table (LUT) with radiative transfer model Double-Adding KNMI (DAK) and discusses the sensitivity of modeled outputs to different variables.

**Sub Question 3:** How are atmospheric components and surface properties on spectral measurements and the retrieved vertical column density?

Subsequently, step by step, the details of the processing algorithm from Spectrolite spectral measurements to tropospheric NO<sub>2</sub> VCD are illustrated in Chapter 5. (Sub Question 4) It contains airborne measurement wavelength calibration, DOAS fitting, AMF calculation and stratospheric correction.

**Sub Question 4:** Specifically in this project, how spectral measurements are processed to NO<sub>2</sub> vertical column densities?

Chapter 6 analyzes and visualizes the results obtained by the developed algorithm. Sub Question 5 asks to interpret the outcomes and identify the uncertainty.

**Sub Question 5:** What do the intermediate and final products indicate and how does the uncertainties in relevant geophysical parameters influence the results?

The chapter will summarize the answer to the main research question, evaluate the project and offer suggestions and outlooks for further study of the topic.

**Sub Question 6:** What conclusions could be made from the project? What improvements could help to obtain better results?





# 2

## SPECTROLITE INSTRUMENT AND AROMAPEX CAMPAIGN

**Sub Question 1:** What is Spectrolite? When, where and what does it measure in this project to obtain NO<sub>2</sub> vertical column densities?

### SPECTROLITE INSTRUMENT

Spectrolite (Figure 2.1) is a hyperspectral imaging spectrometer designed as a low cost modular system for multiple applications (air quality, land use or water quality), which gives Spectrolite following technical advantages[18]:

- Compactness makes it possible to install the instrument on a smaller aircraft or just as an add-on on a larger platform;
- Low-cost instruments require much less budget to be installed multiply on platforms, which can improve the coverage of observation. In addition, measurements can also be conducted more frequently, helping to increase temporal sampling (e.g. multiple overpasses per day to study diurnal processes); and
- A small, lightweight spectrometer can easily be mounted on a small aircraft or high-altitude UAV.

Spectrolite consists of an all-reflective, off-axis optical design, resulting in the benefits:

- The all-aluminum design makes it remain thermally stable during measurement;
- The choice of other wavelength ranges between 270nm and 2400nm does not affect the design so it can directly copied for usage;
- The adoption of an all-reflective, off-axis optical design gives more freedom to design the baffle for stray light; and

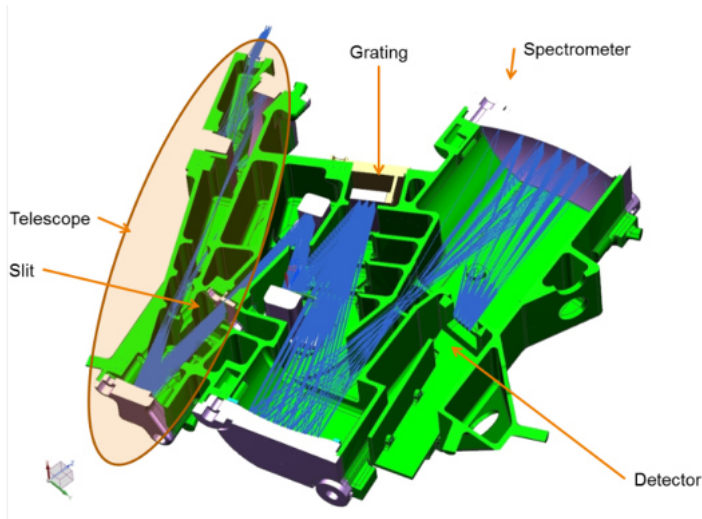


Figure 2.1: 3D drawing of Spectrolite showing the housing (green), components (grey) and optical path (blue).[18]

- Inherently low ghost stray light between detector and optical surfaces.

## LEVEL 0-1B DATA PROCESSING

Spectrolite measures the radiance received by the sensor, however, the raw measurements (Level 0) should be initially processed to Level 1B data in order to convert the raw detector images to spectral radiance that can be used in NO<sub>2</sub> column density retrieval. Level 0-1B data processor is presented in Figure 2.2.

The data processor is composed of several correction steps:

- Bad pixel removal.

All 'bad' or 'dead' pixels which are not - or only to a small extent - suitable for retrieval, are removed from the data. 'Bad' pixel is caused by a lattice constant mismatch between the substrate material and the light detecting material.[11] The removal is performed on the basis of a "Bad pixel map", which was determined based on ground dark and illuminated measurement. An interpolated data point to replace the removed pixel.

- Electronic offset and dark current removal

Electronic offset is the number of counts displayed when the detector puts out its lowest possible voltage and can be temperature dependent.[19] Dark current is the result of random thermal fluctuations producing enough energy to promote an electron across the band gap, creating an electron-hole pair that is separated by local electric fields. The free electron is stored in the well and spectrometer cannot distinguish these thermal electrons from those generated by incident photons, and they therefore appear as noise in the spectrum.[19] During this step the

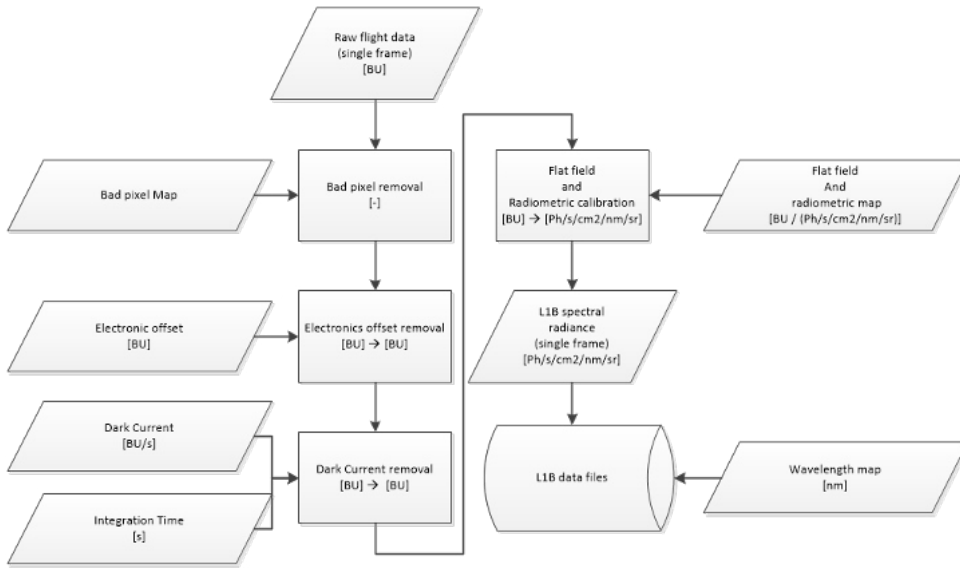


Figure 2.2: Spectrolite Berlin flight L0-1B data processor.[18]

electronics offset and dark current signal are subtracted on a pixel to pixel basis. The subtraction is performed on the basis of electronics offset and dark current key data that has been determined during an on ground dark measurement with several integration times.

- Flat fielding and Radiometric calibration

The data is transformed from [BU] to spectral radiance levels per pixel. For this correction a pixel based radiometric response map was generated and applied to the data. The radiometric response map has been generated on the basis of a measurement with an integrating sphere, which spectral radiance was made absolute through the calibration of the GOME 2 instrument.

- Wavelength Map

In this step, the data was augmented with a pixel based wavelength map which was based on measurements with a spectral line source.

## AROMAPEX CAMPAIGN

The AROMAPEX campaign was carried out from 11th to 21st of April, 2016 over the city of Berlin, Germany. The scientific teams involved in the campaign include researchers from Germany (FUB, University of Bremen, DLR, MPIC), Belgium (BIRA, VITO), Netherlands (KNMI, TNO, TU Delft) and Romania (INCAS, UGAL).[20] It was an excellent chance to test the Spectrolite instrument under atmospheric conditions and to compare NO<sub>2</sub> VCD results with those obtained with other instruments such as APEX [21], AirMAP [22] and SWING [23].[18]

The purpose of the AROMAPEX campaign was to measure the air quality over Berlin. Two aircrafts (DLR Do-228 and FUB Cessna-207) carried four instruments (APEX in the Do-228 and AirMAP, SWING, and Spectrolite in the Cessna). Meanwhile, three mobile DOAS systems and a set of static instruments (including two MAX-DOAS and a ceilometer) were operated on the ground across Berlin.[24] The data set obtained during the campaign allows to compare different instruments to investigate the characteristics of them, which is also the primary objective of the campaign. Additionally, unlike the AROMAT campaign in Bulgaria where these instruments were used separately, the measurements were all conducted simultaneously, thus making it possible to compare simultaneously to complement the results and conclusions retrieved from the previous campaign.

From 11th till 20th April during the campaign, clouds were often present but cloud forecast was constantly updated in order to decide the research flights on daily basis. On 21st April (the golden day), the day had the most optimal weather conditions and the clear sky allowed to conduct two sets of flights (in the morning and afternoon) which were synchronized with the ground-based measurements. Spectrolite Level 1b data set used in this paper is provided by TNO which has conducted the initial processing procedures (Level 0-1B), including bad pixel removal, electronic offset and dark current removal, flat fielding and radiometric calibration and wavelength map augmentation.[18]

This project makes use of the Spectrolite data to obtain tropospheric NO<sub>2</sub> vertical column densities. The preliminary results show a good comparison with those obtained by other instruments (AirMAP and SWING) from other research groups at the same time during AROMAPEX campaign and thus give much confidence for the further development of Spectrolite.

# 3

## METHODOLOGY

**Sub Question 2:** What is the general approach to retrieve NO<sub>2</sub> vertical column densities from spectral measurements? What is the particularity in airborne (Spectrolite) observations?

Airborne UV/visible spectrometers have been used in the past for studies of stratospheric and tropospheric composition.[25] The most common method to derive NO<sub>2</sub> vertical column densities (VCDs) from airborne (and space-borne) measurements is composed of two steps. The first step is to derive slant column densities from spectral measurements by Differential Optical Absorption Spectroscopy (DOAS) [26]. Afterwards, air mass factors (AMFs) are applied to slant column densities (SCDs) to obtain VCDs.

## DOAS FITTING AND DIFFERENTIAL SLANT COLUMN DENSITY

Before the radiance is measured by a sensor on aircraft, it has experienced extinction due to the absorption by trace gases and aerosols, and scattering by air molecules, clouds, aerosols and surface. The amount of energy that extincts from the original beam by absorption and scattering can be characterized as cross section. Because the scattering and reflectance from air molecules, aerosol, clouds and surface have a smooth impact on the spectrum, absorption cross section is often used to include both the portion due to scattering and true absorption. According to Lambert-Beer law, absorption cross section is calculated by Equation 3.1:

$$I = I_0 e^{-\sigma n s} \quad (3.1)$$

Where  $I_0$  and  $I$  are the incident and transmitted light radiance spectrum,  $\sigma$  is the absorption cross section ( $\text{cm}^2 \text{molecule}^{-1}$ ),  $n$  is the number concentration of absorbing gas ( $\text{molecule}/\text{cm}^2$ ), and  $s$  is the pathlength in cm.[27]

It can also be written in a differential form:

$$dI = dI_0 e^{-\sigma n ds} \quad (3.2)$$

As a result of electronic, vibrational and rotational transitions of molecular energy levels, trace gases have characteristic absorption features as function of wavelength, which is demonstrated in Figure 3.1.[28]

Since optical thickness  $\tau$  is defined as the natural logarithm of the ratio of incident to transmitted spectral radiant power through a material,  $\tau = \ln(I_0/I)$ . [30] Therefore, the relationship between source and radiance spectrum can be written as Equation 3.3.

$$I(\lambda) = I_0 \cdot e^{-\tau(\lambda)} \quad (3.3)$$

Where  $\tau(\lambda)$  is the slant optical thickness of the trace gas,  $I$  is the measured spectrum which contains the absorption of the trace gas of interest,  $I_0$  is the reference spectrum without the trace gas of interest.[11] Although this law strictly speaking applies only to direct sun observations where every photon has the same light path through the atmosphere, it can also be applied to observations of scattered sunlight when the trace gas of interest is the regime called 'optically thin' (optical depth  $< 1$ ). [31]

Slant optical thickness spectrum  $\tau(\lambda)$  is influenced by the same parameters that affect the radiance spectra: the absorption of trace gases and aerosols, and scattering of air molecules, clouds, aerosols and surface. In order to eliminate the influence, differential slant optical thickness spectrum  $\tau^*(\lambda)$  is obtained by subtracting a low-order polynomial fit  $P(\lambda)$  which serves as a high-pass filter to slant optical thickness spectrum (Equation 3.4). The purpose is to account for scattering and absorption that vary gradually with the wavelength. Moreover, the high-pass filter takes out gradually varying radiometric calibration errors and other instrumental multiplicative effects.  $\tau^*(\lambda)$ , however, is only impacted by trace gases with absorption cross sections that show rapid variation with wavelength:

$$\tau^*(\lambda) = \tau(\lambda) - P(\lambda) \quad (3.4)$$

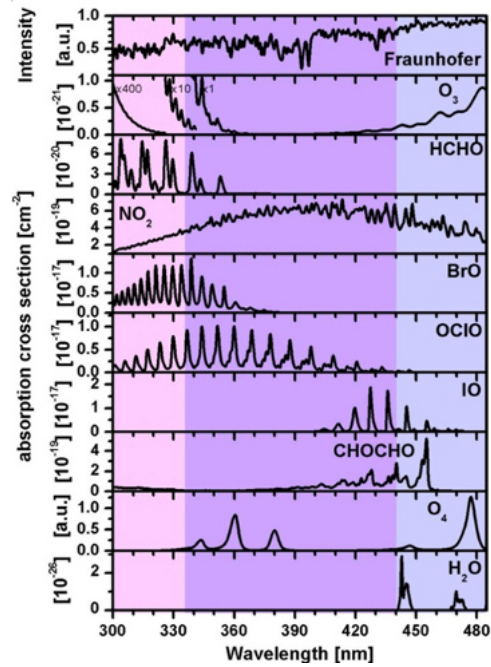


Figure 3.1: Absorption Cross Section Dependence of Several Trace Gases on Wavelength in the UV and Visible.[29]

Differential slant optical thickness is the sum of differential absorption cross sections  $\sigma^*(\lambda)$ , multiplied with the slant column densities of the trace gases  $N^S$  which is defined as the amount of the trace gas along an average path that photons take within a fit window as they travel from the sun, through the atmosphere to the sensor. DOAS method is widely used to measure trace gases in the atmosphere and utilizes the fact that trace gases often have unique spectral fingerprints. Regularly, DOAS method is basically to fit the differential absorption cross-sections to the measured sun-normalized Earth radiance spectrum, to obtain the slant column density (Equation 3.5). [26]

$$\tau^* = \sigma_{NO_2}^*(\lambda) \cdot N_{NO_2}^S + \sigma_{O_3}^*(\lambda) \cdot N_{O_3}^S + \sigma_{HCHO}^*(\lambda) \cdot N_{HCHO}^S + \dots \quad (3.5)$$

It is called DOAS equation which can also be written a Equation 3.6

$$\ln\left(\frac{I_0(\lambda)}{I(\lambda)}\right) = P(\lambda) + \sigma_{NO_2}^*(\lambda) \cdot N_{NO_2}^S + \sigma_{O_3}^*(\lambda) \cdot N_{O_3}^S + \sigma_{HCHO}^*(\lambda) \cdot N_{HCHO}^S + \dots \quad (3.6)$$

Among the parameters in Equation 3.5,  $\tau(\lambda)$  is derived from radiance measurements and  $\sigma^*(\lambda)$  are retrieved from known database with experimental measurement conducted in a lab.  $N^S$  is the SCDs for different trace gases. Therefore,  $NO_2$  slant column density  $N_{NO_2}^S$  is obtained from DOAS method, and it is the intermediate product before VCD.

DOAS analysis requires two radiance measurements, radiance scattered by air molecules and aerosols below the aircraft and the surface, and reference spectra which does not contain the absorption of the trace gas of interest in order to obtain absolute vertical column density. In the modeled environment, differential slant column density can be calculated by one radiance simulation with a trace gas in the atmosphere ( $I$ ) and a second simulation without that trace gas in the atmosphere ( $I_0$ ), then the SCD ( $N^S$ ) can be derived from Equation 3.7

$$N^S = \frac{1}{\sigma} \log\left(\frac{I_0}{I}\right) \quad (3.7)$$

In satellite measurement (e.g. OMI), solar irradiance is directly measured as a reference by looking towards the sun in Vacuum space, so the derived slant column density will be absolute SCD in the atmosphere. On the contrary, in the case of airborne (Spectrolite) observations, there always exist trace gases (atmosphere) between the aircraft and the top of atmosphere. In the real atmosphere, we cannot 'remove' the trace gas but we can choose the areas which almost only contain a background abundance of  $NO_2$  (pollution free) or a relatively low amount of pollution (remote from urban area) so that the retrieved DSCDs are mostly positive. However, we do not know the absolute pollution levels, which is the disadvantage of utilizing reference. However, afterwards, we can assume that satellite (OMI) observations offer a good estimate of the reference level. It can help to convert the relative scale to an absolute scale by adding the SCD of reference to dSCD. The detail of calculation process will be explained in Chapter 4. As a consequence, we need to find out an alternative reference spectra in order to obtain slant column density. We use a radiance spectrum that is measured during the flight as



reference and the result obtained with DOAS is differential slant column density (dSCD) relative to this reference.

The total SCD can be split into a tropospheric and a stratospheric part:

$$SCD = SCD_{trop} + SCD_{strat} \quad (3.8)$$

In the lower atmosphere, the higher air density brings more Rayleigh scattering and higher particle loadings cause in more Mie scattering. As a result, we can assume that the last scattering event, before the light reaches the sensor, takes place in the lower troposphere. [32] Therefore, the light detected by the instrument traverses the same path in the stratosphere, regardless of the telescope elevation angle  $\alpha$ :

$$SCD_{\alpha, strat} = SCD_{90, strat} \quad (3.9)$$

Since not only the measured spectra, but also the reference spectra contains atmospheric trace gas absorption, DSCD represents the difference in absorption between the atmospheric measurement and the reference: .

$$\begin{aligned} dSCD &= SCD_{\alpha} - SCD_{ref} = (SCD_{\alpha, trop} + SCD_{\alpha, strat}) - (SCD_{ref, trop} + SCD_{ref, strat}) \\ &= SCD_{\alpha, trop} - SCD_{ref, trop} + \Delta SCD_{strat} \end{aligned} \quad (3.10)$$

, where  $\Delta SCD_{strat}$  is the second order effect, stratospheric slant column density change over time as function of solar zenith angle  $\Delta SZ A_{\alpha, ref}$ . From Equation 3.10, we can know that an additional advantage of this approach to select a reference spectrum is that the need for a stratospheric NO<sub>2</sub> correction is strongly reduced, especially when observations are done in a period with relatively little variability in the solar zenith angle, hence a quite constant average photon path length through the stratosphere. Although in principle, any spectrum can be selected as reference, it is common practice to select a spectrum measured over a region with relatively low pollution levels, such that high pollution levels at other locations correspond to positive dSCDs.

## AIR MASS FACTOR

After the first step, differential slant column densities (dSCDs) are derived. (Differential) Slant column density is a measured quantity. In order to account for enhancement in the length of light path due to viewing geometry, surface albedo or aerosol scattering air mass factors are utilized to derive vertical column density. To conclude, AMF and VCD depends not only on the state of the atmosphere (e.g. the amount of trace gas, the impact from clouds or aerosols), but also on the observation geometric conditions (e.g. solar zenith angle, viewing direction wavelength), as well as on the surface properties like surface reflectance. Table 3.1 show the influence that each parameter has on reflectance spectrum, air mass factor and slant column density.

We can see that all elements have a large influence on slant column density. The same applies to air mass factor except that for optically thin trace gases like NO<sub>2</sub>, the impact of VCD on AMF is low while for optically thin trace gases in UV, mainly Ozone, the impact is high. In the case of reflectance spectrum, aerosol vertical distribution has

Parameters	Reflectance Spectrum	AMF	SCD
Wavelength <sup>(1)</sup>	H	H	H
Solar Zenith Angle <sup>(1)</sup>	H	H	H
Viewing Zenith Angle <sup>(1)</sup>	H	H	H
Relative Azimuth Angle <sup>(1)</sup>	H	H	H
Rayleigh Scattering <sup>(1)</sup>	H	H	H
Surface Albedo <sup>(2)</sup>	H	H	H
Aerosol Optical Thickness <sup>(2)</sup>	H	H	H
Aerosol Vertical Profile <sup>(2)</sup>	L	H	H
Trace Gas VCD <sup>(2)</sup>	L <sup>(3)</sup> /H <sup>(4)</sup>	L <sup>(3)</sup> /H <sup>(4)</sup>	H
Trace Gas Vertical Profile <sup>(2)</sup>	L <sup>(3)</sup> /H <sup>(4)</sup>	H	H

Table 3.1: The dependence of air mass factor and slant column density on different parameters, H means high impact while L indicates low impact. (1) known with high accuracy (independent of measurement); (2) known with quite low accuracy (poorly constrained a-priori information); (3) for optically thin trace gases like NO<sub>2</sub>, HCHO (no impact on 'average light path'); (4) for optically thick trace gases, mainly O<sub>3</sub> in UV (affects 'average light path')

a low influence, so do the VCD and vertical profile of optically thin trace gases like NO<sub>2</sub>. However, the VCD and vertical profile of Ozone in UV acquire small effect. In addition, among all parameters, vertical column density applies only to one species and does not depend on other aspects. It indicates the amount of trace gas there is in the atmosphere. Among all parameters in Figure 3.1, trace gas vertical column density is what we want to know, AMF is derived from radiative transfer model, slant column density is obtained from spectral measurement after DOAS fitting. In the case of NO<sub>2</sub>, VCD is highly affected by SCD but not AMF.

Air mass factor (AMF) is the ratio between slant column and vertical column as shown in Equation 3.11, and depends on the radiative transfer properties of the atmosphere. It is calculated with a radiative transfer model. [33]

$$N^V = \frac{N^S}{AMF} \quad (3.11)$$

### RADIATIVE TRANSFER MODEL

Radiative transfer is the physical phenomenon of energy transfer in the form of electromagnetic radiation. The propagation of radiation through a medium is affected by absorption, emission, and scattering processes.[34] Radiative transfer models are of great significance in atmospheric remote sensing: they can for instance be used i) for sensitivity studies: with forward modeling we know how the measurements are affected by atmospheric properties and ii) for retrievals that rely on the comparison of real and simulated measurements. The retrieval of quantitative information on surface properties is disturbed by the scattering and absorption processes. Radiative transfer models and their inversions are widely used to correct for such effects on the propagation of light. The foundation of radiative transfer models is the radiative transfer equation which is a monochromatic equation to calculate radiance in a single layer of the Earth's atmo-

sphere (Equation 3.12) and implies that the radiation is related to the losses and gains because of extinction and emission respectively during its propagation in a medium. [35]

$$\frac{dI_\sigma}{ds} = -(\epsilon_a(\lambda) + \epsilon_s(\lambda)) \cdot (I_\lambda) + \epsilon_s(\lambda) \cdot \int_0^\pi \int_0^{2\pi} I(\lambda, \theta, \phi) \cdot \frac{S(\theta, \phi)}{4\pi} d\phi \cdot \sin\theta d\theta \quad (3.12)$$

,where  $\lambda$  is the wavelength,  $dI(\lambda)/ds$  represents the change in the spectrum of incoming radiation that move through an infinitesimally thin layer with thickness  $ds$ ,  $\epsilon_a$  and  $\epsilon_s$  respectively donate the absorption and scattering coefficient and  $S(\theta, \phi)$  donates the dimensionless scattering function.

Examples common radiative transfer models are 6S (Second Simulation of a Satellite Signal in the Solar Spectrum) [36] and SCIATRAN [37]. These RTMs are frequently run in a forward mode, generating look-up tables (LUTs), which will be used afterwards during the inversion process for atmospheric compensation or trace gas retrieval.

6S enables accurate simulations of satellite and plane observations in the MODIS (MODerate resolution Imaging Spectroradiometer) atmospheric correction algorithm. [38] It permits calculations of near-nadir (down-looking) aircraft observations, accounting for elevated targets, modeling of a realistic molecular/aerosol/ mixed atmosphere, use of (non-)Lambertian surface conditions. [36]

SCIATRAN offers fast and accurate radiance spectra simulations for atmospheric remote sensing observations in the UV-visible-TIR spectral range. A coupled ocean-atmosphere system can be used to simulate the radiance over and under the water surface. [37] SCIATRAN can be utilized in a broad range of applications: retrieval of atmospheric constituents from measurements of direct or scattered solar light, calculation of air mass factors and trace gases slant columns, and the retrieval of aerosol and cloud parameters.

In this project, radiative transfer model Double-Adding KNMI (DAK) is performed to derive the surface and atmospheric contribution to radiance for a specified geometry. DAK makes use of the doubling adding method, a two-step process. Calculations start with a very thin atmospheric layer in which only single-scattering occurs. An identical layer is then introduced, the optical properties of the combined layer are calculated and internal scattering is included. This step is the 'doubling' one. The doubling step will be repeated until the layer has reached the required optical depth. Multiple scattering is thus taken into account. The 'adding' step is a similar mechanism designed to handle layers with different optical properties. These layers are combined in a single one which will be added to a third layer and so on. The 'adding' is assumed completed when the boundary fluxes of the modeled layers converge. In this study, each input parameter was set to achieve a four or five decimal accuracy.

The results are stored in look-up tables (LUTs), these tables contain all calculated variables with corresponding simulated radiance. They can be considered as multi-dimensional matrix stored in a text file.

### CALCULATION OF AIR MASS FACTOR FROM DAK LOOK-UP TABLE

The radiance obtained by a sensor at a specified geometric condition with a predefined surface property for a defined atmospheric scenario is the primary output from radiative transfer modeling. However, during airborne remote sensing measurements, we are

more interested in their sensitivity to atmospheric trace gases. Usually the sensitivity is expressed as so called Air Mass Factor. Besides the observation geometry and the atmospheric properties, the AMF depends in particular on the spatial distribution of the trace gas of interest.

Box air mass factors (Box-AMFs) characterize the ratio of the partial SCD to the partial VCD of an atmospheric layer with an assumed constant trace gas concentration. The DAK modeling in this project includes two NO<sub>2</sub> conditions: a reference scenario with only background trace gases profile, and a scenario with a NO<sub>2</sub> perturbation of  $10^{16} \text{ mole/cm}_3$  in a 100 meters layer is added to specific layers in the atmospheric profile. By comparing the radiance outputs from these two conditions, Box-AMF can be derived as following.

Firstly, partial NO<sub>2</sub> absorption optical thickness caused by the perturbation is calculated by subtracting total molecule absorption optical thickness in reference scenario from the one with NO<sub>2</sub> perturbation as in Equation 3.13.

$$\tau_{NO_2} = \tau_{tot} - \tau_{0tot} \quad (3.13)$$

Then, Equation 3.14 shows that Box-AMF (BAMF) can be obtained by dividing partial slant optical thickness  $\ln(\frac{I_0}{I})$  by partial NO<sub>2</sub> absorption optical thickness  $\tau_{NO_2}$ . A vertical profile of Box-AMF calculated by the SCIATRAN RTM for a rural ground pixel as function of perturbation height should be similar to Figure 3.2. [39]

$$\text{Box-AMF} = \ln(\frac{I_0}{I}) / \tau_{NO_2} \quad (3.14)$$

In order to compute the influence of atmospheric scattering, the atmosphere is divided as several vertically resolved layers. For optically thin species such as NO<sub>2</sub>, AMF can be obtained as the linear sum of the Box-AMF of each layer over the whole atmosphere weighted by the respective partial trace gas vertical column density, as presented in Equation 3.15.[31] It means that as long as we have LUT to derive Box-AMFs ( $AMF_i$ ) and the respective trace gas profile, AMFs can be calculated, which is a big advantage of calculating Box-AMF: even though height profiles are different, AMF can still be quickly retrieved if we have LUT beforehand. It is reasonable to build up a universal data base for different trace gases in order to calculate AMFs for arbitrary species.

$$AMF = \frac{\sum_0^{TOA} AMF_i \cdot VCD_i}{\sum_0^{TOA} VCD_i} \quad (3.15)$$

Here  $AMF_i$  and  $VCD_i$  refer to the Box-AMF and the partial vertical column density for layer  $i$ ; within the layer the trace gas concentration is assumed to be constant. The sum is carried out over all layers  $i$  (from the surface to the top of the atmosphere, TOA).

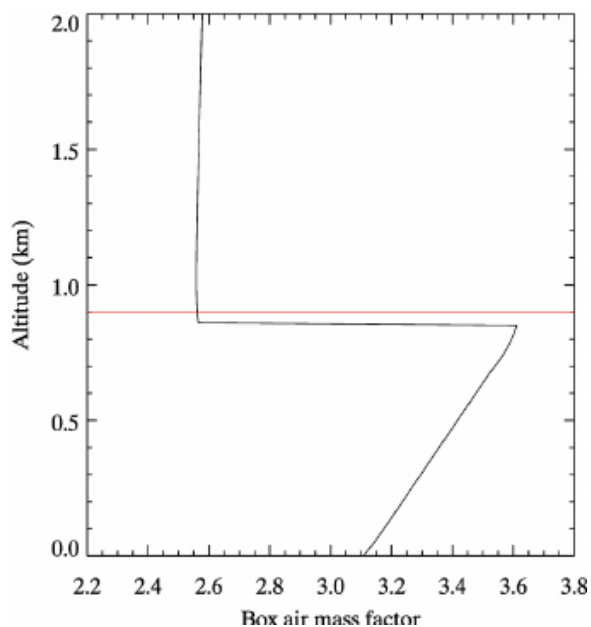


Figure 3.2: A typical box air mass factor calculated by the SCIATRAN RTM for a rural ground pixel. The red line indicates the instrument altitude (0.9 km) at the time of the measurement. [39] Box-AMF starts from approximately 3.1 near the Earth surface, increases steadily (almost linearly) to around 3.6 just below the sensor's altitude, then drops dramatically as it reaches instrument height. Finally it stabilizes at 2.6 afterwards above the instrument.



# 4

## GENERATION OF DAK LUT AND SENSITIVITY STUDY

**Sub Question 3:** How are atmospheric components and surface properties on spectral measurements and the retrieved vertical column density?

For the conversion from slant column density to vertical column density, it is critical to obtain accurate radiative transfer calculations for air mass factor in the solar spectral range. The Doubling-Adding KNMI (DAK) model is an accurate and efficient line-by-line, multiple scattering, radiative transfer model of the Earth's atmosphere in plane-parallel geometry.[40] The model atmosphere may contain gas absorptions, and aerosol and cloud particle absorption and scattering. Since the 1990's DAK has been used for many satellite retrieval applications, e.g. cloud and aerosol remote sensing and ozone column retrievals.

The Doubling-Adding KNMI (DAK) program computes the internal radiation field and emerging radiation field at top and bottom of a planetary atmosphere in the short-wave region of the spectrum. Specific data files are aimed at calculations for the Earth's atmosphere. The algorithm of the program is based on the doubling-adding method. The program solves the monochromatic radiative transfer problem for solar radiation in the Earth's atmosphere.

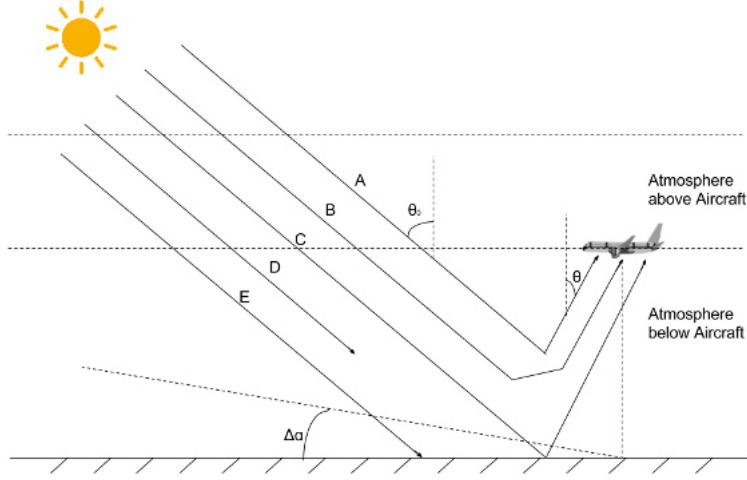


Figure 4.1: The light paths of photons from the Sun to the sensor on the aircraft. **A** is single scattering path. **B** represents light path with multiple scatterings. **C** indicates the scattering at surface. **D** and **E** are the absorptions by aerosol/trace gases and surface.

## INPUT PARAMETERS

Before running the DAK program, it is crucial to predefine the input settings of certain parameters and files because the inputs for simulation will influence the generation of Look-up Table (LUT), thus also on the precision of further outputs which are air mass factor and vertical column density. In addition, it should also be underlined that the monochromatic incident solar ux is assumed to be  $\pi$ , perpendicular to the solar beam, at all wavelengths. The calculated radiances in the LUT are therefore automatically normalized to the incident solar flux. The step intervals of input parameters cannot be too dense because the file size of the Look-up Table should also be taken into consideration. A Look-up Table with large file size not only occupies space on hard disk, but also increases the reading and processing time when being used in further steps, which is quite frequently.

Each radiance measurement by Spectrolite comprises an infinite number of possible photons paths. However, these can roughly be divided into five categories. Figure 4.1 shows schematic paths of photons that are emitted by the Sun and received by the sensors on aircraft. **A** is single scattering path where incoming irradiance is only scattered once by air molecules, aerosols or clouds. **B** represents light path with multiple scatterings. **C** indicates the scattering at surface. **D** and **E**, on the other hand, are the absorptions by aerosol/trace gases and surface, respectively. Moreover,  $\theta_0$  and  $\theta$  are solar zenith angle and viewing zenith angle, while  $\Delta\alpha$  is relative azimuth angle between the Sun and the aircraft. The relative importance of each of these five categories varies depending on solar zenith angle, viewing zenith angle, aerosol optical thickness, wavelength, surface reflectance, etc. and influences the sensitivity to  $\text{NO}_2$  at different altitudes (Box-AMF).

Therefore, the range of input parameters should be limited according to environ-



Parameters	Sources
Wavelength	Defined by User
Aircraft Altitude	Spectrolite Measurements
Surface Temperature	Weather Record
Surface Pressure	Weather Record
Surface Reflectance	Retrieved with Landsat Surface Reflectance Product
Aerosol Optical Thickness	Aeronet Measurements
Single Scattering Albedo	Aeronet Measurements
Aerosol Layer Height	Defined by User
Solar Zenith Angle	Python Astral Package
Viewing Zenith Angle	Spectrolite Measurements
Relative Azimuth Angle	Spectrolite Measurements

Table 4.1: Parameters that need to be defined in the DAK input files and their sources.

mental conditions and the time of measurement. Also for the sampling of each parameter within this range, a reasonable balance must be found between accuracy and practical use. As is shown in Figure 4.1, the parameters that need to be predefined in the DAK input files can be concluded in Table 4.1. The sources of these parameters, namely the datasets obtained by other measurements are also looked into in order to narrow down the ranges.

## PARAMETERS SETTINGS

For various parameters mentioned in Table 4.1, there are datasets available (second column in the table) to acquire the conditions during the Spectrolite measurement in order to narrow down the range of input parameters.

### WAVELENGTH

Wavelength has an impact on the scattering of aerosols, clouds, air molecules and absorption of aerosols and trace gases.

As is shown in Figure 4.2, when light travels through the atmosphere, type of scattering that depends on the wavelength of spectra and the radius of particle. For aerosols and clouds, their diameters are similar to the wavelength of sunlight, so Mie scattering will occur. The same will happen to dust, pollen, smoke and microscopic water droplets. Mie scattering occurs mostly in the lower parts of the atmosphere where larger particles are more abundant, and dominates in cloudy conditions. On the other hand, since the diameters of air molecules are much smaller than the wavelength of the irradiation, Rayleigh scattering will occur. However, if the radius of air molecules is too small ( $\frac{d}{R} < 0.002$ ), the scattering can be neglected. That is the reason why the UV/Visible part of sunlight is commonly used in atmospheric remote sensing. In conclusion, regarding UV/Visible, scattering will occur on the Earth surface, in aerosols and clouds with Mie scattering and in air molecules with Rayleigh Scattering.

Figure 4.3 demonstrates the profile of NO<sub>2</sub> absorption cross section as function of

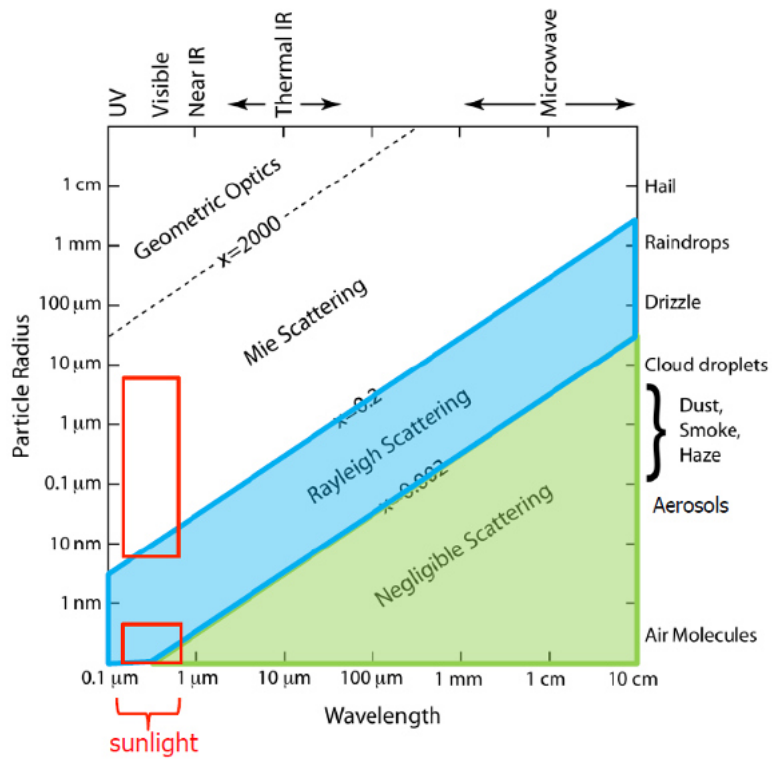


Figure 4.2: Type of scattering as function of the radius of particle and the wavelength of spectra.

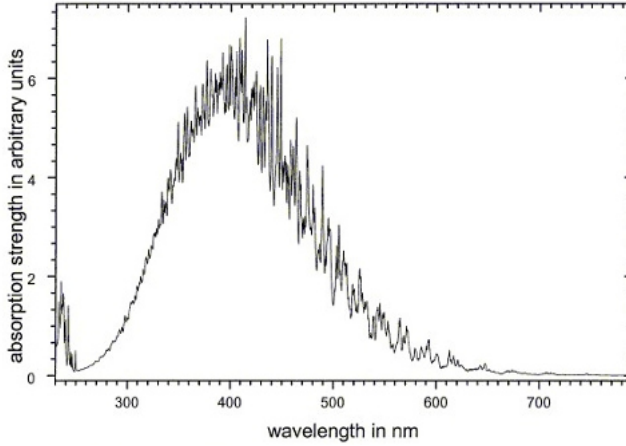


Figure 4.3: Relative NO<sub>2</sub> Spectrum at 293K measured by GOME FM between 231-794 nm. The spectral resolution is 0.2 nm at wavelength below 0.3 nm and above 400 nm.[41]

wavelength. Absorption cross section is proportional to the ability of a molecule to absorb a photon of a particular wavelength and polarization. It quantifies the probability of a certain photon-particle interaction. In the wavelength band between 400 nm to 500 nm, NO<sub>2</sub> absorption cross section acquires the highest variability, which means that the spectrum is most sensitive to NO<sub>2</sub>. When the spectrum within this wavelength range are used, photon-particle interaction is more remarkable. Therefore in this project, 440 nm is chosen as the wavelength of simulation.

## ALTITUDE

It is well known that the movements of aircraft during a flight can be simplified as takeoff, stable flight, turning and landing. In the simulation of DAK model, instrument altitude is considered as the same as aircraft altitude because compared to tropospheric trace gas profile height, the distance between centers of GPS and Spectrolite instruments are much smaller and consequently can be neglected. In addition, the changes of aircraft altitude during stable flight are also negligible so the altitude is considered constant.

According to the geolocation file retrieved during the campaign, the aircraft altitude is visualized in Figure 4.4. It can be concluded there are two flights on 21 April, in the morning and afternoon, which are indicated in blue and red lines respectively. In the morning, from 9 am to 9:30 am, the aircraft was taking off and climbing. After slightly more than 2 hours stable flight, the aircraft started descending and finally landed at 12:20 pm. While in the afternoon, it took off at 1:45 pm and started flying steadily at 2:15 pm. At 4:15 pm the aircraft started to land and reached the ground after 45 minutes. The average altitude during the stable height is approximately 3.1 km. Thus in the DAK model input files, output altitude, namely the altitude where radiance is simulated would be 3.1 km. Within this project, DAK simulations are not done for other flight altitudes.

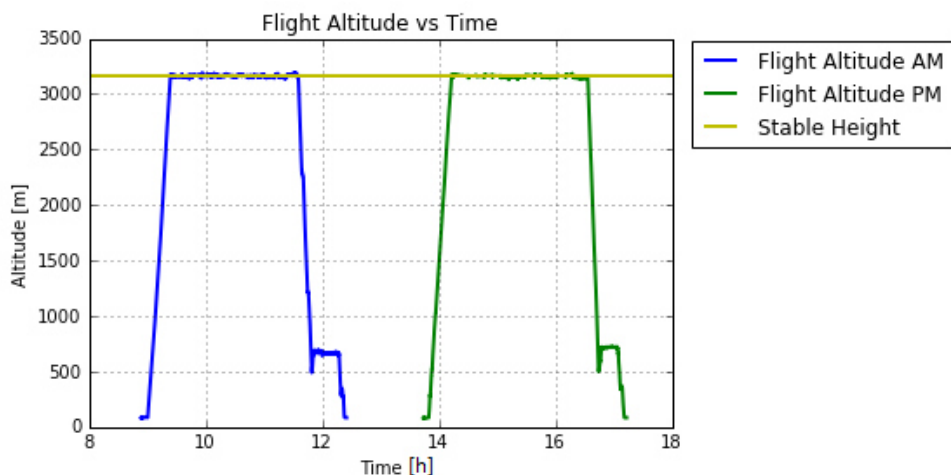


Figure 4.4: Flight Altitude during Spectrolite Measurements. The blue, green lines indicate the aircraft altitude as function of time in the morning and afternoon respectively. And the red line is the averaged altitude during stable flight.

### ATMOSPHERIC PROFILE

Atmospheric profile contains pressure, temperature, as well as trace gas mixing ratio profile. The profile used as simulation input depends on the surface pressure, temperature and the choice of reference atmosphere.

#### BACKGROUND PROFILE DATA

Within the DAK package, there are six reference atmospheres, each with associated pressure, temperature and volume mixing ratio profiles for trace gases. They are:

- Tropical: files 'tro\_afgl.dat1', 'tro\_afgl.dat2', 'tro.dat'.
- Mid-latitude summer: files 'mls\_afgl.dat1', 'mls\_afgl.dat2', 'mls.dat'.
- Mid-latitude winter: files 'mlw\_afgl.dat1', 'mlw.dat', 'mlw\_afgl.dat2'.
- Subarctic summer: 'sas\_afgl.dat1', 'sas\_afgl.dat2', 'sas.dat'.
- Subarctic winter: 'saw\_afgl.dat1', 'saw.dat', 'saw\_afgl.dat2'.
- US standard: 'u76\_afgl.dat1', 'u76\_afgl.dat2'.

The files with \_afgl.dat1 contain all AFGL levels up to 100 km. Meanwhile, the ones with \_afgl.dat2 contain the Lowtran7 levels up to 100 km. These are the mostly used ones.

The measurements were conducted in Berlin on 21 April. Even though April is not as warm as August, but it can be generalized as mid-latitude region during summer, so mls\_afgl.dat2 is used for modeling.

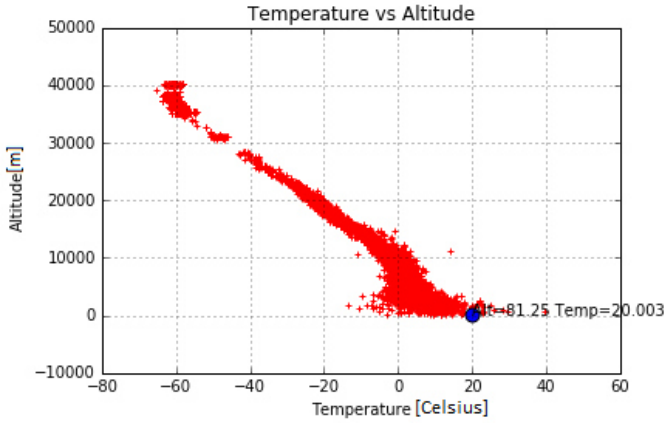


Figure 4.5: ADSB Temperature Vertical Profile Measurement during the same day

In addition,  $\text{NO}_2$  absorption spectrum is given in `NO2T_VD.dat` where 'VD' is short for Vandaele who has researched in measuring the  $\text{NO}_2$  absorption cross-section from 42 000 to 100 000  $\text{cm}^{-1}$  (238 - 1000 nm) with a Fourier transform spectrometer and a 5 m temperature controlled multiple reflection cell.[42] The cross sections have been convoluted with a Gaussian slit function with a FWHM of 0.05nm for the wavelength range 255nm - 665nm with a step of 0.02 nm, in order to create a fairly high-resolution spectrum that is relatively smooth. The same cross-section file `NO2T_VD.dat` is also used for the DOAS fitting later, although a different slit function width is applied.

#### SURFACE TEMPERATURE AND PRESSURE

Surface temperature and pressure influence the input atmospheric profile and thus the output by applying scaling factor to the temperature and pressure profile in the given atmospheric data file. The scaling factor is the division of new surface temperature or pressure and the original one.

During the AROMAPEX campaign, ADSB (Automatic Dependent Surveillance Broadcast) measurement was being taken at the same time to retrieve wind and temperature observations in the upper air, including the pressure and temperature vertical profile as function of altitude.

The profiles of temperature and pressure are visualized in Figure 4.5 and 4.6 respectively to check get real-time information about the temperature and pressure on the surface. Nevertheless, the lowest point ADSB ever managed to successfully measure is at 81.25 meters high, which is not low enough to be considered as earth surface. In addition, after investigating the effect of surface temperature and pressure, it is much smaller because the scaling factor is always slightly shifted from 1. Thus 291 K and 300K are chosen to represent the two temperature conditions, meanwhile surface pressure is set up to be fixed at 1015 hPa.

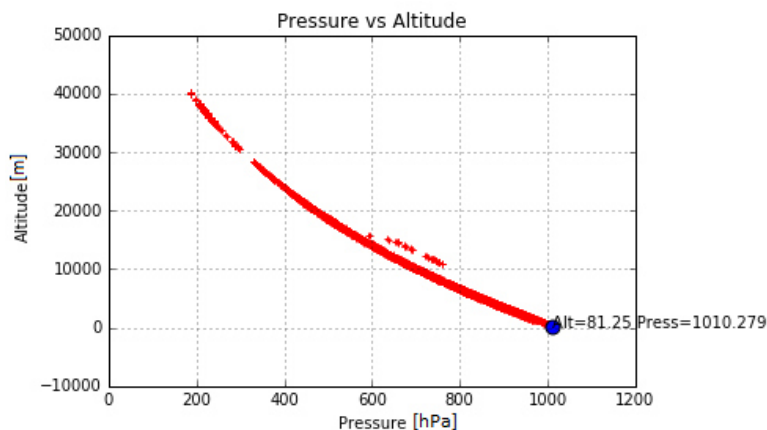


Figure 4.6: ADSB Pressure Vertical Profile Measurement during the same day

### AEROSOL PROFILE

Aerosol profile describes the aerosol parameters used in DAK for each layer. Layers are defined by the altitude layers in the background atmospheric profile by the layering of profiles, which implies that if atmospheric profile offers information at  $N$  altitudes, then there will be  $N - 1$  layers in aerosol profile.

In DAK model, the optical properties of the aerosol and cloud for each layer can be specified by the parameters *baer* and *aaer*. *baer* is aerosol extinction optical thickness (AOD) while the latter one represents aerosol single scattering albedo. The profile is also regarded as rectangular to simplify calculation. It is important that *baer* is the aerosol extinction optical thickness per 1 kilometer. So when layering is not evenly done, namely the distance between two layers is not 1 km, scaling has to be performed to derive the absolute AOD.

By looking into the ground-based remote sensing dataset from AErosol RObotic NETwork (AERONET), a approximate aerosol and cloud condition can be estimated. AERONET only offers information at the site location Berlin-FUB (52.458N, 13.310E). As a result, the magnitude of AOD cannot be absolutely precise at every location but more information helps to narrow down the range of variability and uncertainty. Besides, level 1.5 data instead of level 2 data due to the lack of availability on the database on the same day. Level 1.5 data are automatically cloud cleared but not quality assured. Figure 4.7 shows the time series of aerosol optical thickness in April 2016, the average AOD of the month at wavelength 440nm is 0.147, while the magnitude varies from 0.3 to 1.2. Furthermore, it is indicated in Figure 4.8 that on 21 April, AOD ranges from 0.06 to 0.125 with the daily mean of 0.085. Eight AOD values ranging from 0.05 to 0.4 with a step of 0.05 are sampled to examine the impact of AOD on air mass factor as well as vertical column density.

Ozone monitoring Instrument (OMI) also observes the aerosol property parameters on a daily basis in a global scale, including aerosol extinction optical depth and aerosol single scattering albedo.

OMAEROe which stands for OMI/Aura Multi-wavelength Aerosol Optical Depth and

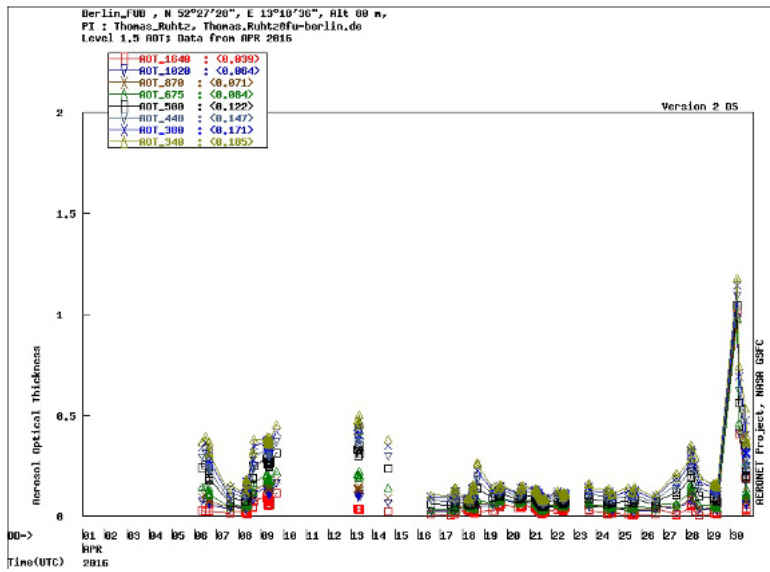


Figure 4.7: Aerosol optical depth in April, 2016 with averaged AOD of each day.

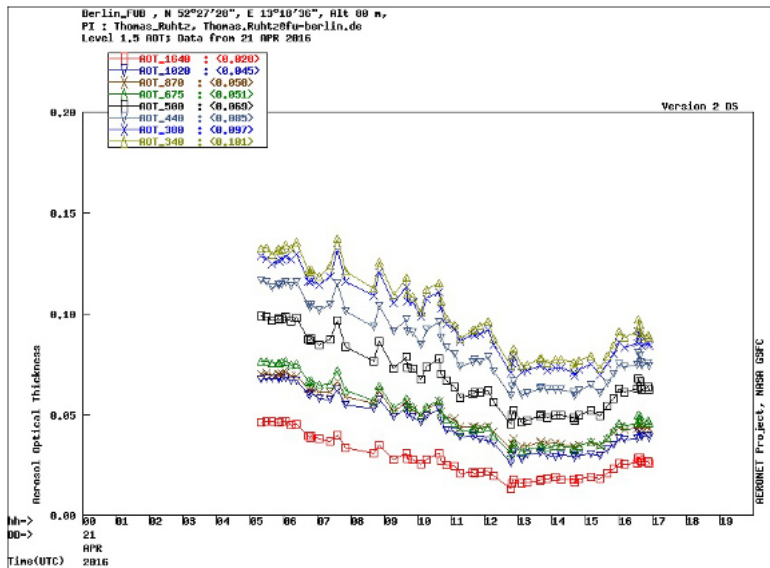


Figure 4.8: Aerosol optical depth on 21 April, 2016 with averaged AOD of each hour.

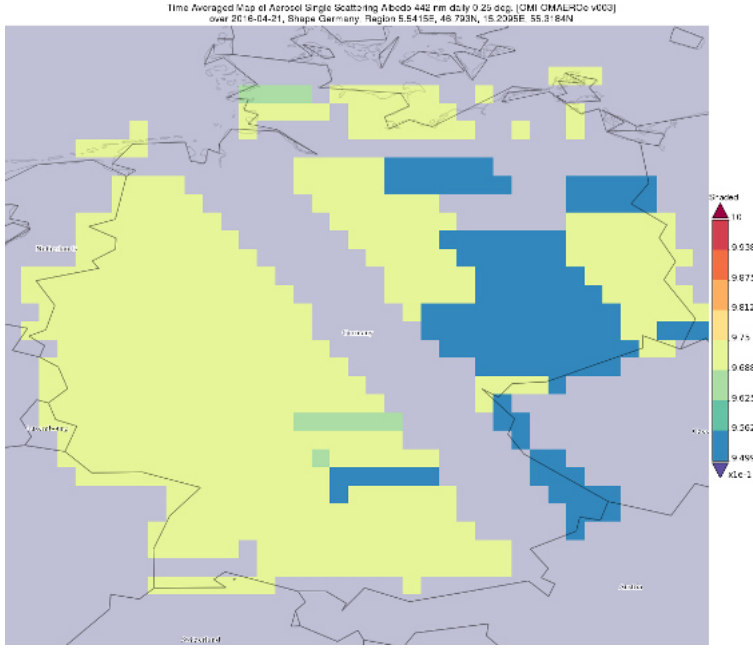


Figure 4.9: The Averaged Map of Single Scattering Albedo from OMI Measurement on 21 April, 2016.

Single Scattering Albedo product contains the daily measurements of aerosol property conducted with five wavelengths (342.5, 388.0, 442.0, 463.0, 483.5 nm) on 0.25 degree  $\times$  0.25 degree grid. It is apparent that 442 nm should be used since it is the closest, almost identical spectra to the choice of the wavelength in DAK simulation. Therefore, a second validation for the choice of parameters can be confirmed with horizontal comparison.

Due to the fact that OMI has a relatively coarse spatial resolution, a much larger area (Region 5.5415E, 46.793N, 15.2095E, 55.3184N) is selected for visualization. As can be seen in Figure 4.9, Aura OMI measurement on that day offers several pixels that cover the most part of Germany but only a few in Berlin region. Some pixels are missing due to bad measurement quality or strips between two satellite orbits. The averaged single scattering albedo on 21 April in Berlin region ranges from 0.95 to 0.98. Figure 4.10 demonstrates the mean aerosol extinction optical thickness from OMI measurements in Germany. We can see that the larger magnitude of AOD is distributed in the west and southwest region where most of the industrial cities are located such as Düsseldorf, Cologne, Stuttgart and Munich, while the AOD in Berlin is around 0.06. But it also could be due to weather because aerosol optical thickness is highly affected by weather.

In order to have a quantified idea of these two parameters, the histograms of single scattering albedo and aerosol extinction optical thickness on 21 April, 2016 are presented in Figure 4.11. Aerosol extinction optical thickness is mostly distributed between 0 to 0.15, while the largest numbers of AOD magnitude can be found between 0 to 0.06, which corresponds to the inference from the map in Figure 4.10. For single scattering albedo, it is dominated by large values. In order to keep the size of the Look-up Table small, the



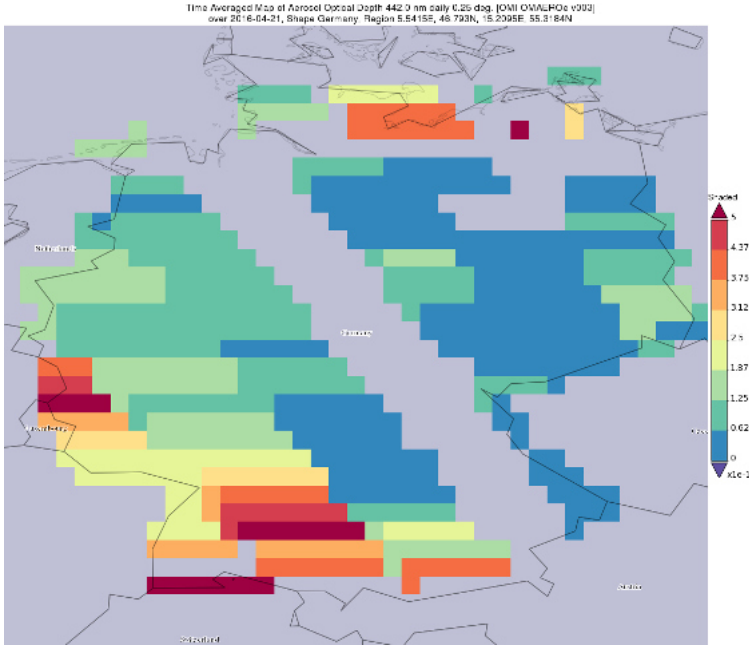


Figure 4.10: The Averaged Map of Aerosol Extinction Optical Depth and from OMI Measurement on 21 April, 2016

single scattering albedo used in the model is a single value 0.98.

However, regarding the aerosol layer height, since we do not have precise measurements for the vertical distribution of aerosol, several common values are chosen, 0.2, 0.5, 0.8 and 1.6 km to study the influence of the aerosol profile.

## GEOMETRY

In DAK model, geometric property involved in simulation comprises solar zenith angle, viewing zenith angle and relative azimuth angle, which illustrate the position relationship among the sun, target and instrument as in Figure 4.12.[43] The solar zenith angle is the angle between the zenith and the center of the sun's disc. The solar zenith angle at one ground position can be determined by time and coordinates of the point of interest. The solar zenith angle is calculated by Astral python package in this project. The time series of solar zenith angle at AERONET site Berlin-FUB (52.510N, 13.281E) is visualized in Figure 4.13. Consequently, solar zenith angle of 0, 4, 5, 8, 10, 12, 15, 20, 25, 30, 35, 40, 45, 50, 55, 60, 65, 70 degrees are chosen in the model to cover different time because the measurement took place in a relatively long period from 9 am to 5 pm (shown in Figure 4.4). DAK model automatically uses the same values for viewing zenith angle from solar zenith angle. However, from the instrument record, the viewing angle of Spectrolite instrument during stable flight is averagely 7.3 degrees in across track direction. Viewing zenith angle is small enough to be simplified to 0 also because of computational convenience, which means that the aircraft is measuring in nadir looking direction.

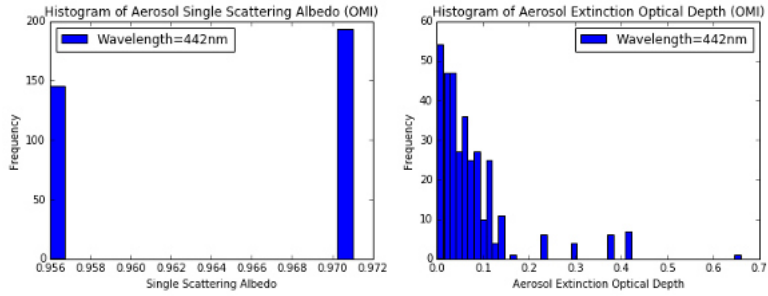


Figure 4.11: Aerosol Extinction Optical Depth and from OMI Measurement on 21 April, 2016

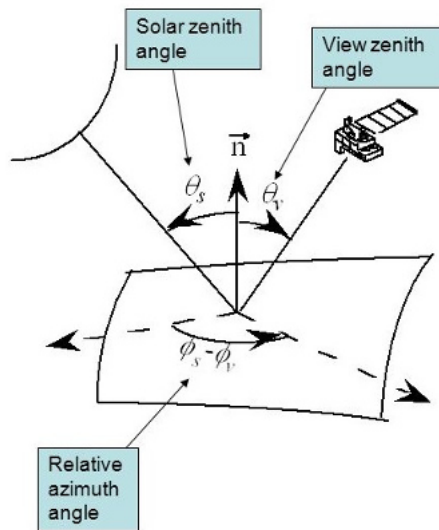


Figure 4.12: Observation Geometry during Airborne Measurement.

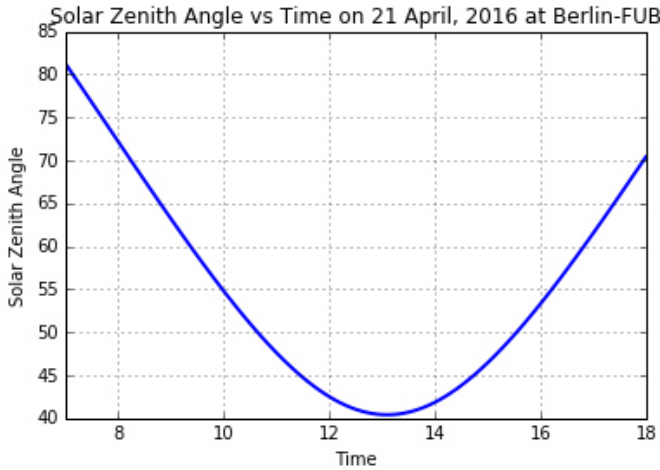


Figure 4.13: Solar Zenith Angle at Berlin-FUB on 21 April, 2016

Beside, if the viewing angle of the aircraft is assumed to be nadir, the magnitude of relative azimuth angle will not have any influence on the output any longer, which save a lot of processing time and reduces the size of Look-up Table.

### SURFACE REFLECTANCE

Surface reflectance also needs to be defined in the input file. A relatively denser selections of surface reflectance between 0 and 0.3 are made in order to have a more precise estimate of surface reflectance after simulation by radiance matching. In addition, some (semi-)extreme condition are also taken into consideration, thus 0.4, 0.6, 0.8 are also included in the surface reflectance used in the input.

## OVERVIEW OF INPUT PARAMETERS

Table 4.2 lists all the parameters for combinations of which radiances are simulated. Loops are set up with Python scripting to generate Look-up Table for further use. Within each loop, output file is derived with radiances of all geometric conditions under the circumstance of the specific combination of other parameters. After reading the output file of each loop, simulated radiances are retrieved and appended in another .txt text file which will be Look-up Table in the end. When the simulation finishes, the Look-up Table can illustrate modeled radiance as function of various input parameters. It took two days for processing even after careful selection of variables, which once again explains the importance of investigating local environmental condition beforehand. The Look-up Table is technically a multi-dimensional dataset with normalized radiance from DAK modeling as function of all various parameters mentioned in Table 4.2. Therefore, given adequate number of parameters, with the help of multi-dimensional linear interpolation, an estimated radiance can be obtained.

In order to perform sensitivity study, we change the magnitude if one parameter

Parameters	Units	Values
Wavelength	<i>nm</i>	440
Output Altitude	<i>km</i>	3.1
Surface Temperature	<i>K</i>	291, 300
Surface Pressure	<i>hPa</i>	1015
Surface Reflectance	-	0.01, 0.02, 0.04, 0.08, 0.12, 0.16, 0.20, 0.24, 0.30, 0.40, 0.60, 0.80
NO <sub>2</sub> Perturbation Height	<i>km</i>	0.1, 0.5, 0.9, 1.0, 1.25, 1.5, 1.75, 2.0, 2.9, 2.97, 3.13, 3.2, 4.0, 5.0, 7.0
NO <sub>2</sub> Perturbation Depth	<i>km</i>	0.1
NO <sub>2</sub> Perturbation	<i>molec/cm<sup>2</sup></i>	0, 1e16
Aerosol Optical Thickness	-	0.05, 0.1, 0.15, 0.2, 0.25, 0.3, 0.35, 0.4
Single Scattering Albedo	-	0.98
Aerosol Layer Height	<i>km</i>	0.2, 0.5, 0.8, 1.6
Solar Zenith Angle	<i>degree</i>	0, 4, 5, 8, 10, 12, 15, 20, 25, 30, 35, 40, 45, 50, 55, 60, 65, 70
Viewing Zenith Angle	<i>degree</i>	0, 4, 5, 8, 10, 12, 15, 20, 25, 30, 35, 40, 45, 50, 55, 60, 65, 70
Relative Azimuth Angle	<i>degree</i>	0, 30, 60, 90, 120, 150, 180

Table 4.2: The choices of inputs for different parameters in DAK program.

while the others keep constant, so that the its impact on modeled radiance/ Box-AMF can be determined. It has to be noted that the selection of references is not related to the condition in Berlin during the measurement. Because the purpose of sensitivity study is to demonstrate and visualize the effect of the parameters by changing the parameter of interest while the others remain the same values which are called references. These references are demonstrated in Table 4.3, only parameters with more than one variable are listed.

## SENSITIVITY STUDY IN RADIANCE OUTPUT

After DAK Look-up Table is generated, a further sensitivity study is performed to investigate and visualize the relationship between modeled radiance from DAK simulations and other parameters.

### GEOMETRY

Figure 4.14 and 4.15 indicate that along with the increase of solar zenith angle or viewing zenith angle, radiance received by the sensor will become larger as well. Besides, exponential tends can also be observed in the two plots.

However, for relative azimuth angle, received radiance will descend first from 0 degree to 90 degrees since the direction that sensor looks is changing from against sunlight when received radiance is the most, to perpendicular to the sunlight. After reaching the

Parameters	Units	References
Surface Temperature	$K$	300
Surface Reflectance	-	0.02
Aerosol Optical Thickness	-	0.35
Aerosol Layer Height	$km$	0.5
Solar Zenith Angle	$degree$	60
Viewing Zenith Angle	$degree$	60
Relative Azimuth Angle	$degree$	90

Table 4.3: The references of different parameters in DAK program for the comparisons of results.

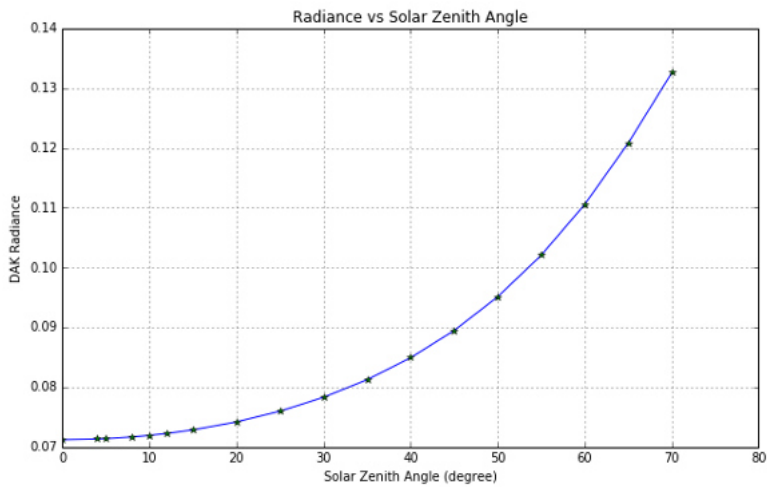


Figure 4.14: DAK Radiance Output as function of Solar Zenith Angle.

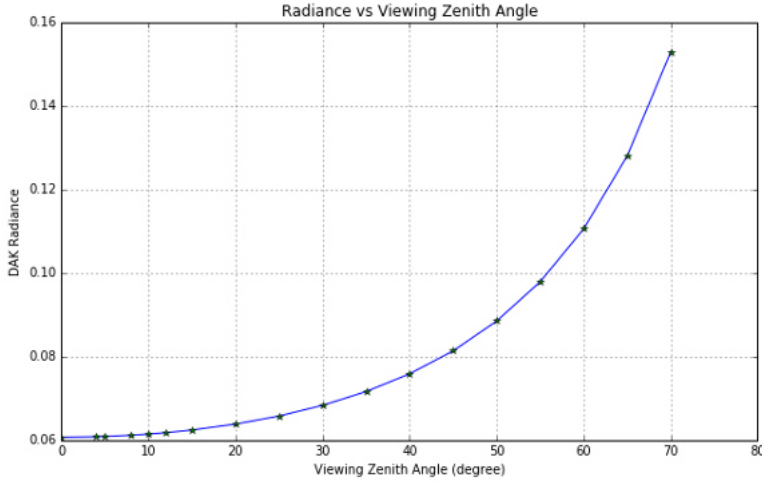


Figure 4.15: DAK Radiance Output as function of Viewing Zenith Angle.

bottom at 90 degrees, received radiance rises up again but will not be as large as 0 degree, because the sun and the sensor are at the same side of the target.

### SURFACE REFLECTANCE

Figure 4.17 show that surface reflectance is significantly related to received radiance, which can be seen from the change scale of simulated radiance output. Compared to geometric parameters, one difference is that the increase of modeled radiance caused by surface reflectance shows nearly a linear trend. However, it is not linear because when surface reflectance is larger, more photons will be scattered to the atmosphere and thus more photons might be sensed by the instrument after multiple scattering. Additionally, the influence of surface reflectance is more obvious with received radiance increasing from 0.1 to approximately 0.75. Because surface reflectance directly impacts the amount of radiance that is scattered by the surface which is the main source of radiance received by the sensor. However, if we look at the y axis radiance, it does nt start from 0, which means that when there is no reflectance from the surface, there is still radiance measured because photons can also be (multi-)scattered by air molecules and be sensed by the instrument.

### AEROSOL PROFILE

Aerosol also contributes to the radiance received by the sensor as a result of scattering, absorption and reflection, this part of the radiance is called aerosol radiance. [44] The scattering of aerosol can be quantified with single scattering albedo. As is described previously, the single scattering albedo is considered to be 0.98 which is considerably high, which indicates the impact that aerosol has on the radiance. When there is a thicker aerosol layer, or extinction optical depth gets larger, more radiance will be scattered by aerosols, thus radiance increases as well, which is clarified in Figure 4.18 and 4.19.

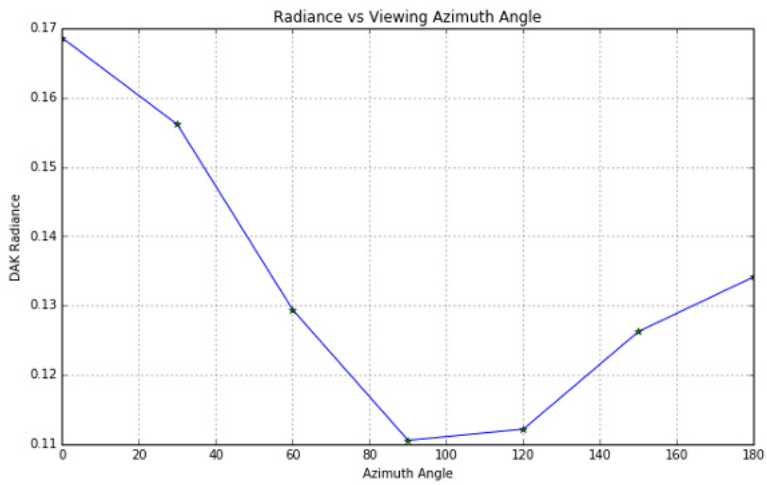


Figure 4.16: DAK Radiance Output as function of Relative Azimuth Angle.

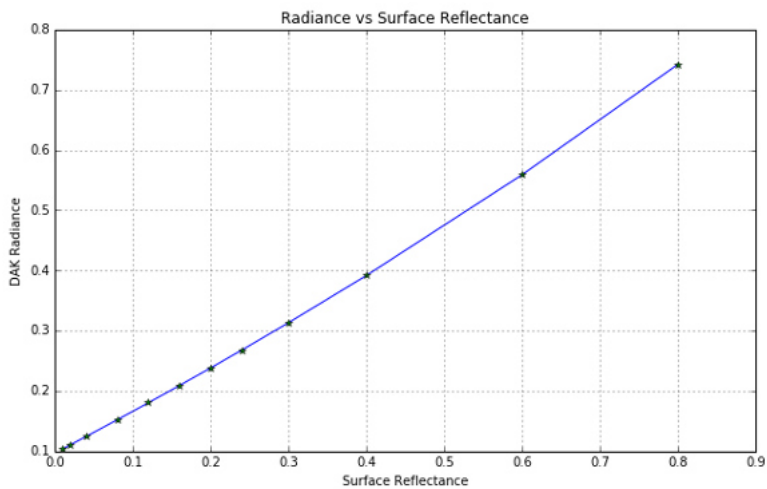


Figure 4.17: DAK Radiance Output as function of Surface Reflectance.

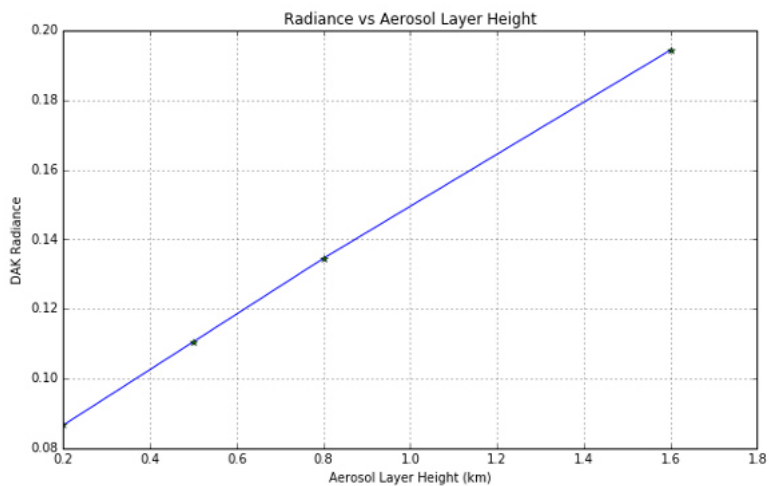


Figure 4.18: DAK Radiance Output as function of Aerosol Layer Height.

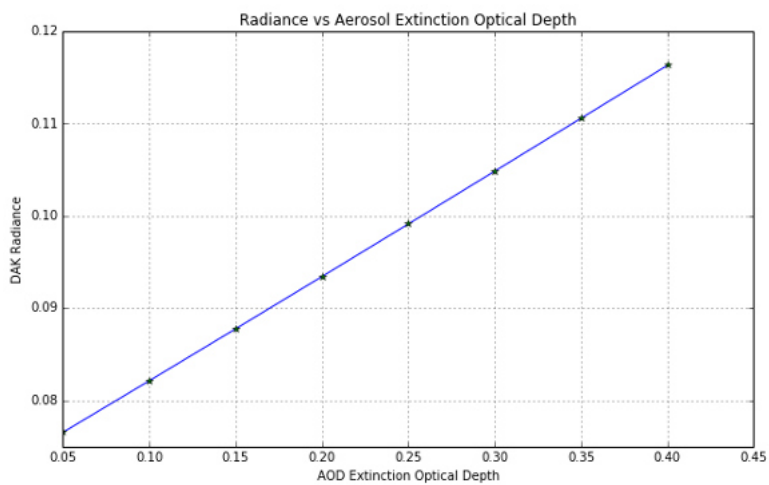


Figure 4.19: DAK Radiance Output as function of Aerosol Extinction Optical Thickness.



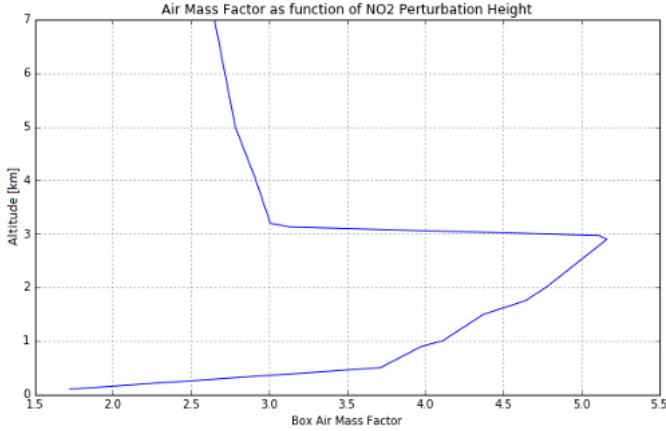


Figure 4.20: The vertical profile of box air mass factor in reference condition

## SENSITIVITY STUDY IN BOX-AMF

Box air mass factor represents the vertically resolved sensitivity to  $\text{NO}_2$  and it is calculated with the method described in Chapter 2. By assuming a  $\text{NO}_2$  perturbation at various altitude and comparing the outputs with those retrieved without perturbation, a vertical profile with x axis representing Box-AMF and y axis as the altitude can be obtained for each combination of parameters. The profile should acquire a shape as the example shown in Figure 4.20.

Below aircraft altitude and close to the earth surface, Box-AMF increase rapidly along with altitude, which means AMF is mostly sensitive to conditions below the aircraft. This is due to the fact that  $\text{NO}_2$  and aerosol extinction profile are at the largest at boundary layer height. However, between the aircraft altitude and aerosol layer, the increase of Box-AMF becomes slower, which means that AMF is less sensitive in this part of the atmosphere because the scattering effect coming from aerosols is reduced. Finally Box-AMF reaches the highest close to the altitude of aircraft (3.1km). Afterwards, it decreases considerably from 5.2 to 3.0, and keeps more or less steady above aircraft altitude. Since above the aircraft, the impact of  $\text{NO}_2$  profile on radiance received by the sensor is quite little. The impacts of different parameters on the vertical profile of box air mass factor is studied below.

### GEOMETRY

Figure 4.22 shows the box air mass factor profiles with different viewing zenith angles. We can see when solar zenith angle decrease ( $\cos(\text{SZA})$  increases), the curves are shifting to the left when they almost start at the same point close to the Earth surface. It shows that solar zenith angle affects the sensitivity to  $\text{NO}_2$  both below and above the aircraft altitude because it has an impact on the light path both below and above the aircraft as is visualized in Figure 4.1. When SZA decreases, the light path of photons also becomes shorter. The interaction of incoming irradiance with air molecules, aerosol, etc. declines as well, which results in a smaller sensitivity due to the reduction of atmospheric light

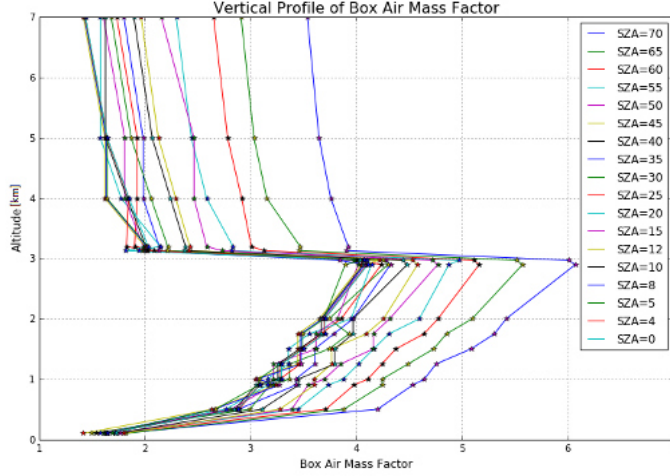


Figure 4.21: Box Air Mass Factor vs Solar Zenith Angle

path. In addition, the peak of box air mass factor is also getting smaller when SZA decreases.

The Box-AMF plot 4.22 of viewing zenith angle demonstrates a similar trend as that of solar zenith angle, which is when viewing zenith angle decrease ( $\cos(VZA)$  increases), the profile of box air mass factor shifts to the left, indicating a smaller sensitivity to atmospheric conditions. However, except that above aircraft height, the curves stabilize in a much closer range (2.3 - 2.8) which nevertheless is still approximately 9% of the maximum Box-AMF. On one hand, the appearance of closer stabilization range is due to the fact that viewing zenith angle almost does not affect the light path above the aircraft. On the other hand, this range is still not small enough to be neglected, e.g. to conclude that viewing zenith angle has no influence on the sensitivity above the aircraft. Because in DAK package, the adopted surface is considered to be Lambertian surface. When an instrument is looking at one point on the surface, the surface reflects light with a cosine angular distribution and each point of a Lambertian surface reflects intensity in a cosine pattern, as is shown in Figure 4.23. [45] It can be inferred that with a fixed solar zenith angle, the scattered intensity will become larger when viewing zenith angle decreases.

It is quite noticeable that there exist some wiggles in the Box-AMF vertical profiles with respect to solar zenith angle and viewing zenith angle. This might be caused by: 1) the discretization in the aerosol extinction optical thickness profile since the profile is divided into several (denser) layers according to the atmospheric profile; 2) the numerical artifacts caused by atmospheric profile where the numerical perturbation in  $\text{NO}_2$  is implemented.

Relative azimuth angle does not have a considerable impact on Box-AMF vertical profile, as is presented in Figure 4.24. Because as mentioned and shown previously in Figure 4.23, DAK regards the surface as Lambertian surface, the scattered intensity does not change noticeably if the solar zenith angle and viewing zenith angle stay the same. The difference of Box-AMF between two extreme conditions (relative azimuth angle is

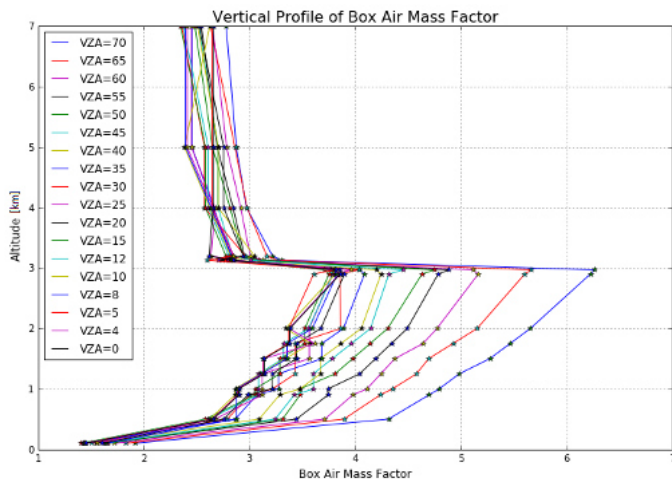


Figure 4.22: Box Air Mass Factor vs Viewing Zenith Angle

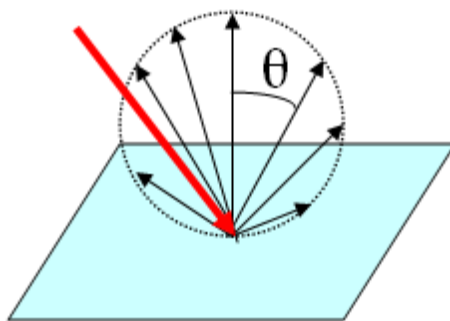


Figure 4.23: The reflection distribution on a Lambertian surface. The scattered intensity reached the highest when viewing zenith angle is zero (the instrument is looking in the nadir).

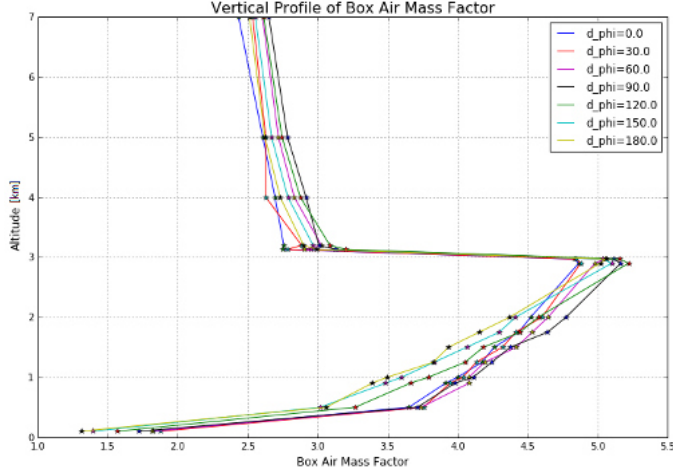


Figure 4.24: Box Air Mass Factor vs Relative Azimuth Angle

0 or 180 respectively) is 0.2 both at aircraft altitude and above, occupying only less than 4% of the peak, which means that the impact of relative azimuth angle on the sensitivity to  $\text{NO}_2$  is not too important for a Lambertian surface.

### SURFACE REFLECTANCE

Surface reflectance is defined as the fraction of incoming solar radiation that is reflected from Earth's surface, it indicates the effectiveness in reflecting radiant energy of the surface. It can be seen from Figure 4.25 surface reflectance mainly affects the magnitude of Box-AMF air mass factor on the surface. When surface reflectance increases, the Box-AMF also rises close to the Earth surface because higher surface reflectance leads to a larger sensitivity. However, the difference of Box-AMF decreases since the influence of surface reflectance attenuates along with altitude. The higher it goes, the less influential surface reflectance is while the effects from other elements stay the same. Therefore, we can see that at aircraft altitude, the difference of Box-AMF has reduced to 0.3 and it is only around 5% of the maximum value. Above the aircraft, the difference even continues to decline, as it moves further from the surface.

### AEROSOL PROFILE

As is visualized in Figure 4.26, aerosol layer height is the first bend in Box-AMF curves where in optically thick aerosol layers, the sensitivity to  $\text{NO}_2$  (Box-AMF) increases more rapidly with altitude below the top of aerosol layer than above. This is because the height of aerosol layer will have effect on aerosol direct radiative forcing due to height dependence of scattering by air molecules for incoming and outgoing (reflectance from surface) solar radiation. So aerosols will result in larger sensitivity to  $\text{NO}_2$ .

However, above the aerosol layer, Box-AMF continues increasing, which means that the sensitivity is still becoming larger, while the magnitudes of Box-AMF in the four scenarios start to aggregate. In addition, at aircraft altitude, the curves of box air mass factor

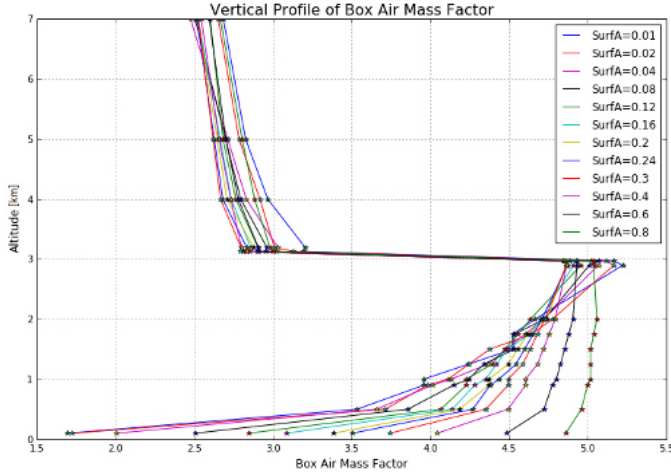


Figure 4.25: Box Air Mass Factor vs Surface Reflectance

reach the peak with almost the same magnitude (5.1) and stabilize at then same value above the aircraft because aerosol layer is to low in altitude to have impact on the sensitivity to  $\text{NO}_2$ .

It has been discussed that aerosol layer height determines the altitude at which the vertical profile of box air mass factor experience the first bend, e.g. the vertical position of the bend. Figure 4.27 shows that aerosol extinction optical depth affects mostly the horizontal position of the bend.

In Figure 4.27, all box air mass factor profiles acquire aerosol layer height of 0.5 km, and that is the altitude at which the first bend occurs as expected. Smaller aerosol extinction optical depth gives rise to smaller Box-AMF (sensitivity to  $\text{NO}_2$ ) at the the top of aerosol layer. However, Box-AMF curves start to emerge above the aerosol layer till they reach the peak with approximately the same Box-AMF value 5.2. In addition, the curves show high identity above the aircraft since aerosol layer no longer has impact.

## SURFACE TEMPERATURE

Surface temperature influences the simulation results by modifying the atmospheric profile of temperature, which can affect the cross-section of a certain absorber ( $\text{NO}_2$  in this project and thus subsequently change the AMF. The temperature-dependent  $\text{NO}_2$  cross section,  $\sigma$ , in UV/ Visible wavelength regions can be calculated at any  $T$ , using a linear regression model. [46]

$$\sigma(\lambda, T) = \sigma_0(\lambda) + \alpha(\lambda) \cdot (T - T_0) \quad (4.1)$$

where constant  $\sigma_0(\lambda)$  is the  $\text{NO}_2$  absorption cross section at temperature  $T_0$  and wavelength  $\lambda$ .  $\alpha(\lambda)$  is a temperature-dependent coefficient describing the change in  $\text{NO}_2$  absorption cross section with temperature  $T$  at wavelength  $\lambda$ .

Figure 4.28 shows the high-resolution laboratory  $\sigma_0(\lambda)$  at 273 K and  $\alpha(\lambda)$  convolved with the MFDOAS instrument transfer function.[47]

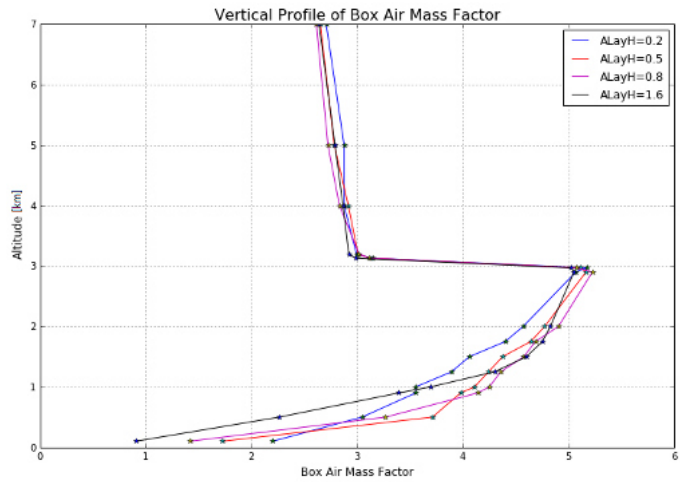


Figure 4.26: Box Air Mass Factor vs Aerosol Layer Height

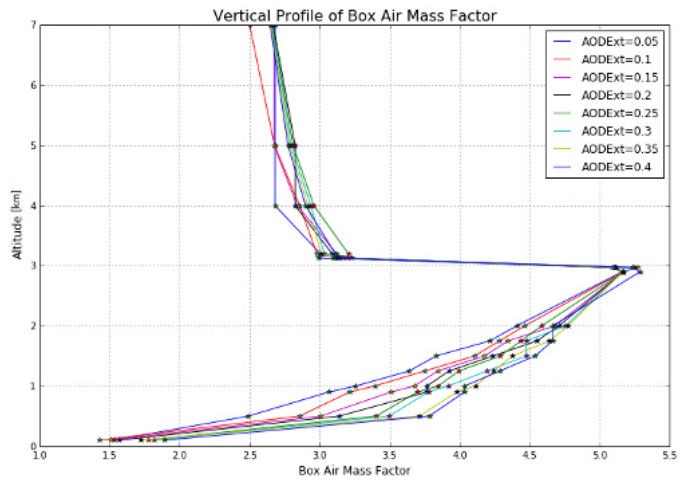


Figure 4.27: Box Air Mass Factor vs Aerosol Extinction Optical Depth

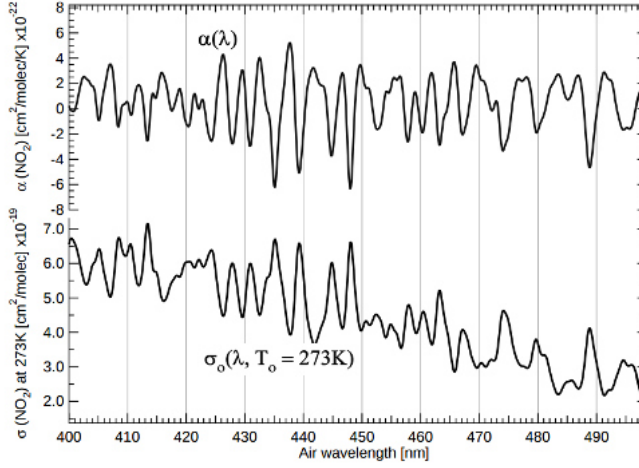


Figure 4.28: NO<sub>2</sub> absorption cross section linear regression model parameters  $\sigma_0(\lambda)$  and  $\alpha(\lambda)$  for  $T_0 = 273K$  [46] and convolved with MFDOAS instrument transmission function (FWHM = 0.83 nm). [47]

It can be seen from Figure 4.28 compared to the NO<sub>2</sub> absorption cross section at temperature  $T_0$ , temperature-dependent coefficient is too smaller with 3-order difference. Besides, the difference in temperature  $T - T_0$  is also not big enough to make a difference. We can conclude that the temperature will only have a negligible effect on the NO<sub>2</sub> absorption cross section as well as Box-AMF. This is verified by the vertical profiles of Box-AMF in different surface temperature in Figure 4.29, the two curves which represent the Box-AMF profiles with surface temperature 293 and 300 K are almost identical.

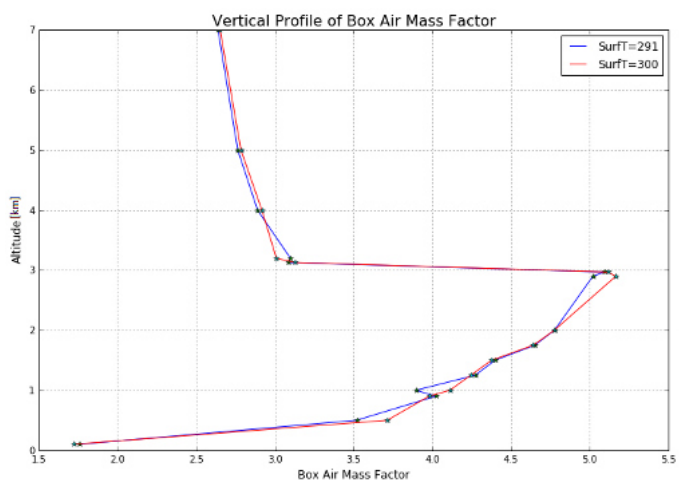


Figure 4.29: Box Air Mass Factor vs Surface Temperature



# 5

## DATA PROCESSING CHAIN

**Sub Question 4:** Specifically in this project, how spectral measurements are processed to NO<sub>2</sub> vertical column densities?

This chapter describes in detail the processing chain that was developed and algorithm involved to process Spectrolite spectral measurements to retrieve NO<sub>2</sub> vertical column densities. The sequence of description is in correspondence with data processing chain. Additionally, the intermediate results are visualized and analyzed after each step.

## FLOW CHARTS OF DATA PROCESSING CHAIN

The flow chart of data processing chain is presented in Figure 5.1.

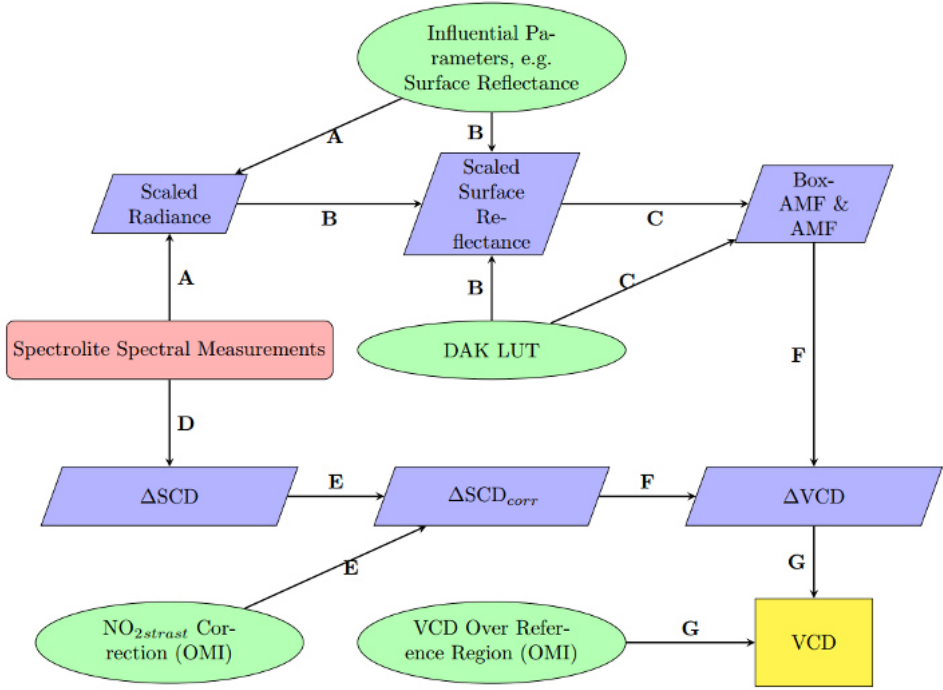


Figure 5.1: The flow chart of data processing chain. Red rounded rectangle represents the primary input of the project which is Spectrolite spectral measurement. Blue rhombuses are the intermediate products obtained during data processing. Green ellipses indicate the other inputs that need to be utilized to obtain the intermediate and final products. These inputs come from other datasets such as ground-base measurements and satellite observations. Yellow rectangle is the final product we want, NO<sub>2</sub> vertical column density.

The flow chart in Figure 5.1 can be summarized into the following steps:

- **A:** The Spectrolite data files contain time and spectral measurements on 21 April during the campaign over the city of Berlin. It is assumed that the surface reflectance is known from Landsat Band 1 measurements over reference area (forests, etc.) where the surface reflectance varies little with respect to viewing direction because Spectrolite and Landsat have different ones, and from place to place, therefore it should be a homogeneous terrain. In order to optimize surface reflectance, scaling factor is derived by comparing measured radiance from Spectrolite measurements and the simulated radiance from DAK modeling using Landsat surface reflectance as input over a forest region. Subsequently, the scalar is applied to all radiance measurements over Berlin. This process is demonstrated in detail in another flow chart in Figure 5.2

- **B:** After the measured radiance from Spectrolite is scaled, the true surface reflectance which is observed by the Spectrolite instrument over the whole region during flights can be obtained by matching the scaled Spectrolite radiance with DAK modeled radiance. Since knowing the two radiances and all other influential parameters during the measurement, the true surface reflectance can be determined from DAK Look-up Table.
- **C:** Given surface reflectance from Step **B** and other parameters such as viewing directions, aerosol profile. etc., by assuming a  $\text{NO}_2$  perturbation with a concentration of  $1 \cdot 10^{16} \text{ mole} \cdot \text{cm}^{-3}$  within a layer of 100 meters thick at a certain altitude, radiances received by the instrument with and without  $\text{NO}_2$  perturbation at background atmospheric profile can be retrieved from DAK Look-up Table. Subsequently, Box-AMF which indicates the sensitivity to  $\text{NO}_2$  can be calculated and so can air mass factor after assuming a  $\text{NO}_2$  profile shape.
- **D:** The original radiance measurements contained in Spectrolite data files are calibrated by an appropriately chosen fit window. Subsequently differential slant column density is calculated with DOAS method with the help of cross section profiles of various trace gases. In addition, the data are georeferenced and gridded with the geolocation file froms GPS measurements during flights.
- **E:** Differential slant column density obtained by DOAS method has to be corrected for the impact of stratosphere. Since the time span during the measurements lasts from around 8 am to 5 pm, solar zenith angle has varied to a large extent (from 72 degrees at 8 am to 40 degrees at noon), resulting in different light path lengths in the stratosphere, which has an influence on  $\text{NO}_2$  stratospheric slant column density.
- **F:** After correction, AMF simulated from DAK model is applied to slant column density to retrieve differential vertical column density underneath the aircraft.
- **G:** Tropospheric vertical column density over the reference region used in DOAS method is obtained from Aura OMI observations and added to the differential VCD over the whole area to obtain absolute vertical column density which is the final product of this project,

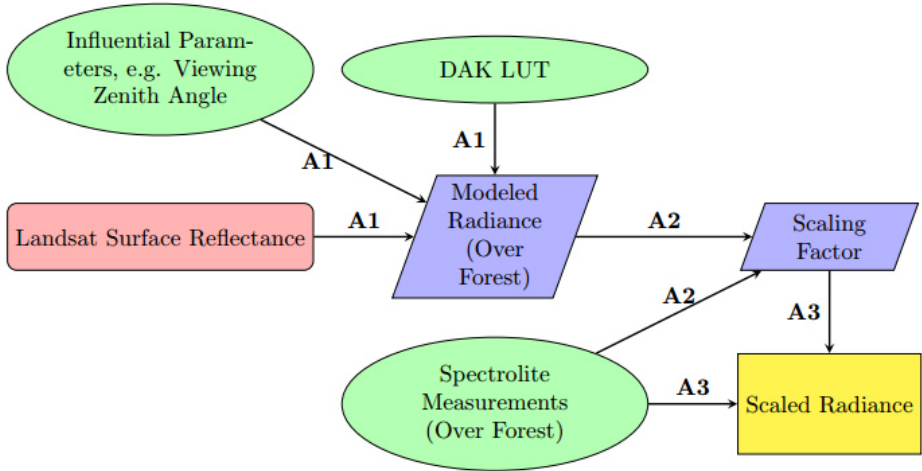


Figure 5.2: The flow chart of scaling process. Red rounded rectangle represents the surface reflectance product from Landsat observation which the primary input of scaling. Blue rhombuses are the intermediate products. Green ellipses are the other inputs from Spectrolite measurements or DAK radiative transfer modeling that need to be utilized to obtain the intermediate and final products. Yellow rectangle is the final product scaled radiance.

The process shown in Figure 5.2 to derive scaling factor and scaled radiance can be described as below:

- **A1:** It is assumed that in a homogeneous region (forest) where the surface reflectance is affected little by viewing directions and from place to place, the surface reflectance is already known from Landsat Band1 observations. After it is substituted into DAK Look-up Table together with other influential parameters, the radiance in a specific scenario during measurement can be modeled.
- **A2:** The histograms of modeled radiance and measured radiance from Spectrolite over forest are plotted. They should have a similar pattern in shape except that the horizontal position might be shifted. The scaling factor is subsequently calculated by taking the division of the medians of modeled and measured radiances.
- **A3:** After scaling factor is obtained, it is applied to the measurements of the whole region to derive scaled radiance for true surface reflectance retrieval in Step B.

## SPECTROLITE DATA PROCESSING

Spectrolite measurements were preprocessed to Level 1b data and provided by TNO which collaborated with TU Delft and KNMI during the campaign. Each data file contains four variables, namely 'time', 'ImageSpectral', 'Spectral' and 'ImageGray' measured over an area with the size of 74 pixels in across-track (viewing) direction and 720 pixels in along-track (flying) direction.

Among the four variable in the Level 1b file, 'time' is a MATLAB datenum array in that represents the time at which the measurement is taken as the number of days from

January 0, 0000. 'Spectral' demonstrates the spectrum composed of 1106 wavelengths utilized during measurement at every pixel in across-track direction. 'ImageSpectral' is a 3-dimensional matrix of radiance measurement of the corresponding area (which acquires a size of 74 pixels by 720 pixels) with the spectrum of 1106 wavelengths at each pixel, therefore this 3D matrix has the size of  $74 \times 720 \times 1106$ . 'ImageGray' averages radiance measurement along the spectral direction so it can help to visualize the surface feature for manual selection, etc.

## GEOREFERENCING AND DATA GRIDDING

As is mentioned above, the Spectrolite data files do not contain coordinates information, therefore georeferencing has to be performed in order to relate the measurements with Earth ground pixels. During Spectrolite measurement, GPS provided time, longitude, latitude, altitude as well as the rotation of aircraft during measurement at a dense time interval of around 0.125s.

The altitude during measurement has been plotted in Figure 4.4 in Chapter 3. It indicates that the altitude of aircraft rises approximately from 9 am to 9:15 and from 13:50 to 14:10, stays steadily both for slightly more than two hours and descend to ground level. Tropospheric  $\text{NO}_2$  columns are measured at 3km altitude which contains mostly information about the vertically integrated amount of  $\text{NO}_2$  in the boundary layer, hence they provide an estimate of boundary layer pollution. [18]

Figure 5.3 shows the rotation of aircraft which is indicated by parameters roll, pitch and yaw in three axes. [48] It can be seen that yaw influences the viewing azimuth angle while roll and pitch have impacts on the viewing zenith angle. Figure 5.4 to 5.6 visualize the time series of the three rotation indicators together with aircraft altitude. Due to the instability during the climb and landing of aircraft, all three parameters fluctuate to a relatively larger extent compared to the other time of the period. When the aircraft starts flying stably, regular and sudden peaks can be noticed in roll and pitch because of the turning of aircraft, which is verified by yaw plot in Figure 5.6. Using the direction of the first stable flight as reference, after the yaw of aircraft stays 0 degree for about 10 minutes, it suddenly jumps to 180 degrees because it is turning to the back. Subsequently yaw changes to -180 degree for another 15 minutes since the aircraft is flying back in the opposite direction as the reference.

In order to grid the data on the Earth surface with measured latitude and longitude from GPS, the two time records from Spectrolite and GPS measurements are utilized. To allocate a GPS location to each measurement taken by Spectrolite instrument, a linear interpolation is performed to GPS time stamps with Spectrolite time stamps to synchronize the two data sets.

The datenum in the radiance measurement is translated into number of hours from 0 o'clock on 21 April, 2016 locally in Berlin. However, the time in GPS geolocation file is written as the number of hours from 0 o'clock on the same day in UTC time zone, which has to be converted into Berlin local time. Berlin is located in UTC+1 time zone with one-hour Daylight Savings Time in April therefore it is 2 hours ahead of UTC+0. After the time difference is added to GPS time stamps, the two time stamps are synchronized with linear interpolation and thus the coordinates can be assigned to the Spectrolite measurements.

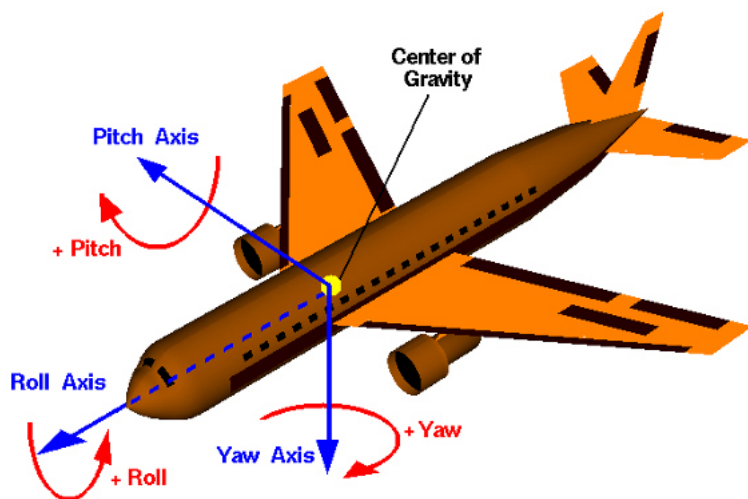


Figure 5.3: The rotation visualization of aircraft. [48]

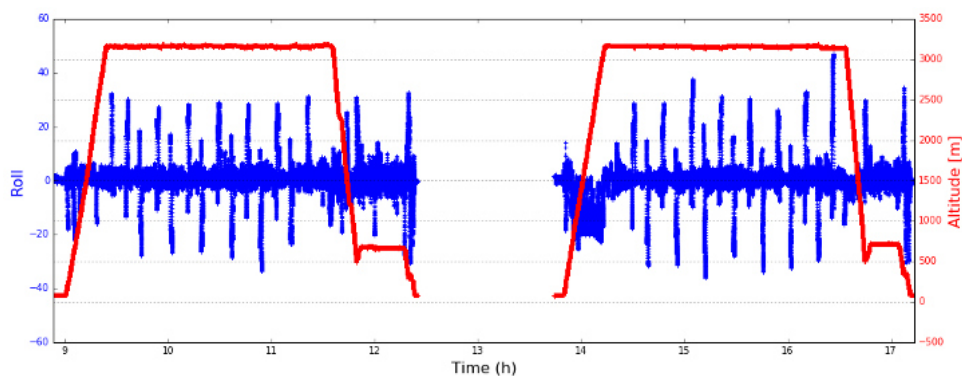


Figure 5.4: Roll and flight altitude as function of time

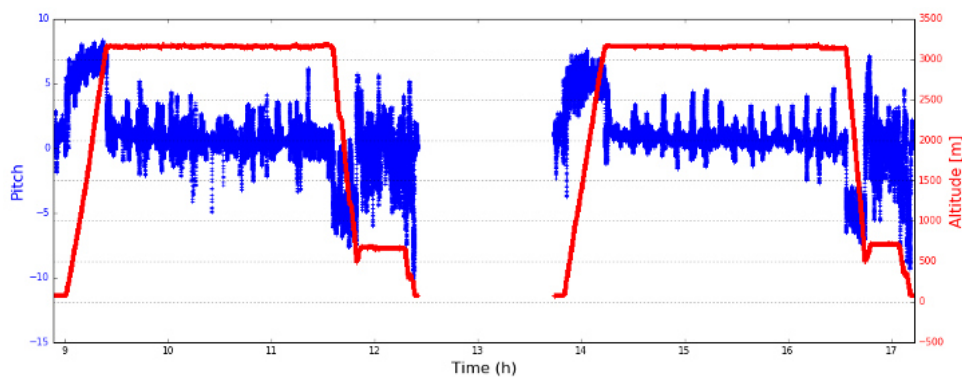


Figure 5.5: Pitch and flight altitude as function of time

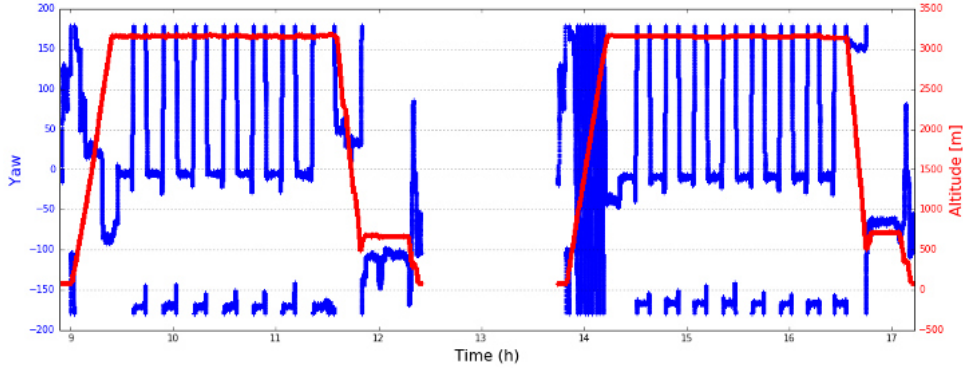


Figure 5.6: Yaw and flight altitude as function of time

It is assumed that GPS measures the coordinates of every center pixel in across-track direction. With Basemap package in Python, flight path from GPS measurement can be integrated with satellite images and visualized in Figure 5.7 to offer a better knowledge about surface features along the flight path. It can be seen from the plot that the two flights cover the city of Berlin and surrounding areas within the window of approximately from 52.3N to 52.6N and from 13.2E to 13.7E with the range of around  $40\text{km}^2$ . There are also some routes that exceed this range and by comparing to the time record, we can know that they exist because of the climb and landing of the aircraft. In addition, the flight routes almost overlap within, which means that the aircraft repeat the path in order to perform the measurements twice.

With the tie series of aircraft altitude in Figure 4.4, the measurements during stable flight can be selected and categorized into two groups, one contains the valid measurement in the morning and the other one includes afternoon observations. The flight paths of two groups are illustrated in Figure 5.8 and 5.9. As is demonstrated, each flight is comprised of several back-and-forth measurements in North-South direction and each single North-South movement is about 40 km long. When the aircraft reaches every end in North/South direction, it turns back with a bit shift to East/West direction.

As mentioned previously, GPS is assumed to measure the coordinates of central point in across-track direction along the flight. Coordinates of pixels in the cross-track (viewing) also need to be calculated in order to georeference other points. However, there are an even number (74) of pixels in across-track direction, so the middle point is equivalent to the middle of the 37th and 38th pixel. Figure 5.10 demonstrates the geometry of data gridding. The blue dots represent Spectrolite measurements, the position is assigned as the center of each pixel. Thus there are 37 dots on both sides of the vertical axis in across-track direction. Once we know the altitude of aircraft  $H$  and the angle from one pixel to the vertical axis  $\alpha$ , the distance from the center point in across-track direction to the center of this pixel  $d$  can be calculated by triangulation in Equation 5.1:

$$d = H \cdot \tan(\alpha) \quad (5.1)$$

The viewing angle of Spectrolite instrument is 8.3 degrees. We assume that the air-

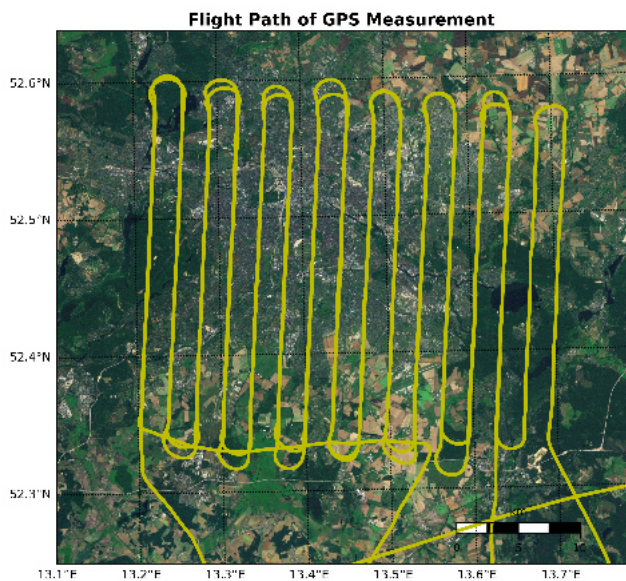


Figure 5.7: Flight Path from GPS Measurement



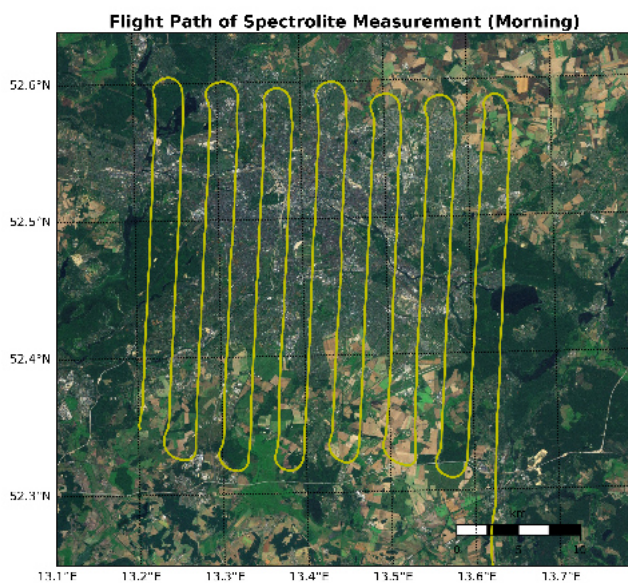


Figure 5.8: Flight Path in the Morning

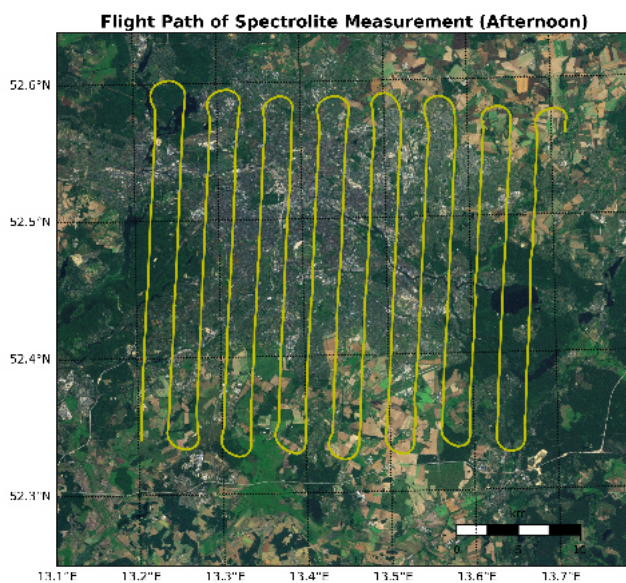


Figure 5.9: Flight Path in the Afternoon

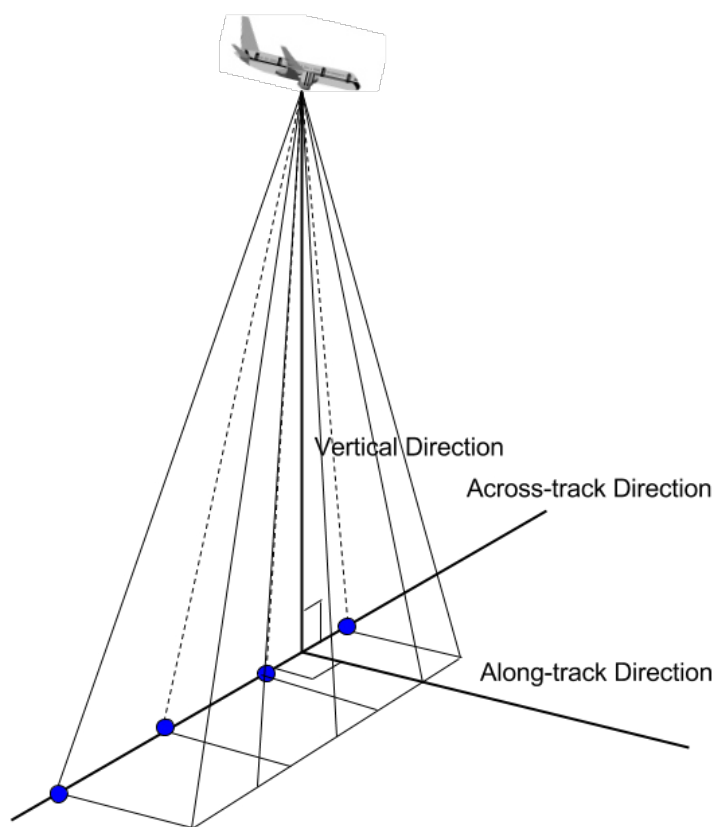


Figure 5.10: Geometry of data gridding. Each blue dot represents one spectral measurement in across-track direction

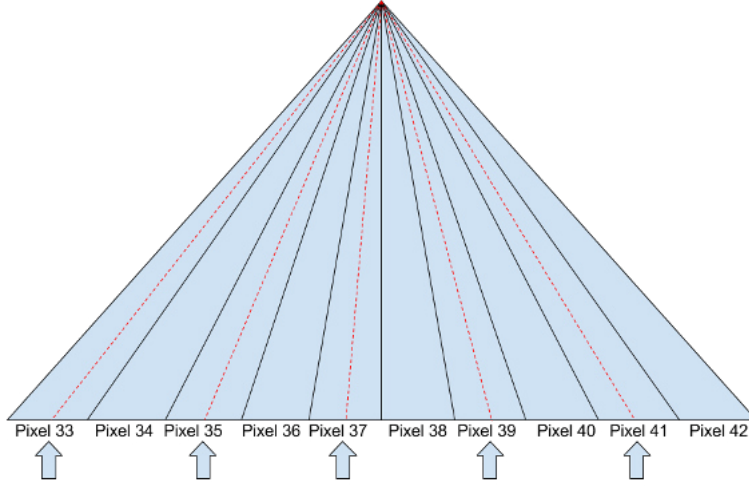


Figure 5.11: The assigning of pixels coordinates in across-track direction

craft is always looking down in nadir direction, which means the instrument observes 4.15 degrees to the left side of nadir and also 4.15 degrees to the right. With aircraft altitude and the angle to nadir, the distances from each pixel in cross-track direction to the corresponding central point can be obtained with trigonometry. The swath width is therefore  $D = 2 \times 3100 \tan(8.3^\circ/2) = 450m$ . It is also supposed that the 74 pixels in across-track direction divide the viewing angle equally because the magnitude of viewing angle is quite small that the miscalculation of distances from angle errors can be neglected. For example, if the aircraft altitude is 3.1km and the viewing angle of one measurement is regarded as 4.15 degrees instead of 4 degree, the miscalculation of distance would be  $3100 \cdot (\tan 1^\circ - \tan 2^\circ) = 8.16m$ . It has to be point out that later when applying DOAS method, in order to save processing time, only every second pixel in across-track direction are processed instead of all of them. Besides, 24 pixels in along-track direction are also averaged to increase the signal to noise ratio, As a result, for each Spectrolite data file, the size of the intermediate products, averaged radiance and differential slant column density would be  $37 \times 30$ . As is shown in Figure 5.11, pixels with odd numbers are chosen and thus the GPS location is assigned to the center of the 37th pixel, which will cause  $8.3/2/37/2 = 0.056^\circ$  of angle shift but it can also be ignored.

Figure 5.12 shows a few adjacent measurement points in along-track direction. Hypothetically, two of them A and B, acquire coordinates  $(lon_A, lat_A)$ ,  $(lon_B, lat_B)$ . Another two points M and N, are perpendicular to  $\overline{AB}$  and  $d$  km away to the left and to point A. The method to calculate the coordinates of point M and N is described below.

Now, we already know the coordinates of the center A in the across-track direction  $(lon_A, lat_A)$  and the distance from center to a point of interest in across-track direction  $S^{AM} = S^{AN} = dkm$ , the coordinates of that point can be derived if we also know the angle with respect to horizontal direction. A vector pointing to B from A can be derived as  $\overrightarrow{AB} = (lon_B - lon_A, lat_B - lat_A)$ . Since the distance between A and B is quite small,

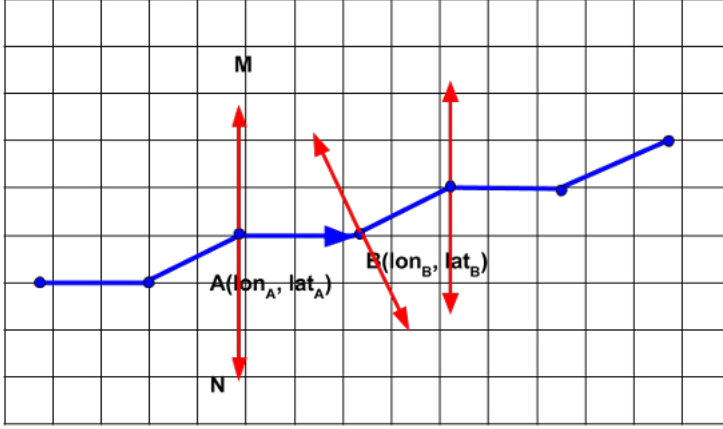


Figure 5.12: Geometry to calculate the pixels in across-track direction. The blue line is the flight path while red vectors point at the points in across-track direction from the center.

the angle of  $\overrightarrow{AB}$  with respect to horizontal direction can be calculated by assuming a flat surface between them:

$$\alpha_{AB} = \arctan\left(\frac{lat_B - lat_A}{lon_B - lon_A}\right) \quad (5.2)$$

In order to obtain the angles of  $\overrightarrow{AM}$  and  $\overrightarrow{AN}$  that are perpendicular to  $\overrightarrow{AB}$  to the left and right, 90 degrees and 270 degrees are added to  $\alpha_{AB}$ . At this point, the shape of the Earth has to be taken into account and it is assumed as a spheroid with a radius of  $R$ . Firstly, longitude, latitude of  $A$  and  $\alpha_{AB}$  are translated into radians. Subsequently, the latitude and longitude of  $M$  can be calculated by:

$$lat_M = \arcsin(\sin(lat_A) * \cos(d/R) + \cos(lat_A) * \sin(d/R) * \cos(\alpha_{AM})) \quad (5.3)$$

$$lon_M = lon_A + \arcsin\left(\frac{\sin(\alpha_{AM}) * \sin(d/R) * \cos(lat_A)}{\cos(d/R) - \sin(lat_A) * \sin(lat_M)}\right) \quad (5.4)$$

$$lat_N = \arcsin(\sin(lat_A) * \cos(d/R) + \cos(lat_A) * \sin(d/R) * \cos(\alpha_{AN})) \quad (5.5)$$

$$lon_N = lon_A + \arcsin\left(\frac{\sin(\alpha_{AN}) * \sin(d/R) * \cos(lat_A)}{\cos(d/R) - \sin(lat_A) * \sin(lat_N)}\right) \quad (5.6)$$

As a result, the coordinates of across-track pixels are retrieved, but it should be noted that since the calculation of the vectors that are perpendicular to the flight direction also depend on two adjacent points in along-track direction, there will be one pixel missing

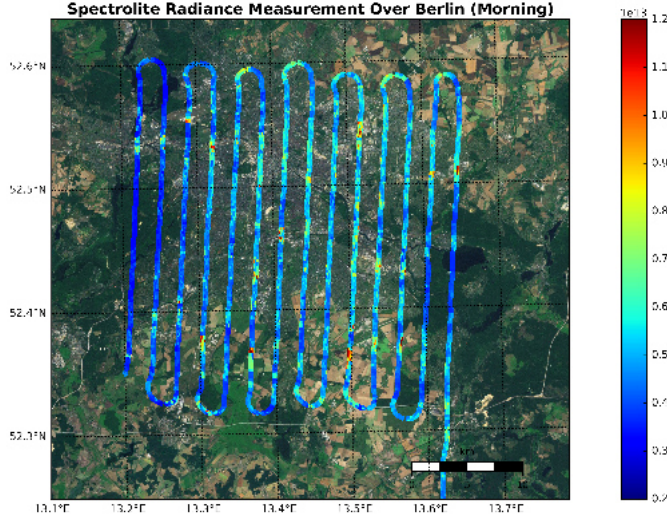


Figure 5.13: Spectrolite Radiance Measurement in the Morning

at the end of the along-track measurement. However, it will not affect the result of the project. The pixel size of the original Spectrolite data file is  $6.08m \times 7.5m$ , while that of the processed intermediate products averaged radiance and DSCD is  $12.2m \times 180m$

Therefore, the Spectrolite radiance measurements can be georeferenced and gridded with Python scripting with the help of **pygmmaps** package. And the radiance measurements in the morning and afternoon over Berlin are visualized in Figure 5.13 and 5.14. It is quite clear that in the afternoon the received radiance is overall larger than in the morning. This might be due to the fact that the solar zenith angle in the afternoon is smaller which results in shorter light path, the intensity therefore gets larger in the afternoon.

After zooming in on the map in Figure 5.15, we can find some patterns with regarding radiance with respect to the surface features. It shows that areas with bright surface tend to have larger radiance. For example, in both plots, groups of houses with white roofs and especially the airport and harbor which are build with light-colored concrete all have much higher radiance and the increase from morning to afternoon is also more considerable in this places because a bright surface increases the sensitivity during the measurement.

### DIFFERENTIAL SLANT COLUMN DENSITY RETRIEVAL

As explained in Chapter 2, differential slant column density is relative to the reference spectrum because there is no direct (irradiance) measurement. As a consequence, we use a radiance spectrum that is measured during the flight at an area which is assumed



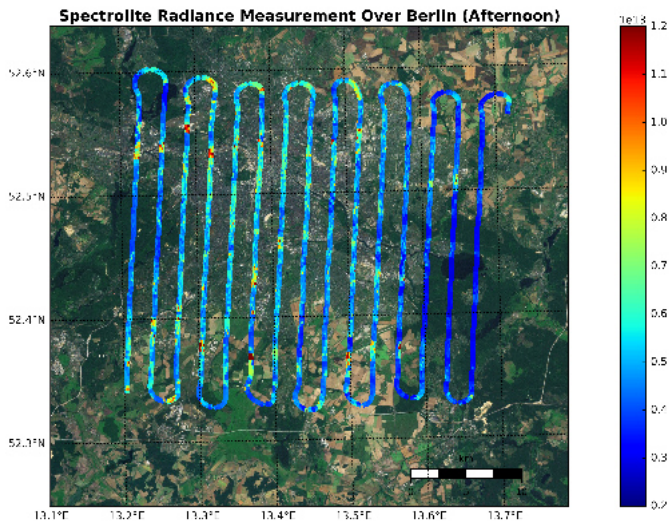


Figure 5.14: Spectrolite Radiance Measurement in the Afternoon

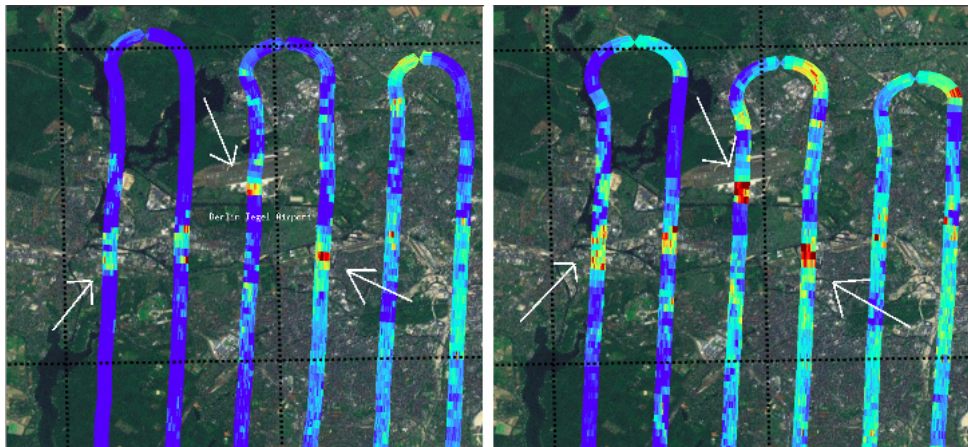


Figure 5.15: Zoomed in radiance map around Berlin Tegel Airport. The white arrows point at the architectures with light-colored roofs, such as harbor and airport.

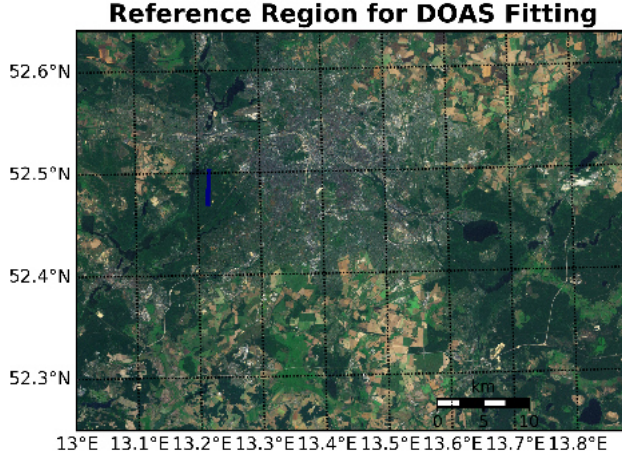


Figure 5.16: The region marked with blue is the reference area used for DOAS fitting.

to only contain a background abundance of  $\text{NO}_2$  (less polluted) as reference because we prefer the differential slant column density to be positive. The reference area is highlighted in Figure 5.16).

As is mentioned early, in order to reduce processing time, only every second pixel is selected, meaning there will be 37 pixels in cross-track direction afterwards. In along-track direction, 24 pixels were averaged to increase the SNR of the spectra and reduce processing time which brings about rather elongated pixels (approximately 12.2m in across track direction and 180m in along track direction).

In order to obtain trace gas column densities, wavelength calibration has to be performed and the slit function also need to be characterized. In the case of satellite remote sensing, this is done by cross-correlating the measured solar irradiance at the top of the atmosphere (for both slit-function and wavelength calibration) and the measured radiance (for wavelength calibration only) with a high-resolution solar irradiance reference spectrum which is also sometimes referred to as Kurucz spectrum.[49] This technique can be applied to airborne (or ground-based) measurements like Spectrolite, however, as is explained previously airborne instruments do not measure the solar irradiance at the top of the atmosphere but the radiances which has gone through the atmosphere after absorption by aerosols and trace gases and scattering from aerosols, clouds (Mie scattering) air molecules(Rayleigh scattering). As a result, we should also take into account the trace-gas absorption and the ring effect which is the solar Fraunhofer lines through Raman scattering in the cross-correlation procedure.

Wavelength calibration is refined by comparing the measured spectrum to solar irradiance reference spectrum, which is realized by simultaneously fitting a third order polynomial describing the pixel to wavelength mapping of the radiance spectrum and (the width of) a Gaussian representing the slit function that is applied to the Kurucz spectrum (Figure 5.17). The fit window is set to from 425 nm to 455 nm. Before differ-



ential absorption cross sections are obtained, the slit function has to be applied to trace gas cross sections.

For each viewing direction, a unique reference spectrum is used, namely the spectrum over the reference region in that viewing direction. This allows minimizing errors in the DOAS analysis caused by spectral miscalibration (e.g. spectral smile) and optical imaging imperfection.

DOAS can be considered as a curve fitting technique where differential absorption cross sections of relevant trace gases are fitted to the differential optical thickness spectrum that can be derived from the radiance spectrum measured by Spectrolite, which is explained in Chapter 2. NO<sub>2</sub> absorption cross sections were subsequently fitted to the differential optical depth derived from the Spectrolite measurements and the reference spectra.

$$\ln\left(\frac{I_0(\lambda)}{I(\lambda)}\right) - P(\lambda) = \sum_i \Delta\sigma_i(\lambda) \cdot N_i^S \quad (5.7)$$

Where  $\ln\left(\frac{I_0(\lambda)}{I(\lambda)}\right) - P(\lambda)$  is the differential optical thickness.  $P(\lambda)$  is a fifth-order polynomial. And  $N_i^S$  is the outcome of DOAS fit - differential slant column density for trace gas  $i$ . Also the differential Ring spectrum is included in the fit, in order to account for the Ring effect caused by inelastic scattering of photons in the atmosphere.

A example of DOAS fit result is shown in Figure 5.17. It can be seen that:

- For this particular case, the analyzed spectrum and reference spectrum have quite a different radiance level. It is probably related to surface reflectance.
- After the wavelength and slit-function calibration, the analyzed spectrum shows good agreement with the solar spectrum
- The total signal is reconstructed reasonably well, although the residual is substantial compared to the fitted signal; the signal is mostly affected by the Ring spectrum while NO<sub>2</sub> comes second and O<sub>3</sub> is quite irrelevant.

Fig. 5.17 shows that it is essential to include the Ring spectrum in the DOAS fit, as it comprises the largest contribution to the fitted curve (10c). This can probably be related to the considerable difference in radiance levels between the spectrum to be analyzed and the reference spectrum (10a): a different radiance level indicates a different surface reflectance hence a different distribution of photon paths. Ozone does not have a relevant contribution to the DOAS fit which is partly due to the relative weak differential ozone absorption structures in this wavelength range, and partly due to the fact that apparently the tropospheric ozone levels do not vary that much between the two spectra.

It is quite remarkable to see the relatively large mean amplitude of the residual compared to the NO<sub>2</sub> signal (indicating an imprecise fit). Fig. 10g shows that averaging five times more spectra considerably improves the NO<sub>2</sub> fit but it will not reveal significantly more spatial detail as this effectively reduces the spatial resolution. A different way to improve the signal to noise ratio of the NO<sub>2</sub> fit is to add more spectra to the reference spectrum. This can be done if the instrument is sufficiently stable (spectrally).

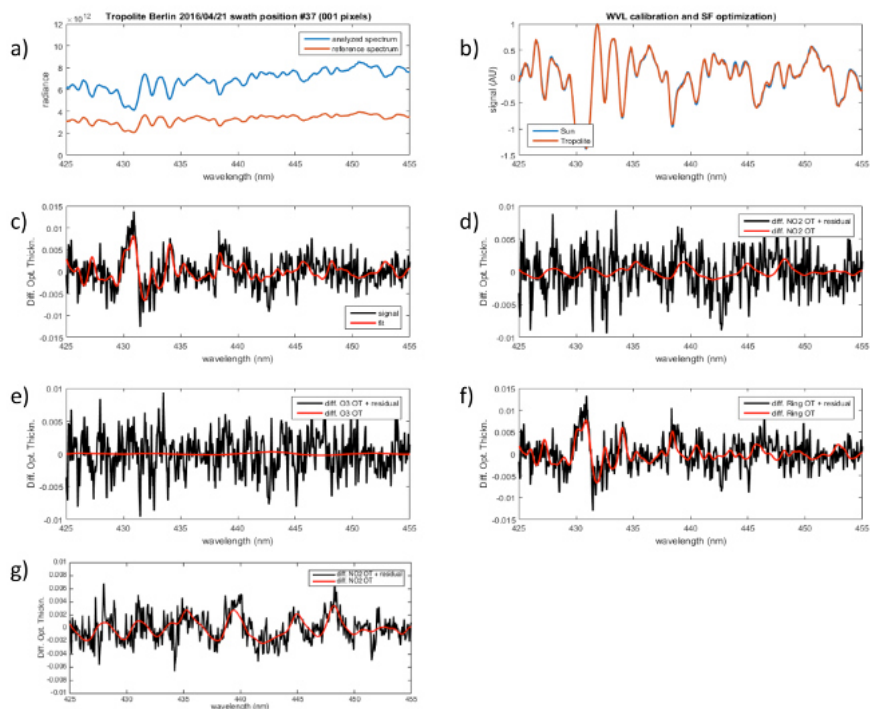


Figure 5.17: An example of DOAS analysis of two spectra (one of which is reference spectrum). a) radiance spectra; b) differential structures of measured spectrum are aligned with differential structures in solar spectrum in wavelength calibration procedure; c) differential optical thickness spectrum compared to fit result (i.e. the sum of the red curves shown in panels d), e) and f); d) fit result for NO<sub>2</sub>; e) fit result for ozone; f) fit result for Ring cross section; g) NO<sub>2</sub> fit result for different spectrum.

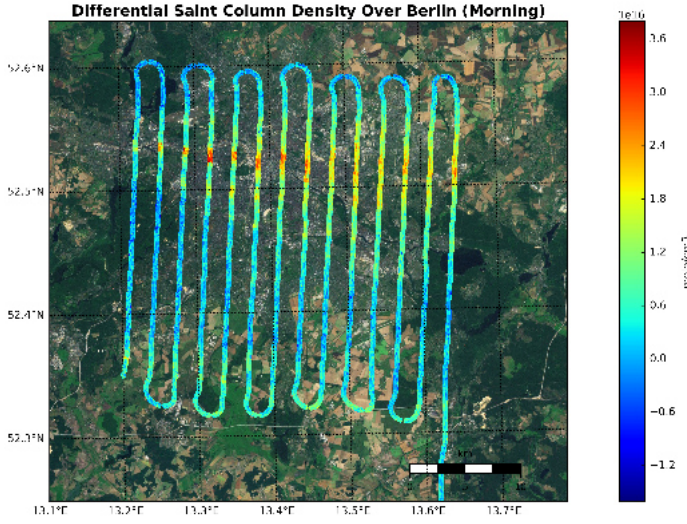


Figure 5.18: Differential Slant Column Density in the Morning

It has to be noted that in Figure 5.17, differential slant column density can be negative. Because the magnitude of dSCD is with respect to the slant column density of the reference region, the SCD at one location can be even smaller than the reference; or it could also be caused by the fitted spectrum or noise.

Figure 5.18 and 5.19 shows the differential slant column density (dSCD) in the afternoon on 21 April 2016 over the city of Berlin and surrounding regions.

## CALCULATION OF SOLAR ZENITH ANGLE

It is illustrated in Chapter 3 that air mass factors are retrieved by using the radiative transfer model - Double-Adding KNMI (DAK). After a look-up table is set up with modeled radiance as function of various parameters, it can be sliced and interpolated to acquire the radiance, and thus to calculate Box-AMF and AMF according to different observing conditions obtained from weather forecast, ground-base observation and other assumptions.

Observation geometry consists of solar zenith angle, viewing zenith angle, and relative azimuth angle, which has been demonstrated in Figure 4.12 in Chapter 4. Atmospheric profile is characterized by aerosol optical thickness, aerosol layer height and single scattering albedo as well as surface temperature and pressure. In addition, surface reflectance also plays a significant role in the radiance.

Among all the parameters above, some of them are consistent and thus can be applied during the whole measurement, while the others change over time because of observation conditions. Fixed parameters are listed in Table 5.1. As is explained earlier,

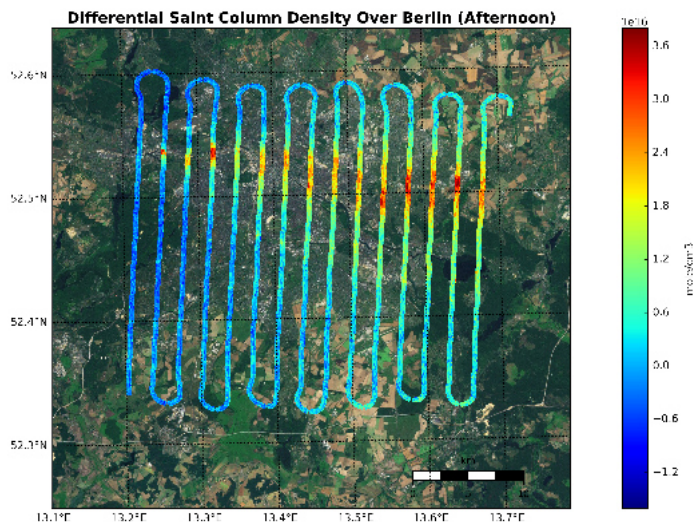


Figure 5.19: Differential Slant Column Density in the Afternoon

the viewing angle is only  $8.3^\circ$ , that is  $4.15^\circ$  in both directions, so viewing zenith angle can be simplified to 0. As a result, relative azimuth angle does not have any impact and therefore can be set to a random value 90. Aerosol optical thickness aerosol layer height and single scattering albedo are estimated to 0.3, 0.5 and 0.98 respectively based on AERONET measurement during the day at station Berlin-FUB, which has been described in Chapter 4 during the generation of DAK Look-up Table. Moreover, by looking into the weather record on that day, surface temperature and pressure are considered as 300K and 1015hPa.

In summary, what we do not know and need to calculate or assume is solar zenith angle, aerosol layer height and surface reflectance.

Hypothetically, since vertical distribution of aerosol is not well known, four condi-

Parameters	Units	Values
Surface Temperature	K	291
Surface Pressure	hPa	1015
Single Scattering Albedo	-	0.98
Aerosol Optical Thickness	-	0.1
Viewing Zenith Angle	degree	0
Relative Azimuth Angle	degree	90

Table 5.1: Parameters that are considered known and fixed during Spectrolite measurements.

tions of aerosol layer height are considered based on time series in the past. They are 0.2, 0.5 and 0.8 km but the aerosol layer height used in this chapter is assumed to be 0.5 km. The result in other conditions will be demonstrated in Chapter 5. Solar zenith angle and surface reflectance are acquired as following.

Solar zenith angle is calculated with Astral Python package and verified with NOAA Solar Calculator from NASA Earth System Research Laboratory.

It is supposedly performed by using module *solar\_zenith* in the package. The needed inputs are the time in *datetime* format, and the longitude and latitude of location.

However, if datetime object is created in a specific timezone (Berlin), *tzinfo* parameter should not be used in the *datetime* constructor. Instead the *localize()* method is applied on the correct *pytz* timezone. For example, a measurement is conducted at 10 am, then the *datetime* is

$$dt = datetime.datetime(2016, 4, 21, 10, 0, 0) \quad (5.8)$$

$$dt = pytz.timezone('Europe/Berlin').localize(dt) \quad (5.9)$$

When being comparing calculated solar zenith angle with those obtained from NOAA Solar Calculator, the two results of solar zenith angle turn out to be quite different and in fact they are complementary. The source code of Astral package is checked, a bug is found out as follows:

```
def solar_zenith(self, dateandtime, latitude, longitude):
    return self.solar_elevation(dateandtime, latitude, longitude)
```

It indicates that the function *solar\_zenith* returns solar elevation angle instead of solar zenith angle. The bug has been corrected and the time series of solar zenith angle on 21 April at Berlin-FUB is plotted in Figure 4.13. In the morning, solar zenith angle decreases until 1pm, with the magnitude dropping from around 80° at 7:30 am to the bottom 40° at 13:00. Afterwards, it rises up again and reaches 70° at 6pm and the plot shows a pattern of a second-order polynomial curve.

## CALCULATION OF SCALED SURFACE REFLECTANCE

The surface reflectance is influenced by many variables such as wavelength, surface roughness and brightness, but we do not have information of surface reflectance during the measurement. The issue is solved by firstly assuming that the surface reflectance is known from Landsat measurements over a reference area with relatively homogeneous surface reflectance properties from place to place, both in space and for different directions. The difference of solar zenith angle and viewing zenith angle during Landsat and Spectrolite observation is less important over such homogeneous surfaces such as forest terrain which more resembles a Lambertian reflector than urban terrain. Afterwards, radiance is obtained by selecting a portion of the LUT and using linear interpolation with assumed surface reflectance values and a variety of atmospheric conditions over the reference region. Scaling factor then is calculated by matching the measured radiance with DAK modeled radiance over the reference area.

Scenario	Aerosol Layer Height(km)	NO <sub>2</sub> Profile Height(km)
A1	0.2	0.1
A2	0.2	0.2
B1	0.5	0.25
B2	0.5	0.5
C1	0.8	0.4
C2	0.8	0.8
D1	1.6	0.8
D2	1.6	1.6

Table 5.2: Scenarios with different aerosol layer height and NO<sub>2</sub> profile height assumptions.

As is mentioned, since we do not have information on the aerosol layer height and NO<sub>2</sub> profile height, some scenarios are assumed to study the influence of those on NO<sub>2</sub> vertical column density retrieval. Aerosol layer height is the inputs chosen for DAK modeling, while NO<sub>2</sub> is considered as half or the same as high as aerosol. It has to be emphasized that aerosol layer height affects all the products afterwards because it is an input in radiative transfer model, however NO<sub>2</sub> only has impact on air mass factor which requires a NO<sub>2</sub> vertical profile for calculation and thus on vertical column density. The scenarios are listed in Table 5.2.

## LANDSAT IMAGE PROCESSING

Landsat Surface Reflectance product is available in the following scenes:

- Most Landsat 8 scenes acquired from April 11, 2013 to within one week of present acquisitions
- All Landsat 7 scenes acquired from 1999 to within one week of present acquisitions
- Most archived Landsat 4-5 Thematic Mapper (TM) scenes acquired from August 1982 to May 2012

During the project, Landsat 8 Operational Land Imager (OLI) and Thermal Infrared Sensor (TIRS) product is chosen because provides enhancement from prior Landsat instruments. Besides, Band 1 images are used in this case because the wavelength range in Band 1 is 0.43 - 0.45 micrometers which contains the wavelength for NO<sub>2</sub> observations.

The Landsat 8 data on 21 April over Berlin *LC81920242016112 - SC20160702155807* is downloaded from USGS Earth Resources Observation and Science (EROS) Center. The original projection system of the Landsat images are in WGS UTM 35N, the coordinate system needs to be transformed into WGS84 Geographic System with GDAL. Reprojected Band1 reflectance is visualized in Figure 5.20.

Reference region without source of pollution is selected by visual inspection. In the end, the same region used during DOAS fitting in Figure 5.21 is selected for scaling factor calculation.

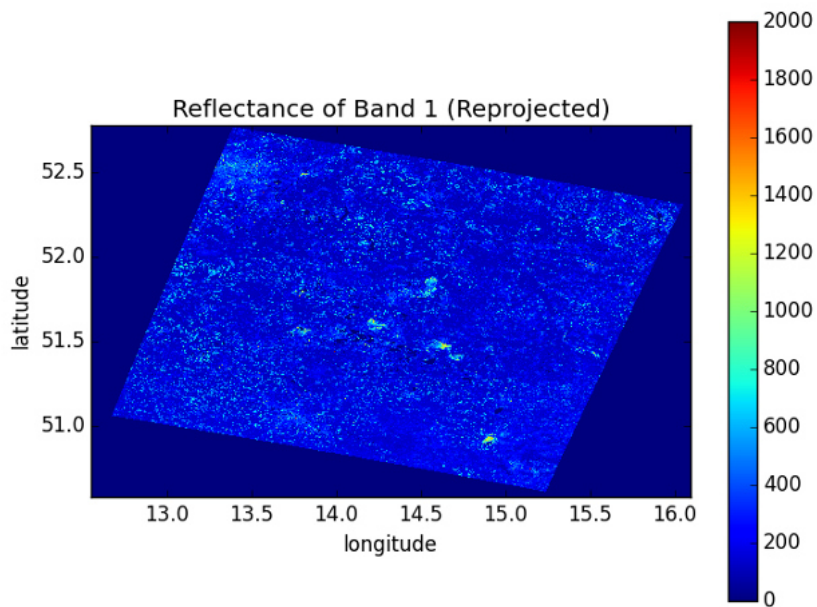


Figure 5.20: Landsat Band 1 Observation over Berlin on 21 April, 2016, scaling factor is 10000



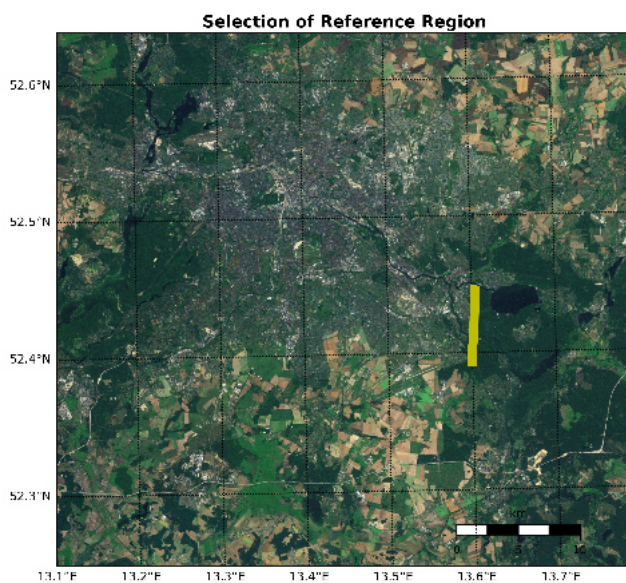


Figure 5.21: The region marked with blue is the reference area used for the calculation of scalar.



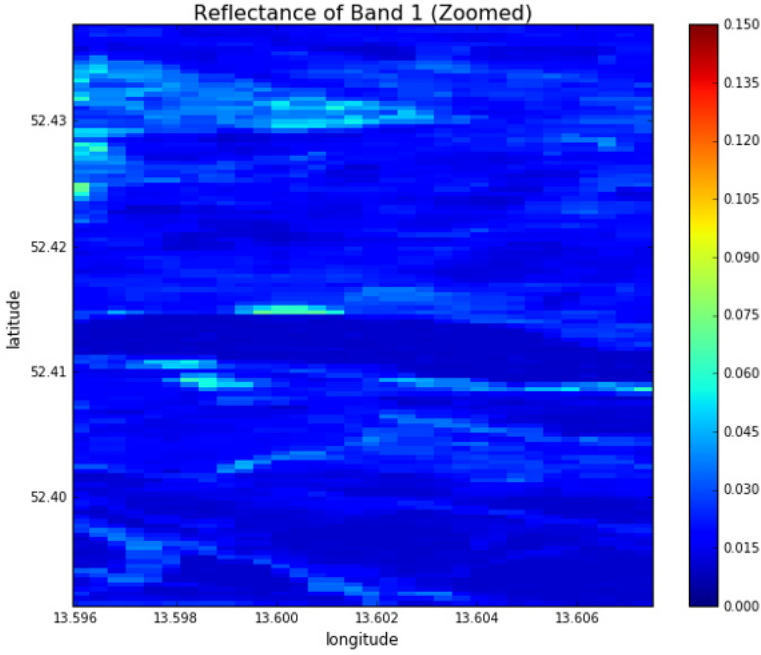


Figure 5.22: Zoomed Landsat Band 1 Observation over Berlin on 21 April, 2016.

Landsat data is then cropped to a smaller image around reference region for better processing efficiency as in Figure 5.22 and it is linearly interpolated to the surface reflectance on coordinates from Spectrolite measurements, which is shown in Figure 5.23

#### CALCULATION OF RADIANCE SCALING FACTOR

After Landsat 8 Band1 surface reflectance is calculated over the reference region, it is substituted into DAK LUT, thus modeled radiance can be derived through slicing and interpolation.

It has to be pointed out that in DAK model, the incident solar flux is always  $\pi W/m_2$  through a surface unit perpendicular to the incident solar beam. The radiances in the output are in  $W/m_2/sr$ . Usually these parameters are divided by  $\pi_0$ , which is the cosine of the solar zenith angle. This choice of  $\pi$  for the incident solar flux and division by  $\pi_0$  means that the real radiance should be calculated by Equation 5.10.

$$Radiance = \frac{Radiance_{DAK}}{\pi * \cos(\mu_0)} * Irradiance \quad (5.10)$$

,where  $Radiance_{DAK}$  is the scaled radiance from DAK modeling,  $Irradiance$  is solar irradiance and  $\mu_0$  is solar zenith angle.

Based on four scenarios of aerosol layer height, eight histograms of modeled radiance from DAK LUT and Landsat reflectance can be obtained. One example with 0.5 km aerosol layer in the morning is presented in Figure 5.24 in red, while the histogram of

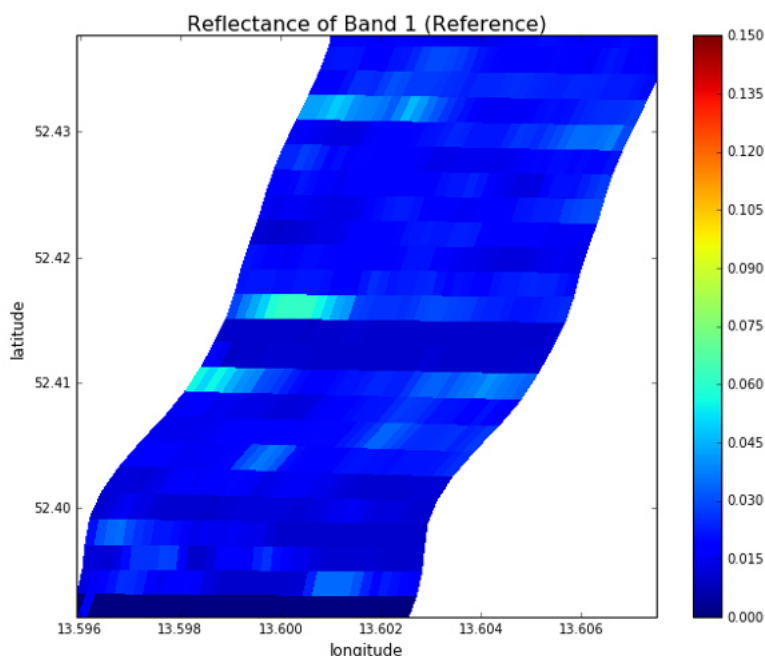


Figure 5.23: Landsat Band 1 Observation over Reference Area on 21 April, 2016.

Scenario	Aerosol Layer Height(km)	Scalar(AM)	Scalar(PM)
A	0.2	0.9765	0.9941
B	0.5	1.0071	1.0311
C	0.8	1.0388	1.0684
D	1.6	1.1242	1.1718

Table 5.3: Scaling factor for radiance in different aerosol layer height scenarios

measured radiance from Spectrolite is shown in blue in the same figure. The two histograms are both normalized in order to acquire the same magnitude, an obvious shift appears in Figure 5.24. It can be noticed that the shapes of the histograms are almost identical, except that DAK modeled radiance moves horizontally to the right of Spectrolite measurement. The medians of two dataset are retrieved to calculate the scaling factor. After applying the scaling factor, two histograms are updated in Figure 5.25, they are nearly overlapping with each other. It indicated that the scaling factor is accurate and effective. In total eight scalars are retrieved in different aerosol conditions in the morning and afternoon, they are presented in Table 5.3. By plotting the scalars as function of aerosol layer height in Figure 5.26, we can see that aerosol layer height almost has a linear impact on the scalars. In the afternoon, the scalar is overall higher than that in the morning and increases slightly faster along with the aerosol layer height.

Scaling factor is therefore applied to the whole radiance measurement. DAK LUT

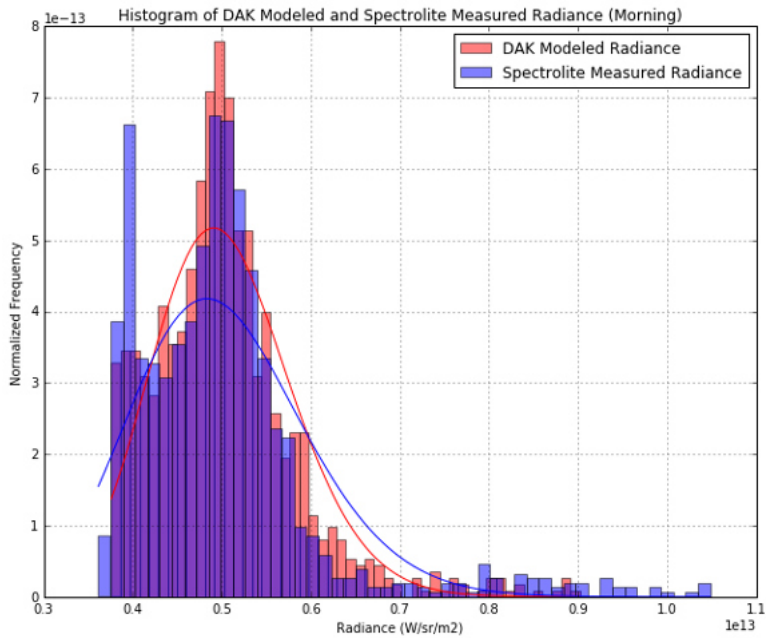


Figure 5.24: Normalized histograms of Spectrolite measured radiance and DAK modeled radiance with 0.5km aerosol layer height in the morning. The red histogram represents the modeled radiance from DAK with Landsat surface reflectance, while the blue one indicates the measured radiance from Spectrolite spectral observations.

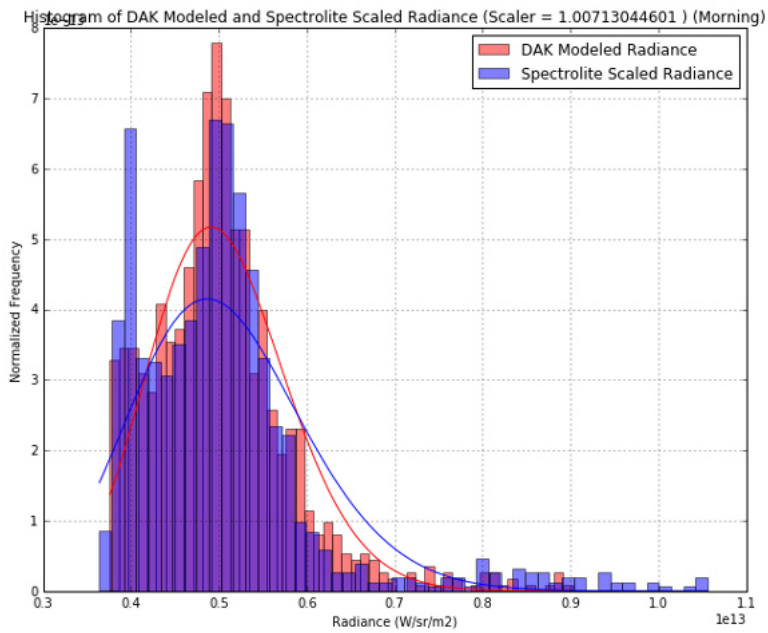


Figure 5.25: Normalized histograms of Spectrolite radiance after scaling and DAK modeled radiance with 0.5km aerosol layer height in the morning. The red histogram represents the modeled radiance from DAK with Landsat surface reflectance, while the blue one indicates the scaled radiance from Spectrolite spectral observations after applying the scalar.

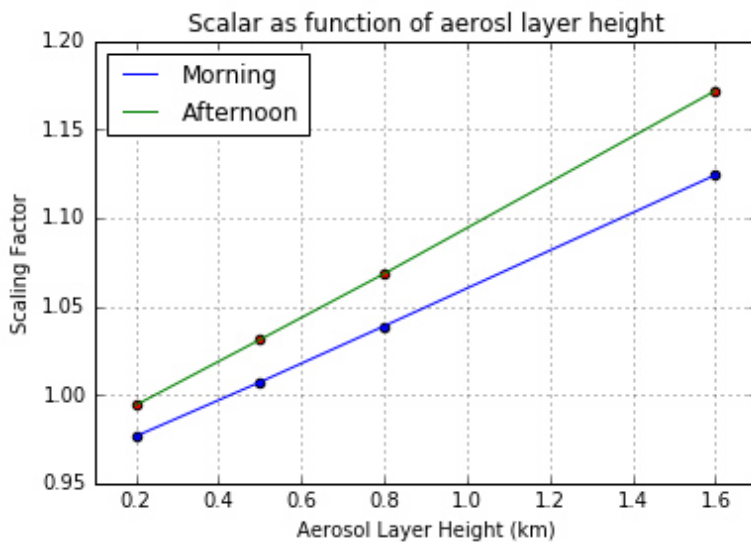


Figure 5.26: Scalars as function of aerosol layer height. Red line indicates the morning scenario while the blue one represents afternoon.

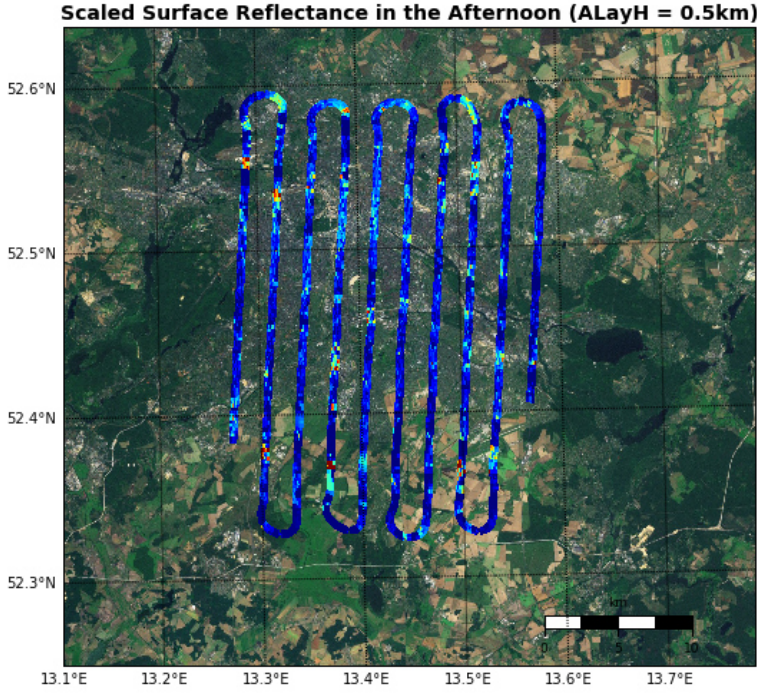


Figure 5.27: Scaled Surface Reflectance over Berlin in the Afternoon on 21 April, 2016

is sliced and interpolated again to obtain scaled surface reflectance. An example with 0.5km aerosol layer in the afternoon is visualized in Figure 5.27.

## CALCULATION OF AIR MASS FACTOR

Scaled surface reflectance is substituted into DAK model, both in the cases with and without  $\text{NO}_2$  perturbation in order to retrieve Box-AMF which is calculated by 5.11, where  $I_0$  and  $I$  are the radiance without and with  $\text{NO}_2$  perturbation respectively.  $\tau_{\text{NO}_2}$  is  $\text{NO}_2$  absorption optical thickness. From here in this report, due to the limited time of this project, only the major part of the measurements in the city are process. But the flight path of intentionally chosen data files goes through the city center as well as rural area.

$$\text{BAMF} = \ln\left(\frac{I_0}{I}\right) / \tau_{\text{NO}_2} \quad (5.11)$$

Finally, total AMF can be obtained as the the sum of the Box-AMF over the whole atmosphere weighted by the respective partial trace gas VCD, written in Equation 5.12. It is proves from the equation that it is the shape instead of the magnitude of  $\text{NO}_2$  profile that influence air mass factor because air mass factor can be considered as the weighted average of Box-AMF.  $\text{NO}_2$  profile is assumed to be rectangular with height half of or the same as aerosol layer. As a result, there will be 8 outputs in total corresponding to each scenario.

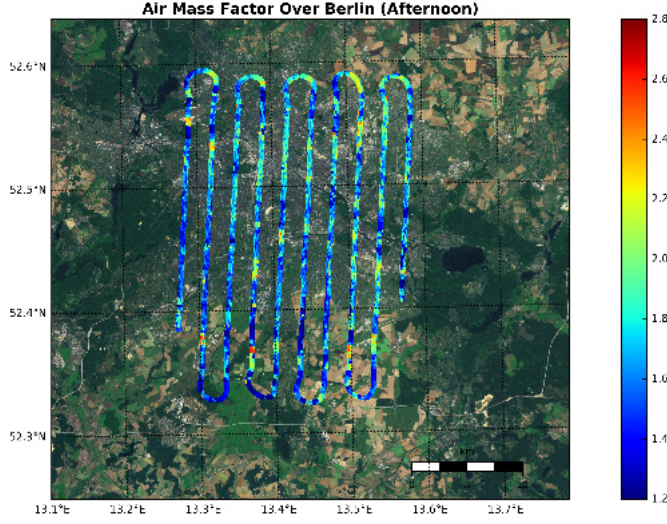


Figure 5.28: Air Mass Factor with 0.8km aerosol layer height and 0.4km NO<sub>2</sub> profile height over Berlin in the Afternoon on 21 April, 2016

$$AMF = \frac{\sum_0^{TOA} AMF \cdot VCD_i}{\sum_0^{TOA} VCD_i} \quad (5.12)$$

Consequently, there are eight results in total based on different aerosol layer heights and NO<sub>2</sub> profile height. Figure 5.28 visualizes the condition is 0.8 km aerosol layer height and 0.4 km profile height in the afternoon. Results of all occasions will be presented and interpreted in Chapter 6.

## STRATOSPHERIC CORRECTION

The radiance Spectrolite instrument measures goes through stratosphere and troposphere, then gets reflected to the sensor. Morning and afternoon measurements last for more than two hours, during which the impact of stratosphere has to be corrected because different solar zenith angle causes various light path, resulting in an error in obtained differential slant column density.

Stratospheric slant column density can be retrieved from OMI observation. It should be underlined that even though OMI data contains stratospheric slant column density, it is acquired in satellite observing conditions which are different from aircraft. So stratospheric vertical column density is taken instead. Level-3 OMI NO<sub>2</sub> Cloud-Screened Total and Tropospheric Column NO<sub>2</sub> data on 21 April is downloaded from GES DISC, Stratospheric VCD is interpolated to the pixel coordinates of Spectrolite measurement and it is plotted in Figure 5.29.



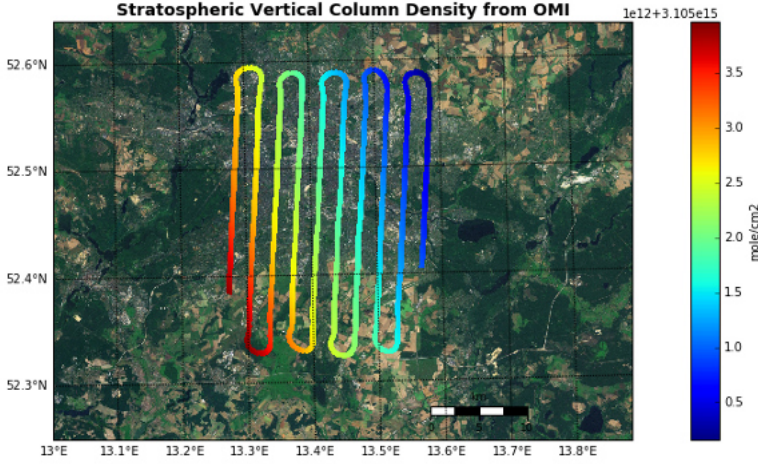


Figure 5.29: Stratospheric Vertical Column Density over Berlin in the Afternoon on 21 April, 2016

Stratospheric SCD is assumed to only be affected by geometry conditions. Geometric air mass factor  $AMF_{geo} = \frac{1}{\cos(\mu_0)}$  and stratospheric slant column density equals to stratospheric VCD multiply geometric air mass factor, as presented in Figure 5.30 and 5.29.

By looking at the stratospheric SCD in along-track direction in Figure 5.32, it is apparent that it increases along with pixel number (time). Because in the afternoon, the sun is setting. The light path through stratosphere is becoming longer, thus more radiance extincts due to scattering and absorption. As a result, calculated stratospheric SCD increases as well.

Stratospheric correction is made by subtracting the difference of stratospheric SCD between the first pixel and latter pixels from Differential SCD (Equation 5.13):

$$dSCD_{corrected} = dSCD - (SCD_{strat} - SCD_{strat}^1) \quad (5.13)$$

Figure 5.33 demonstrates the corrected differential slant column density with 0.5km aerosol layer height and 0.25km NO<sub>2</sub> profile height.

## RETRIEVAL OF TROPOSPHERIC VERTICAL COLUMN DENSITY

The total NO<sub>2</sub> slant column density can be divided into two parts, stratospheric SCD and tropospheric SCD, whereas the latter one is what we want to retrieve.

Thus, the total SCD over the city can be written as:

$$\begin{aligned} SCD &= SCD_{strat} + SCD_{tropo} \\ &= SCD_{strat} + VCD_{tropo} \cdot AMF \end{aligned}$$

where  $SCD_{strat}$  is the stratospheric slant column density,  $SCD_{tropo}$  is the tropospheric slant column density,  $VCD_{tropo}$  is the tropospheric vertical column density and

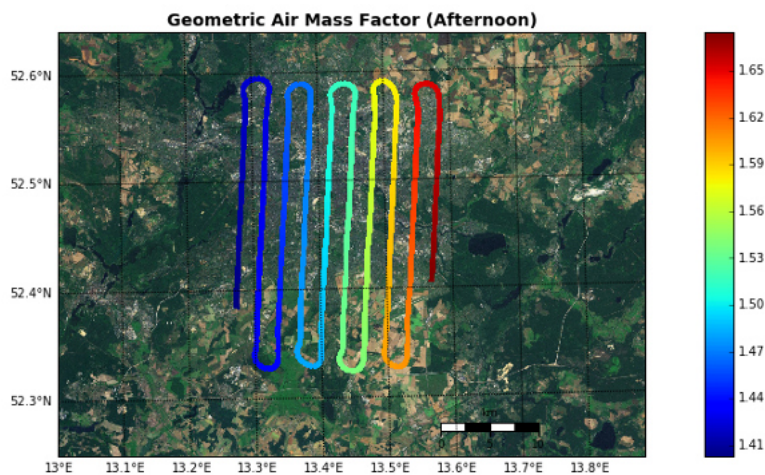


Figure 5.30: Geometric Air Mass Factor over Berlin in the Afternoon on 21 April, 2016

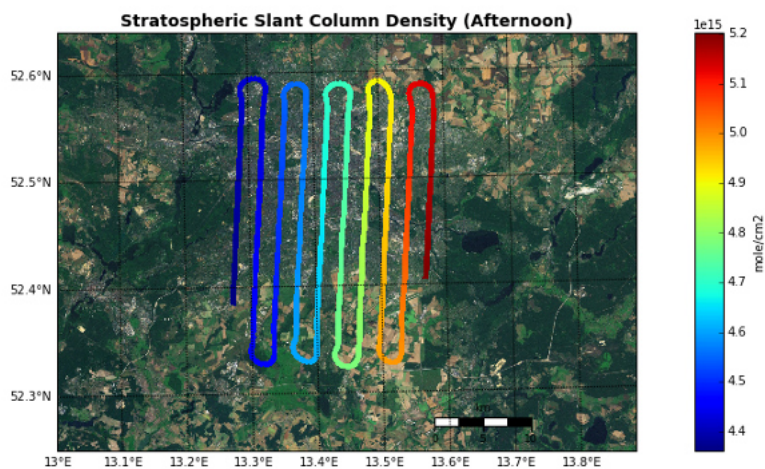


Figure 5.31: Stratospheric Slant Column Density over Berlin in the Afternoon on 21 April, 2016



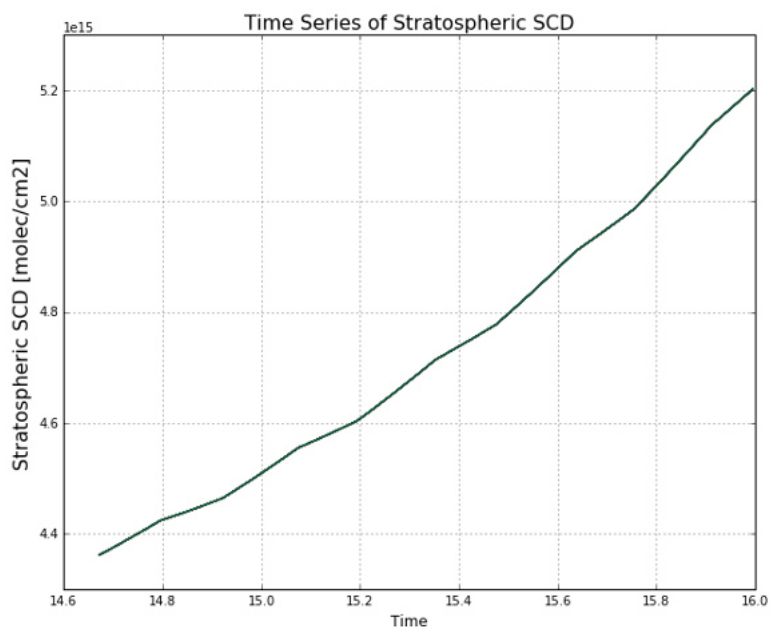


Figure 5.32: Stratospheric SCD Along-track over Berlin in the Afternoon on 21 April, 2016

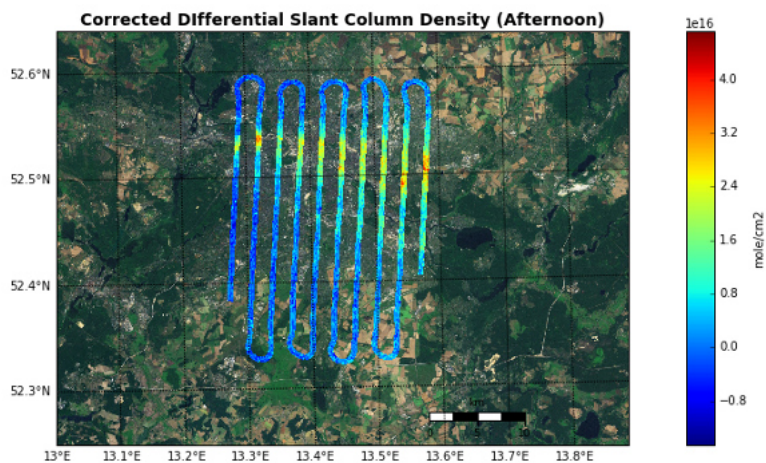


Figure 5.33: Corrected Differential Slant Column Density over Berlin in the Afternoon on 21 April, 2016

$AMF$  is the air mass factor during the Spectrolite observations obtained by DAK modeling. Then the SCD over the reference region is:

$$\begin{aligned} SCD_{ref} &= SCD_{strat,ref} + SCD_{tropo,ref} \\ &= SCD_{strat,ref} + VCD_{tropo,ref}^{OMI} \cdot AMF_{ref} \end{aligned}$$

Differential slant column density is the difference of SCD with respect to the reference region:

$$\Delta SCD = (SCD_{strat} + VCD_{tropo} \cdot AMF) - (SCD_{strat,ref} + VCD_{tropo,ref}^{OMI} \cdot AMF_{ref})$$

The absolute vertical column density is therefore calculated by:

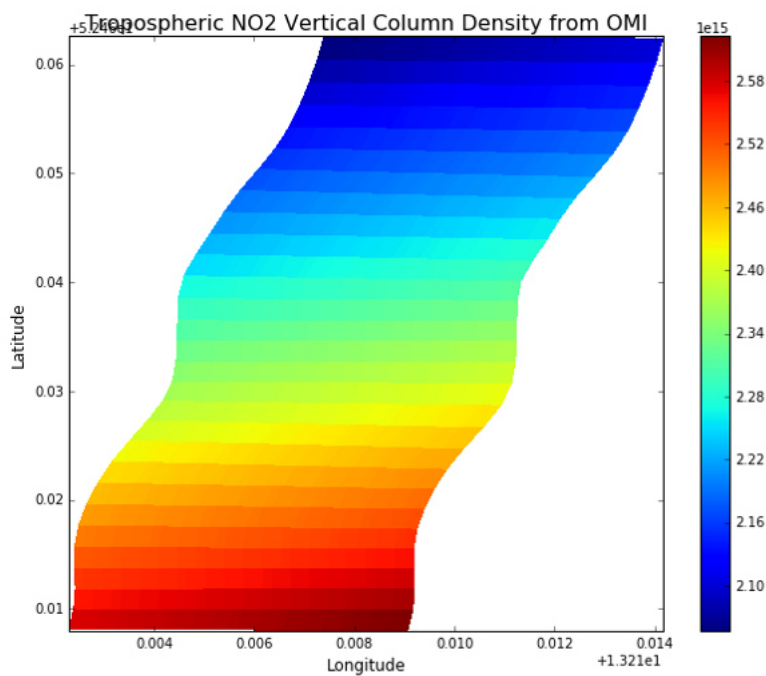
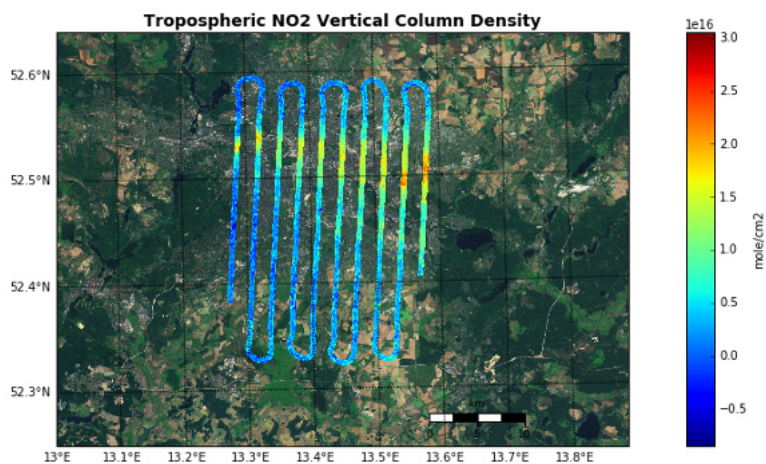
$$VCD_{tropo} = \frac{\Delta SCD + (SCD_{strat,ref} - SCD_{strat}) + VCD_{tropo,ref}^{OMI} \cdot AMF_{ref}}{AMF}$$

As is explained in Chapter 3, we consider the light detected by the instrument traverses the same path in the stratosphere, and the error caused by different solar zenith angles over time has also been corrected, the calculation of absolute tropospheric vertical column density therefore can be written as:

$$VCD_{tropo} = \frac{\Delta SCD + VCD_{tropo,ref}^{OMI} \cdot AMF_{ref}}{AMF}$$

OMI Level3 data is used again by interpolating Tropospheric VCD to Spectrolite measurement locations. It is shown in Figure 5.34. On the purpose of simplification, averaged VCD is take in along-track direction. Subsequently 37 VCDs in viewing direction are obtained and added to differential VCD. Therefore,  $NO_2$  vertical column density is retrieved, and it is the final product we want to acquire from Spectrolite measurement in this project. One example with aerosol layer height 0.5km and  $NO_2$  profile height 0.25km is presented in Figure 5.35.

In the end, all calculated variable, such as coordinates, AMF, dSCD, VCD, etc. are all stored in MAT file for future discussion and visualization.

Figure 5.34: Tropospheric NO<sub>2</sub> Vertical Column Density from OMIFigure 5.35: Tropospheric NO<sub>2</sub> Vertical Column Density from OMI



# 6

## RESULTS

**Sub Question 5:** What do the intermediate and final products indicate and how does the uncertainties in relevant geophysical parameters influence the results?

This chapter presents the intermediate products (dSCD, surface reflectance, air mass factor) and final result (NO<sub>2</sub> vertical column density) after radiative transfer modeling and data processing. They are interpreted with ground feature by visual inspection. In addition, the precision of the algorithm is studied by looking into the impact of uncertainties in the project - the heights of aerosol and NO<sub>2</sub> profiles which are considered rectangular shaped as well as surface reflectance. As is mentioned, aerosol layer height is assumed to be 0.2, 0.5 0.8 or 1.6 km, while NO<sub>2</sub> profile height is either half of or the same as that of aerosol. Therefore results obtained in these eight conditions are compared to see if the algorithm offers a reasonable processing chain for Spectrolite measurements. Expect for dSCD and VCD, we mainly focus on the other products in the afternoon due to considering the capacity of the project, results in the morning will be visualized in appendix.

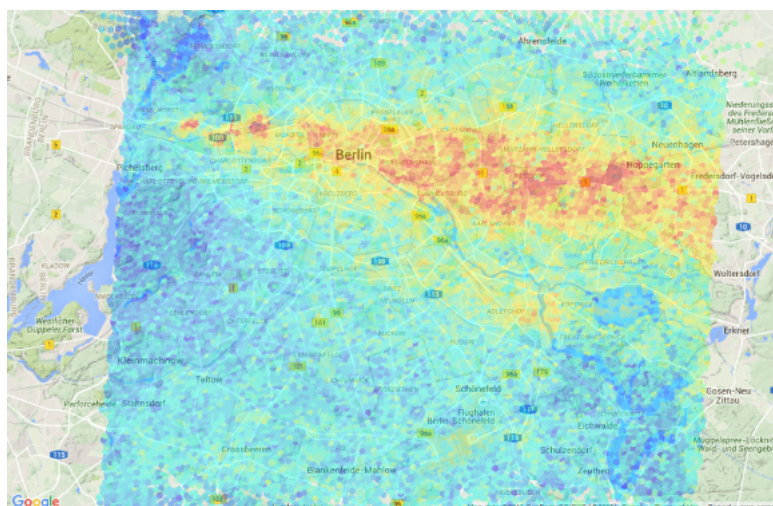


Figure 6.1: SWING measurement during the AROMAPEX in the afternoon on the same day over the city of Berlin. (Figure source: AROMAPEX SWING group)

## VISUALIZATION AND INTERPRETATION

### DIFFERENTIAL SLANT COLUMN DENSITY

Figure 5.18 and 5.19 show the differential slant column density (dSCD) in the morning and afternoon on 21 april 2016 over the city of Berlin and surrounding regions. Even though the DSCD does not correspond to the retrieved  $\text{NO}_2$  column in the troposphere, it still offers some information about the trend and movement of the trace gas. One of the most outstanding features of the map is the pollution plume over the city center, stretching from the west to the east. This feature was also observed with the other instruments (SWING) participating in the AROMAPEX campaign (Figure 6.1) and gives a first indication of successful operation of Spectrolite.

The basic statistics in the morning and afternoon are demonstrated in Table 6.1 and the histograms are shown in Figure 6.2. It can be seen that the minimum and maximum magnitude of dSCD both increase in the afternoon, however the afternoon measurements have smaller mean with larger standard deviation. It means that the distribution of dSCD in the afternoon shifts to a range with larger magnitude. But the majority of dSCD in the morning is concentrated on a slightly bigger value than that in the afternoon. With larger standard deviation and maximum,  $\text{NO}_2$  concentration has a higher level of fluctuation, which indicates that the emission from main pollution sources is getting more outstanding and extreme.

In the morning, the  $\text{NO}_2$  pollution forms a shape of plume and the higher concentration of  $\text{NO}_2$  occurs in the northwest while in the afternoon, the plume broadens,  $\text{NO}_2$  highly concentrated area is shifted to the northeast part of the region. In order to study the movement of  $\text{NO}_2$  emissions, fifty locations with highest dSCD is selected in the morning and afternoon in Figure 6.3 and 6.4. The largest  $\text{NO}_2$  dSCD emissions in the morning and afternoon occur at five and three areas, respectively. By looking into

Measurement	Max	Min	Median	Standard Deviation
Morning	$4.011 \cdot 10^{16}$	$-1.927 \cdot 10^{16}$	$6.588 \cdot 10^{15}$	$6.451 \cdot 10^{15}$
Afternoon	$4.796 \cdot 10^{16}$	$-1.450 \cdot 10^{16}$	$5.311 \cdot 10^{15}$	$7.873 \cdot 10^{15}$

Table 6.1: Minimum, maximum, median and standard deviation of differential slant column density in the morning and afternoon.

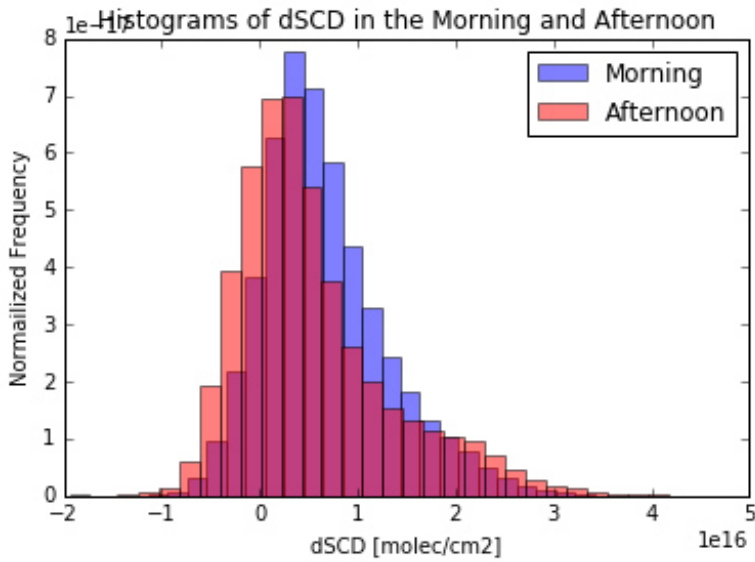


Figure 6.2: The histograms of differential slant column density in the morning and afternoon.



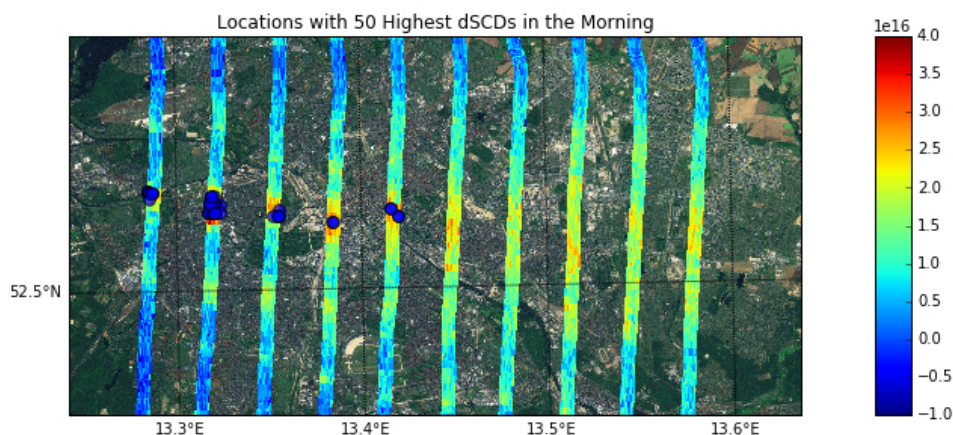


Figure 6.3: The histograms of differential slant column density in the morning and afternoon.

Google Maps, we can obtain the descriptions of these location in Table 6.2 and 6.3. It is clear that in the morning the main source of  $\text{NO}_2$  emission in Berlin is at (52.529N, 13.3165E) where a lot of industrial activities are going on as well as some commercial districts where pollution might be caused by heavy traffic. The interesting finding is that in the afternoon, even though the industrial regions still maintain high level of  $\text{NO}_2$ , suburbs such as (52.495N, 13.533E), (52.503N, 13.576E) also acquire high concentration. Given the expansion of the plume and the appearance of high concentration on suburbs, we can guess this situation might be caused by weather condition during the day. By looking into the wind record in Figure 6.5, it says that the wind direction in the morning on 21 April is towards east with increasing speed, which explains the shift of  $\text{NO}_2$  slant column density, and that  $\text{NO}_2$  pollution is blown away to the east by the wind and appears at locations without many human activities.

Beside this main feature, adjacent pixels are also looked into more detailedly for further confirmation. We can see it happens quite often that adjacent pixels in across track direction show considerably different  $\text{NO}_2$  dSCDs. This should not be caused by the true variability in the tropospheric  $\text{NO}_2$  column field. Especially over regions away from the city center where most of strong local  $\text{NO}_x$  sources are located, it can be expected that the true  $\text{NO}_2$  column between adjacent pixels differs only by a few percent. We can guess that the true variabilities are caused by instant  $\text{NO}_2$  emission from human activities.

For the peaks of dSCD in long-track direction that indicate the largest part the variabilities between adjacent pixels can be a consequence of not only relatively low signal to noise, i.e. imprecise DOAS fits, but also differences in surface reflectance between adjacent pixels. High surface reflectance brought by bright surfaces such as white painted buildings or concrete infrastructure cause enhanced sensitivity to  $\text{NO}_2$  close to the surface. However, on the contrary, the same magnitude of  $\text{NO}_2$  VCD will result in a lower dSCD over dark surfaces (e.g. forests and rural areas) because of reduced sensitivity.

It shows in Figure 6.6 the differential slant column density of three adjacent columns stretching out in the along track direction. and how these compare to the main features



Coordinates	Descriptions
(52.533N, 13.281E)	Kraftwerk Reuter West power plant, Industrial companies (Siemens, BSH), building materials store, furniture store, construction machine rental
(52.529N, 13.3165E)	Recycling center, car components malls, transit center and energy sector
(52.523N, 13.351E)	City core commercial area with shops, restaurants, gas station, courthouse and hospital
(52.522N, 13.380E)	City core political cultural center with government, embassies, galleries and museums
(52.522N, 13.413E)	City core commercial center Alexanderplatz

Table 6.2: Locations with higher NO<sub>2</sub> dSCDs in the morning. Blue dots indicate the highest NO<sub>2</sub> level and they are mainly distributed at (52.533N, 13.281E), (52.529N, 13.3165E), (52.523N, 13.351E), (52.522N, 13.380E), (52.522N, 13.413E).

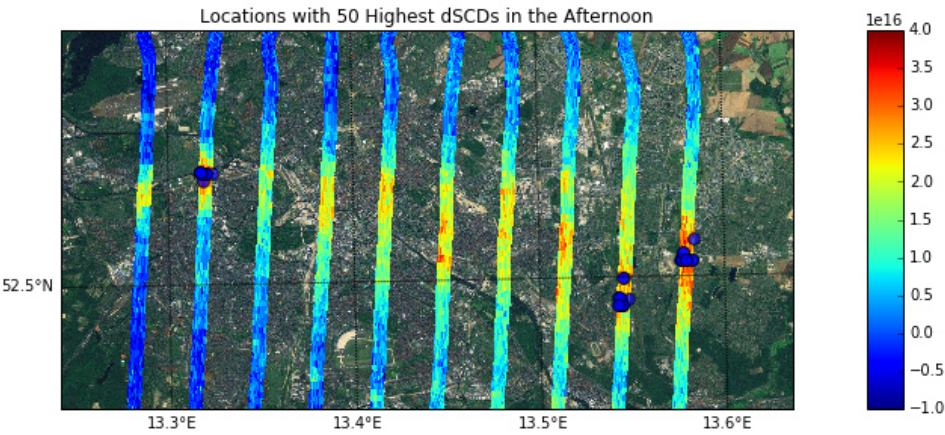


Figure 6.4: The histograms of differential slant column density in the morning and afternoon.

Coordinates	Descriptions
(52.529N, 13.3165E)	Recycling center, car components malls, transit center and energy sector
(52.495N, 13.533E)	Zoo, universities, cemetery
(52.503N, 13.576E)	Park, suburbs

Table 6.3: Locations with higher NO<sub>2</sub> dSCDs in the afternoon. Blue dots indicate the highest NO<sub>2</sub> level and they are mainly distributed at (52.529N, 13.3165E), (52.495N, 13.533E), (52.503N, 13.576E).









Time	Conditions			Comfort		
		Temp	Weather	Wind		Humidity
07:50		5 °C	Passing clouds.	9 km/h	→	81%
09:20		7 °C	Passing clouds.	9 km/h	→	71%
09:50		9 °C	Passing clouds.	13 km/h	→	66%
10:20		10 °C	Passing clouds.	20 km/h	→	62%
10:50		10 °C	Passing clouds.	19 km/h	→	58%
11:20		10 °C	Passing clouds.	20 km/h	→	54%
11:50		12 °C	Passing clouds.	19 km/h	↗	54%
12:50		11 °C	Passing clouds.	19 km/h	→	47%

Figure 6.5: Wind Direction in the Morning

that can be seen on the map (e.g. the pollution plume over the city center). The variability of  $\text{NO}_2$  dSCD in along-track direction is about  $3-5 \times 10^{16} \text{ molec/cm}^2$  and it is assumed to be caused by pollution. This is already sufficient to detect the plume, i.e. to quantify the contrast between pollution in the city center and rural regions at greater distance from the center.

Then, Spectrolite measurements are compared with SWING measurements conducted at the same time during the campaign. Swing data is interpolated on the same time stamps as Spectrolite. The time series of morning measurements is shown in Figure 6.7. The trends of the two time series are quite corresponding, while the difference of magnitude acquires a mean of  $-3.833 \cdot 10^{15} \text{ molec/cm}^2$  and a standard deviation of  $3.770 \cdot 10^{15} \text{ molec/cm}^2$ . To study the relationship of two instrument, scatter plots are made and it is found out that dSCD measurements from Spectrolite and SWING obeys a linear function. In the afternoon, as can be calculated in Figure 6.10 and 6.11, the difference of magnitude has a mean of  $-3.860 \cdot 10^{15} \text{ molec/cm}^2$  and a standard deviation of  $3.888 \cdot 10^{15} \text{ molec/cm}^2$ . The two measurements also indicate a linear relation.

### SCALED SURFACE REFLECTANCE

Surface reflectance here refers to the scaled surface reflectance retrieved by scaling measured radiance with modeled radiance from DAK LUT and it is the surface reflectance detected by the sensor. As is discussed before, there are four scaled surface reflectance outputs according to different aerosol layer heights (0.2km, 0.5km, 0.8km and 1.6km). An example with 0.5km has been given in Figure 5.27. The distribution is related to the brightness of surface features. Zoomed-in map (Figure 6.13) clearly indicated that white roofs of buildings and structures of bright concrete acquire larger surface reflectance while that of forest and darker architectures is relatively much smaller.

From the histograms in Figure 6.14, we can see that the number of larger magnitude

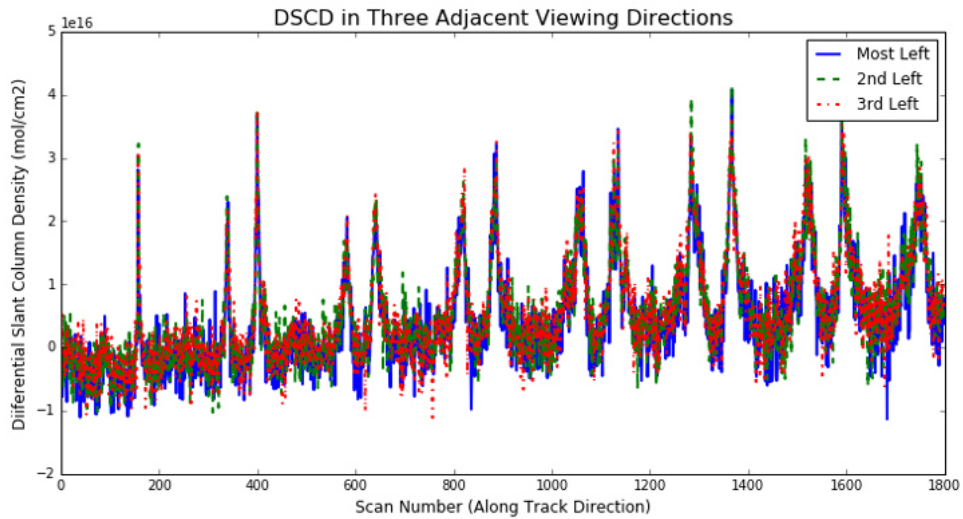


Figure 6.6: Differential Slant Column Density (Corrected) in the Afternoon

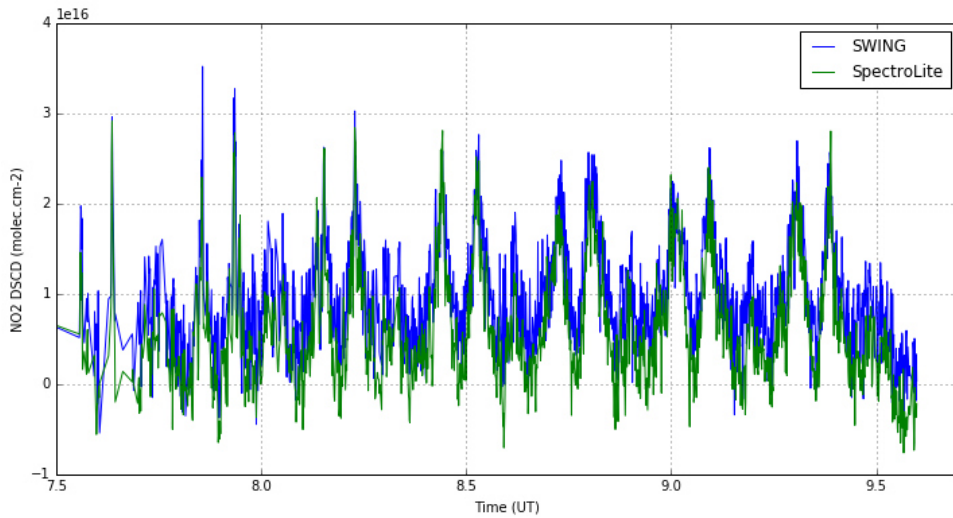


Figure 6.7: Time series of morning Spectrolite differential slant column density in comparison with SWING measurements.

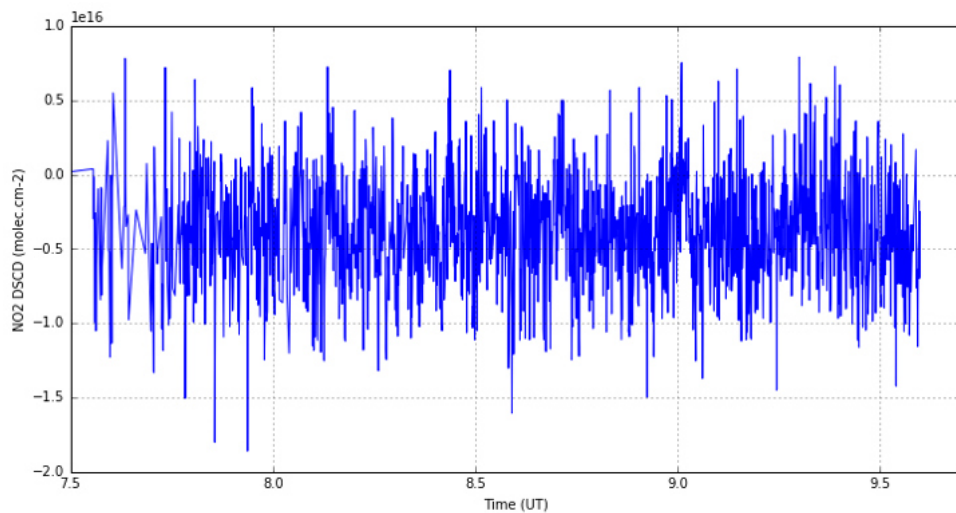


Figure 6.8: Time series of difference between differential slant column density measured by Spectrolite and SWING in the morning.

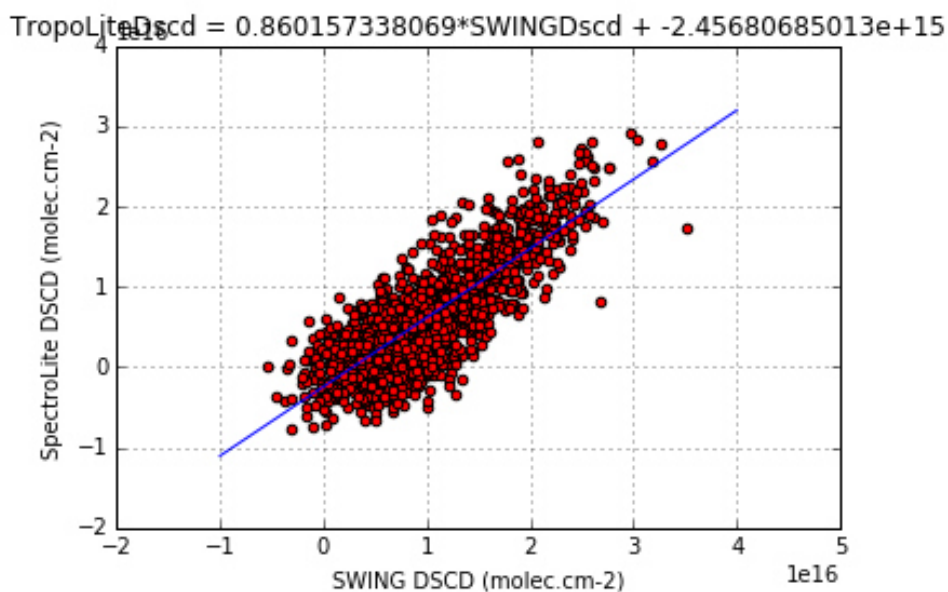


Figure 6.9: Scatter plot of difference between differential slant column density measured by Spectrolite and SWING in the morning.

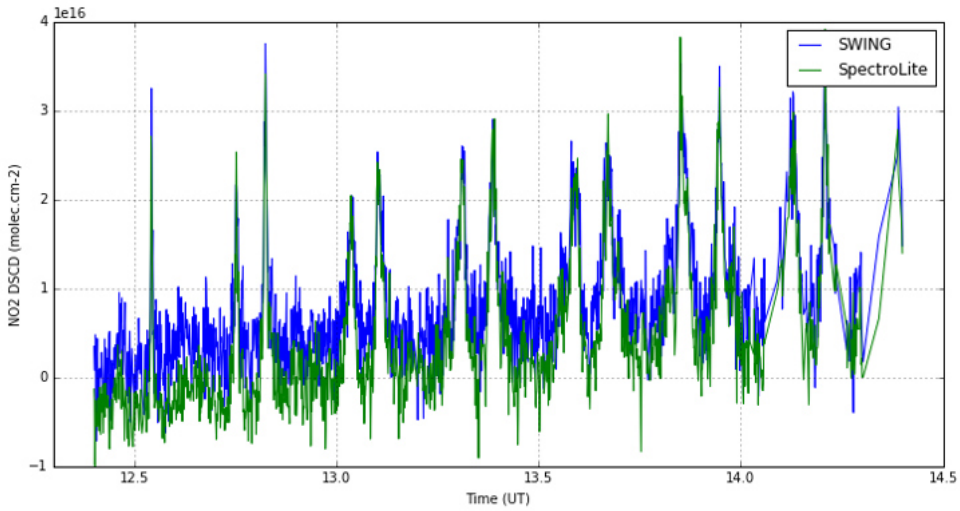


Figure 6.10: Time series of afternoon Spectrolite differential slant column density in comparison with SWING measurements.

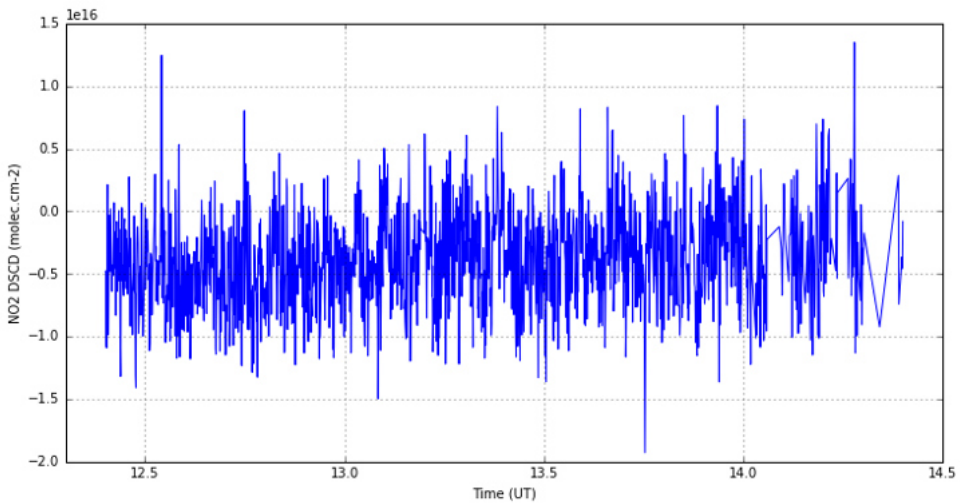


Figure 6.11: Time series of difference between differential slant column density measured by Spectrolite and SWING in the afternoon.

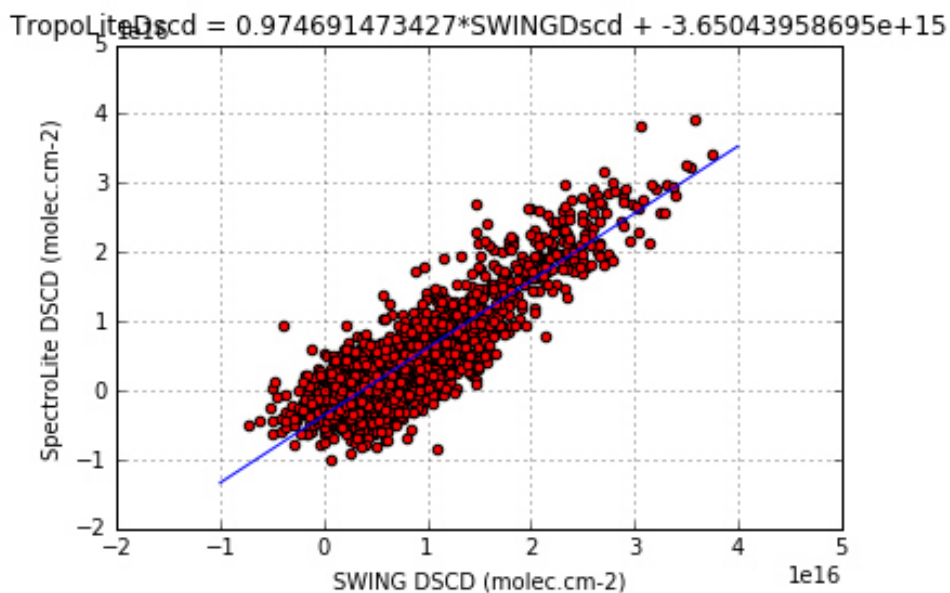


Figure 6.12: Scatter plot of difference between differential slant column density measured by Spectrolite and SWING in the afternoon.

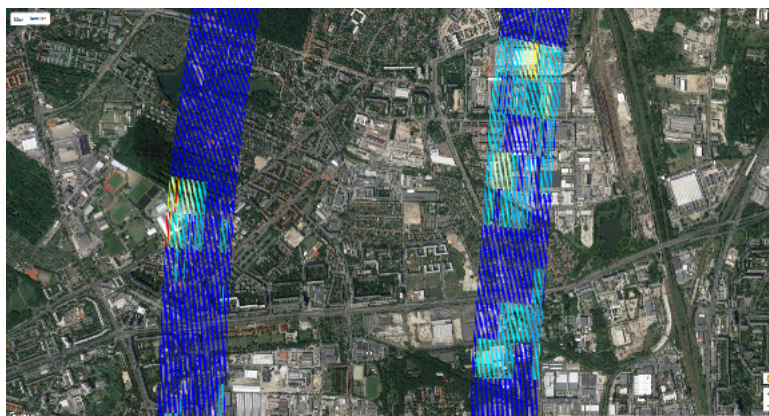


Figure 6.13: Zoomed-in Map of Scaled Surface Reflectance (Aerosol Layer Height is 0.2km) over Berlin in the Afternoon on 21 April, 2016



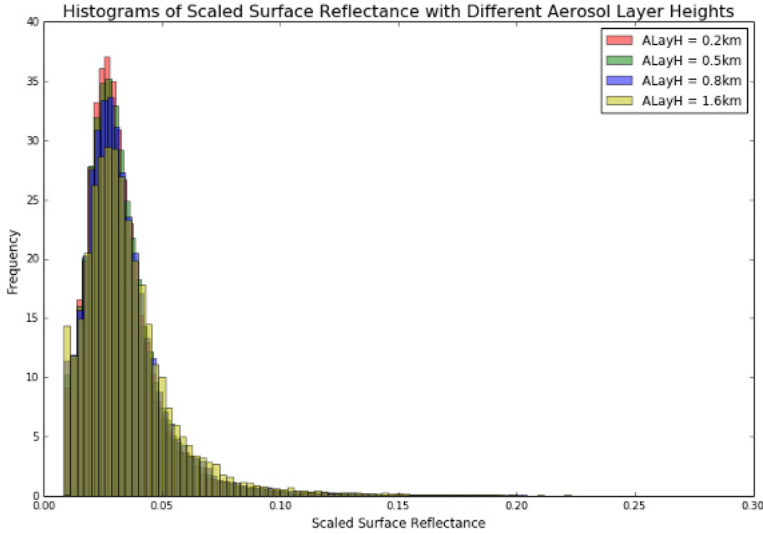


Figure 6.14: Histogram of scaled surface reflectance in the afternoon.

of surface reflectance (0.05 - 0.08) increases while the frequency of median surface reflectance decreases, which means the surface reflectance around median value becomes larger. It can be interpreted as in general the magnitude of scaled surface reflectance increases if aerosol layer height rises. It can be verified in Figure 6.15 which shows the scatter plot of surface reflectance and radiance. For the one radiance, when aerosol layer height is larger, the retrieved scaled reflectance also gets bigger, which means that for the same Spectrolite measurement dataset, the scaled surface reflectance will overall be bigger along with the increase of aerosol layer height. However, the difference is not really significant, which can also be seen from the linear fitting in Figure 6.15, as the slopes and intercepts are not considerably different.

### AIR MASS FACTOR

For air mass factor, the height of  $\text{NO}_2$  profile also needs to be taken into consideration, thus there will be 8 scenarios (A1 - D2 as shown in Table 5.2). Individually, Figure 6.16 is the zoomed-in map of air mass factor with 0.8km aerosol layer height and 0.4km  $\text{NO}_2$  profile height, we can see that the bright surface has relatively higher value than darker area because the surface reflectance results in higher sensitivity to  $\text{NO}_2$ .

By looking at the results of air mass factor with the same aerosol layer height, the impact of  $\text{NO}_2$  profile height can be obtained. For instance, Figure 6.18 and 6.19 indicate that the magnitude of AMF overall increases when  $\text{NO}_2$  profile height rises, because AMF is calculated from Box-AMF with Equation 3.15 and Box-AMF acquires the shape in 4.20. When  $\text{NO}_2$  perturbation occurs below aircraft altitude, Box-AMF increases, and AMF can be regarded as the weighted average of AMF along with altitude.

Similarly, we can look at the plots where  $\text{NO}_2$  profile height is the same to identify the influence of aerosol layer height, such as Figure 6.19 and 6.20 which both acquire  $\text{NO}_2$

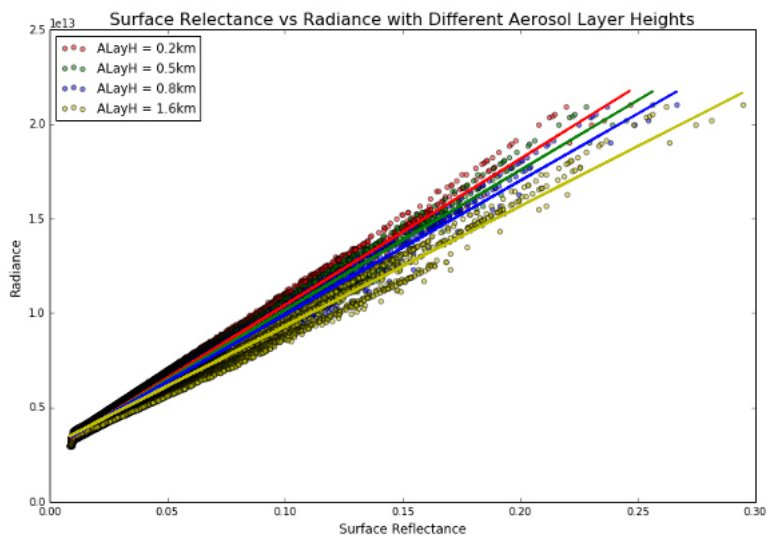


Figure 6.15: Scatter plot of scaled surface relectance and radiance in the afternoon.

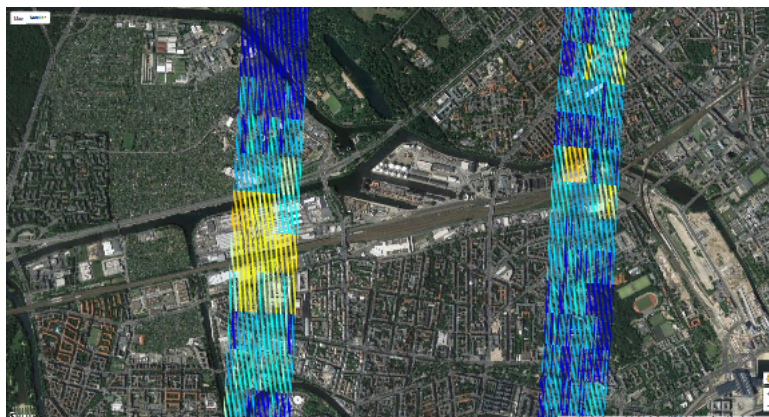


Figure 6.16: Zoomed-in Map of Air Mass Factor (Aerosol Layer Height is 0.8km, NO<sub>2</sub> Layer Height 0.4km) over Berlin in the Afternoon on 21 April, 2016



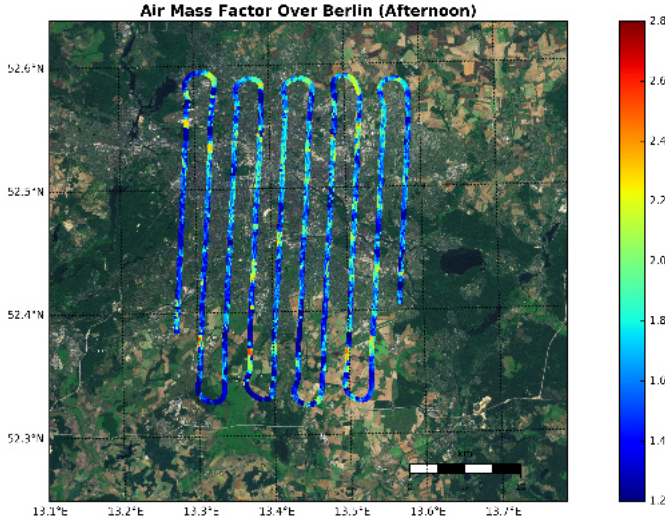


Figure 6.17: Air mass factor with 0.2km aerosol layer height and 0.2km NO<sub>2</sub> profile height in the afternoon.

profile height of 0.8km while their aerosol layer heights are 0.8km and 1.6km respectively. In this case AMF is decreasing, which tells that the increase of aerosol layer height decreases AMF. This is due to aerosol's impact on surface reflectance. Surface reflectance is reduced by aerosol and thus bring about lower sensitivity to NO<sub>2</sub>.

However, if we only look at the results where NO<sub>2</sub> profile height is half of (Figure 6.18 and 6.20) or equal to (Figure 6.17 and 6.19) aerosol layer height, The increases of both result in considerably bigger AMF. That is because now the influence for NO<sub>2</sub> profile is getting more dominating then aerosol, the increase finally outweighs the decrease.

Table 6.4 shows the basic statistics of air mass factor in different scenarios in the afternoon. By combining it with the histograms of air mass factor in Figure 6.21, we can come to the following conclusions. The increase of NO<sub>2</sub> layer height will cause an ascending in air mass factor and the ascending becomes more and more significant when the increase of NO<sub>2</sub> layer height becomes larger. The increase of aerosol layer height seems to result in the rise in AMF but this is because the positive impact of increased NO<sub>2</sub> outweighs the negative effect from aerosol layer. In addition, when aerosol layer gets thicker, the standard deviation of air mass factor is decreasing, which means that the distribution of AMF is narrowed down to a smaller range. The histograms of C2, D1 also show that the increase of aerosol layer will lead to decline in AMF. This is because aerosol decreases the surface reflectance, as in shown in the box-AMF vertical profile in Figure 4.25 in Chapter 4, the decrease of surface reflectance will cause a left shift in the profile below the aircraft, as AMF is the weighted sum of box-AMF along with altitude, the retrieved AMF will also decline.

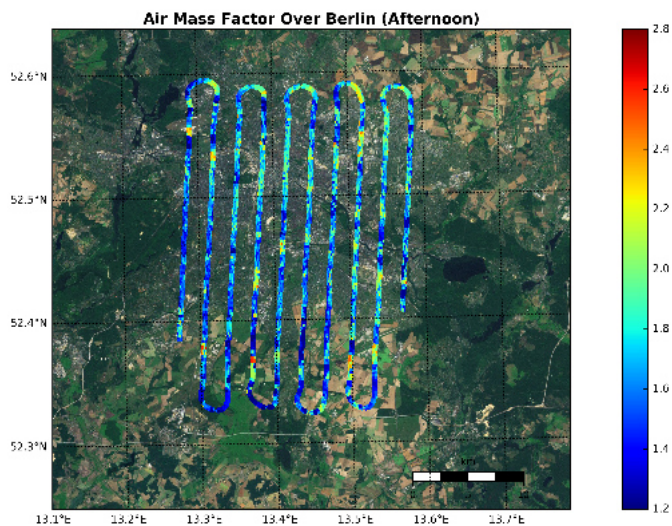


Figure 6.18: Air mass factor with 0.8km aerosol layer height and 0.4km NO<sub>2</sub> profile height in the afternoon.

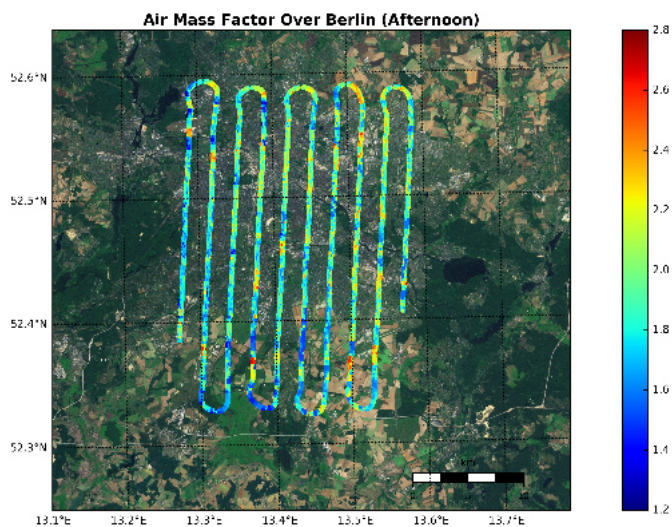


Figure 6.19: Air mass factor with 0.8km aerosol layer height and 0.8km NO<sub>2</sub> profile height in the afternoon.

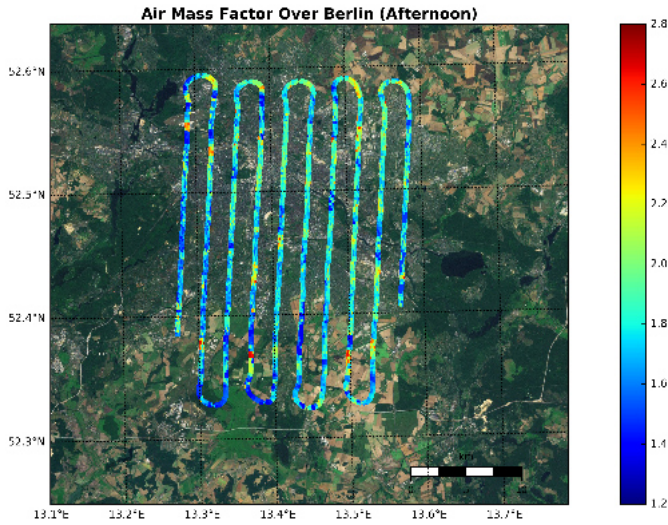


Figure 6.20: Air mass factor with 1.6km aerosol layer height and 0.8km NO<sub>2</sub> profile height in the afternoon.

Scenario	Max	Min	Median	Standard Deviation
A1	2.810	1.080	1.500	0.275
A2	2.819	1.178	1.562	0.264
B1	2.803	0.854	1.561	0.275
B2	2.834	1.079	1.721	0.245
C1	2.840	0.958	1.629	0.271
C2	2.882	1.295	1.863	0.226
D1	2.915	1.334	1.767	0.222
D2	2.976	1.813	2.150	0.161

Table 6.4: Minimum, maximum, median and standard deviation of air mass factor under different scenarios in the afternoon.

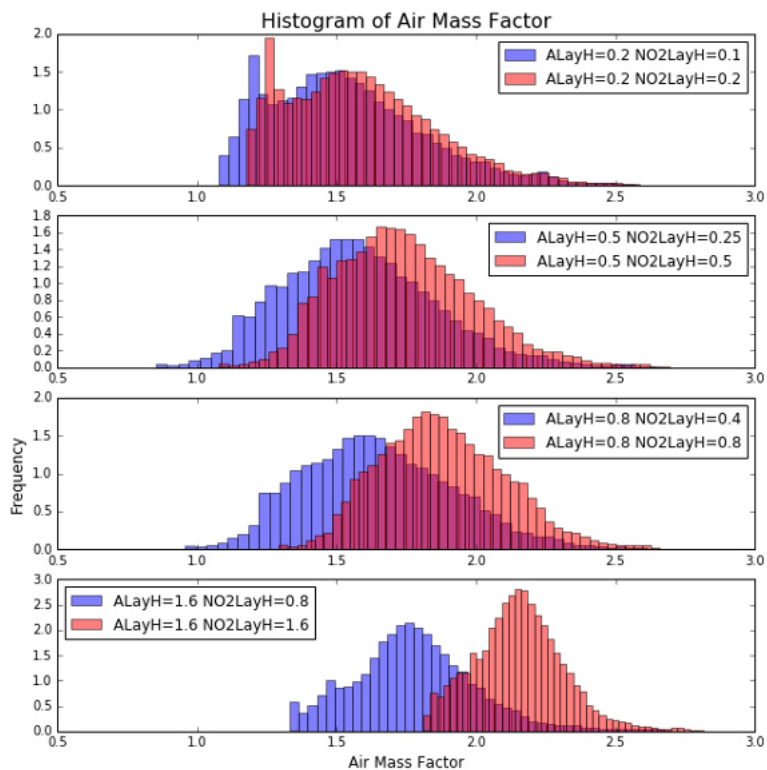


Figure 6.21: Histograms of Air Mass Factor over Berlin in the Afternoon on 21 April, 2016

Scenario	Max	Min	Median	Standard Deviation
A1	$3.049 \cdot 10^{16}$	$-8.836 \cdot 10^{15}$	$4.168 \cdot 10^{15}$	$4.816 \cdot 10^{15}$
A2	$2.897 \cdot 10^{16}$	$-8.331 \cdot 10^{15}$	$4.118 \cdot 10^{15}$	$4.633 \cdot 10^{15}$
B1	$2.946 \cdot 10^{16}$	$-8.814 \cdot 10^{15}$	$4.142 \cdot 10^{15}$	$4.651 \cdot 10^{15}$
B2	$2.613 \cdot 10^{16}$	$-6.829 \cdot 10^{15}$	$4.119 \cdot 10^{15}$	$4.213 \cdot 10^{15}$
C1	$2.836 \cdot 10^{16}$	$-8.132 \cdot 10^{15}$	$3.981 \cdot 10^{15}$	$4.449 \cdot 10^{15}$
C2	$2.380 \cdot 10^{16}$	$-5.994 \cdot 10^{15}$	$3.887 \cdot 10^{15}$	$3.912 \cdot 10^{15}$
D1	$2.540 \cdot 10^{16}$	$-6.637 \cdot 10^{15}$	$3.971 \cdot 10^{15}$	$4.152 \cdot 10^{15}$
D2	$2.019 \cdot 10^{16}$	$-4.575 \cdot 10^{15}$	$3.840 \cdot 10^{15}$	$3.446 \cdot 10^{15}$

Table 6.5: Minimum, maximum, median and standard deviation of vertical column density under different scenarios in the afternoon.

### VERTICAL COLUMN DENSITY

As is explained in the previous chapter, the vertical column density is retrieved by:

$$VCD_{tropo} = \frac{\Delta SCD + VCD_{tropo,ref}^{OMI} \cdot AMF_{ref}}{AMF}$$

Where  $\Delta SCD$  is differential slant column density after correction for stratosphere,  $VCD_{tropo,ref}^{OMI}$  is the  $NO_2$  tropospheric vertical column density derived from OMI measurement on the same day over the reference region,  $AMF_{ref}$  is the air mass factor over the reference region obtained by DAK modeling,  $AMF$  is the air mass factor during measurements. One can tell that  $AMF$  determines the final results of VCD, obtaining a negative influence, which illustrates that aerosol layer height and  $NO_2$  layer height will have the exact opposite impact as it has on  $AMF$ .

Table 6.5 shows the basic statistics of vertical column density retrieval in the afternoon. We can know that the impact of aerosol layer height and  $NO_2$  profile do not affect the median of VCD to a large extent, which is also indicated in the histogram in Figure 6.22. The biggest difference in the table is  $\frac{4.168 \cdot 10^{15} - 3.840 \cdot 10^{15}}{3.840 \cdot 10^{15}} = 8.54\%$ . First we can focus on each subplot, when  $NO_2$  profile height increases, the values around median is redistributed further away from the median, because larger  $NO_2$  profile height leads to bigger  $AMF$  which has a negative influence on VCD by division. The same reason also applies to the narrowing of the range of VCD distribution, the maximum value (positive) becomes smaller and minimum (negative) gets larger. But it has to be noted that, seemingly the increase of aerosol layer height also leads to the decrease of VCD as the histograms are shifting slightly to the left, but it is in fact caused by the increase of  $NO_2$  profile height.

Two zoomed-in VCD maps are offered in Figure 6.23 and 6.24 to have a clearer visualization of influences from aerosol and  $NO_2$  profile on the detection of pollution sources. Figure 6.23 shows the location with highest  $NO_2$  VCD under Scenario A1 while Figure 6.24 represent Scenario D2. We can see that when it comes to an extreme case (two heights are not well estimated), it will affect the outcome of sources detection, which in this case it shows that scenario D2 leads to a quite spread out distribution estimation of  $NO_2$  emission sources, some of which might not be the biggest emitters.



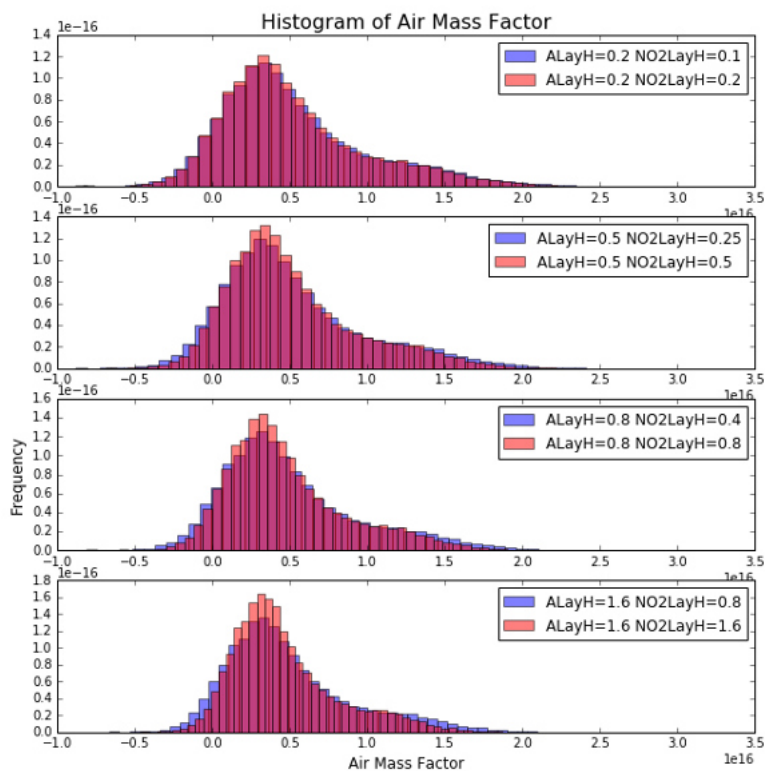


Figure 6.22: Histograms of Differential Vertical Column Density over Berlin in the Afternoon on 21 April, 2016

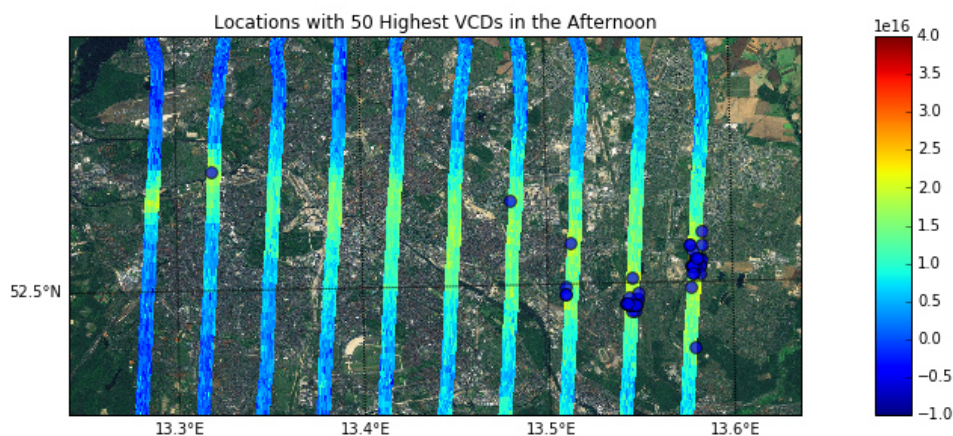


Figure 6.23: Locations of 50 highest NO<sub>2</sub> VCD with 0.2km aerosol layer height and 0.1km NO<sub>2</sub> profile height over Berlin in the afternoon on 21 April, 2016

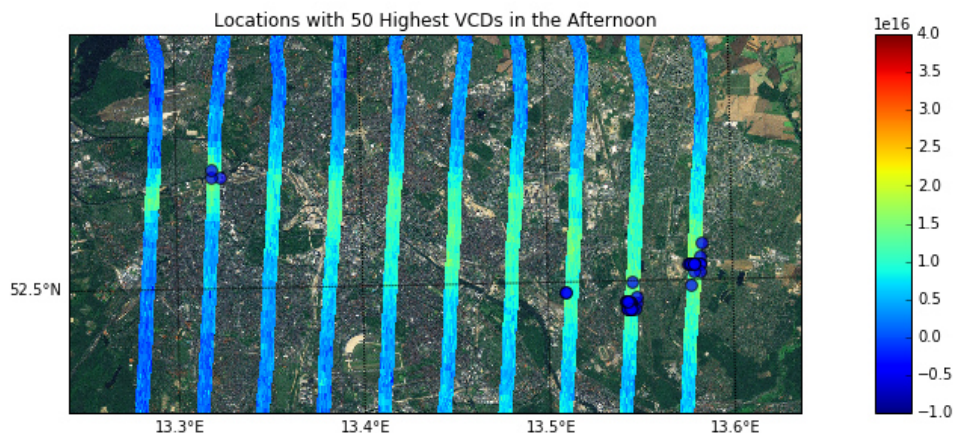


Figure 6.24: Locations of 50 highest NO<sub>2</sub> VCD with 1.6km aerosol layer height and 1.6km NO<sub>2</sub> profile height over Berlin in the afternoon on 21 April, 2016

## UNCERTAINTY STUDY

The error in the retrieval tropospheric NO<sub>2</sub> vertical column density of the Spectrolite measurement comes from both the differential slant column density and air mass factor calculation. However, the uncertainty from AMF computation is difficult to quantify precisely, because each parameter will have an impact on the over error budget in a forward model and as is discussed previously, we do not have accurate knowledge about some of the parameters. An approximation of uncertainty can be obtained by perturbation analysis.

Perturbation analysis is performed by perturbing each parameter with an estimated error by assuming these independent error do not have impact on each other inside the forward model. Therefore, a perturbation can also be observed in the retrieved air mass factor and vertical column density which will be compared with the original ones. This can offer an approximation of the relative significance of each parameter.

From what have been discussed previously, NO<sub>2</sub> profile height in the boundary layer and aerosol layer height are the most unknown parameters in this study, we do not have any data resource to retrieve an estimation. Besides, Air mass factor calculation requires a assumed NO<sub>2</sub> profile and simulated box-AMF vertical profile to determine the vertical sensitivity so it has direct influence, which makes it even more important. NO<sub>2</sub> profile is unknown and we assume the shape is rectangular and height is the only variable that determined NO<sub>2</sub> profile. Therefore, the main parameters that we want to investigate in the uncertain study of the project are NO<sub>2</sub> profile height in the boundary layer and aerosol layer height which are simulated in 8 scenarios in this project (Table 6.6).

By comparing A, B, C, D we can obtain the perturbation of AMF and VCD caused by NO<sub>2</sub> profile height, however, due to NO<sub>2</sub> profile height is determined by scale, C2/D1 can be used to look into the impact of aerosol layer height on the perturbation. A along track in the middle of the viewing direction is taken for analysis.

Figure 6.25 looks into the impact of increases of NO<sub>2</sub> profile height on AMF, and Fig-

Scenario	Aerosol Layer Height(km)	NO <sub>2</sub> Profile Height(km)
A1	0.2	0.1
A2	0.2	0.2
B1	0.5	0.25
B2	0.5	0.5
C1	0.8	0.4
C2	0.8	0.8
D1	1.6	0.8
D2	1.6	1.6

Table 6.6: Scenarios with different aerosol layer height and NO<sub>2</sub> profile height assumptions.

ure 6.26 shows the impact on VCD when aerosol layer stays then same, namely A1/2, B1/2, C1/2, D1/2 are separately compared. As can be seen from the two plots, the fluctuation gets more significant if the aerosol layer height becomes larger, when of NO<sub>2</sub> profile height also increase to bigger extent. More details are demonstrated in Table 6.7. When the uncertainty of NO<sub>2</sub> profile height rises 100%, the mean uncertainty in AMF increases from 0.0580(3.79%) to 0.3729(20.09%). In the case of VCD, the mean uncertainty changes from  $-8.86 \cdot 10^{13}(-1.70\%)$  to  $-2.97 \cdot 10^{15}(-6.08\%)$ . One noticeable change caused by the NO<sub>2</sub> is the minimum uncertainty in vertical column density which dramatically drops from  $-20.19\%$  to  $-79.18\%$ .



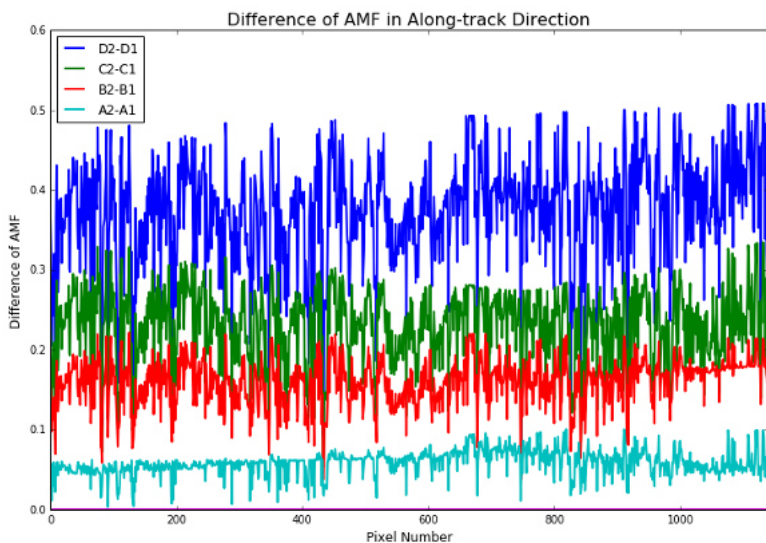


Figure 6.25: Difference of AMF in Along-track Direction with the same aerosol layer height but different  $\text{NO}_2$  profile height over Berlin in the afternoon on 21 April, 2016

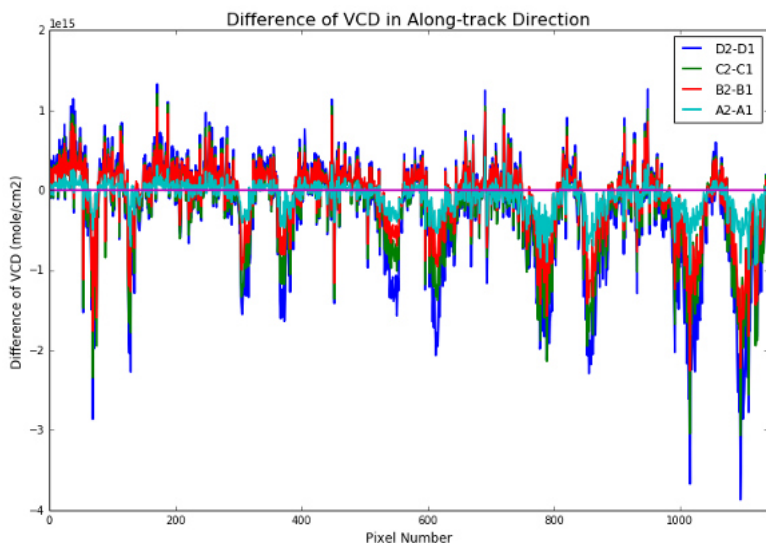


Figure 6.26: Difference of VCD in Along-track Direction with the same aerosol layer height but different  $\text{NO}_2$  profile height over Berlin in the afternoon on 21 April, 2016

$H^{aero}$	$H^{NO_2}$	$\delta H^{NO_2}$	$\delta AMF^{NO_2}_{min}$	$\delta AMF^{NO_2}_{max}$	$\delta AMF^{NO_2}_{mean}$	$\delta AMF^{NO_2}_{std}$
0.2	0.1	+0.1(+100%)	0.0031(+0.20%)	0.1003(+6.55%)	0.0580(+3.79%)	0.0151(+0.98%)
0.5	0.25	+0.25(+100%)	0.0375(+2.38%)	0.2214(+14.01%)	0.1592(+10.07%)	0.0290(+1.84%)
0.8	0.4	+0.4(+100%)	0.0462(+2.80%)	0.3343(+20.27%)	0.2291(+13.89%)	0.0466(+2.82%)
1.6	0.8	+0.8(+100%)	0.0635(+3.57%)	0.5082(+28.56%)	0.3729(+20.96%)	0.0678(+3.81%)

$H^{aero}$	$H^{NO_2}$	$\delta H^{NO_2}$	$\delta VCD^{NO_2}_{min}$	$\delta VCD^{NO_2}_{max}$	$\delta VCD^{NO_2}_{mean}$	$\delta VCD^{NO_2}_{std}$
0.2	0.1	+0.1(+100%)	$-1.05 \cdot 10^{15}$ (-20.19%)	$4.18 \cdot 10^{14}$ (+8.03%)	$-8.86 \cdot 10^{13}$ (-1.70%)	$1.94 \cdot 10^{14}$ (+3.72%)
0.5	0.25	+0.25(+100%)	$-2.25 \cdot 10^{15}$ (-43.87%)	$1.04 \cdot 10^{15}$ (+20.23%)	$-1.15 \cdot 10^{14}$ (-2.23%)	$4.47 \cdot 10^{14}$ (+8.69%)
0.8	0.4	+0.4(+100%)	$-3.06 \cdot 10^{15}$ (-62.15%)	$1.21 \cdot 10^{15}$ (+24.45%)	$-2.03 \cdot 10^{14}$ (-4.11%)	$5.59 \cdot 10^{15}$ (+11.32%)
1.6	0.8	+0.8(+100%)	$-3.87 \cdot 10^{15}$ (-79.18%)	$1.33 \cdot 10^{15}$ (+27.15%)	$-2.97 \cdot 10^{15}$ (-6.08%)	$7.25 \cdot 10^{15}$ (+14.84%)

Table 6.7: Perturbation study results of maximum uncertainties ( $\delta AMF^{NO_2}_{min}$ ,  $\delta VCD^{NO_2}_{min}$ , maximum uncertainties ( $\delta AMF^{NO_2}_{max}$ ,  $\delta VCD^{NO_2}_{max}$ ), mean uncertainties ( $\delta AMF^{NO_2}_{mean}$ ,  $\delta VCD^{NO_2}_{mean}$ ) and standards deviations ( $\delta AMF^{NO_2}_{std}$ ,  $\delta VCD^{NO_2}_{std}$ ) for the four aerosol layer height scenarios with different  $no_2$  perturbation in the afternoon on 21 April, 2016.

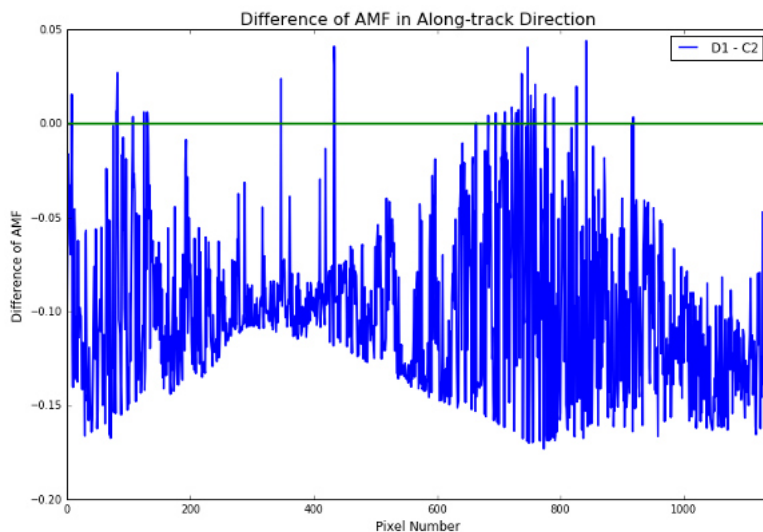


Figure 6.27: Difference of AMF in Along-track Direction with the same  $\text{NO}_2$  profile height but different aerosol layer heights over Berlin in the afternoon on 21 April, 2016

Subsequently, perturbation of AMF and VCD caused by  $\text{NO}_2$  are investigated by comparing C2/D1 which acquire different aerosol layer height but the same  $\text{NO}_2$  profile (Figure 6.28 and 6.28). In detail, Table 6.8 can tell that in general aerosol has a negative impact on AMF (positive impact on VCD) since the mean uncertainty is  $-0.01004$  ( $-5.34\%$ ), but the influence is not that important because the impact is quite limited in scale. So we can come to a conclusion that aerosol layer height has a minor effect than  $\text{NO}_2$  profile height, which also explains the domination of  $\text{NO}_2$  over aerosol in the change of AMF in the previous section.

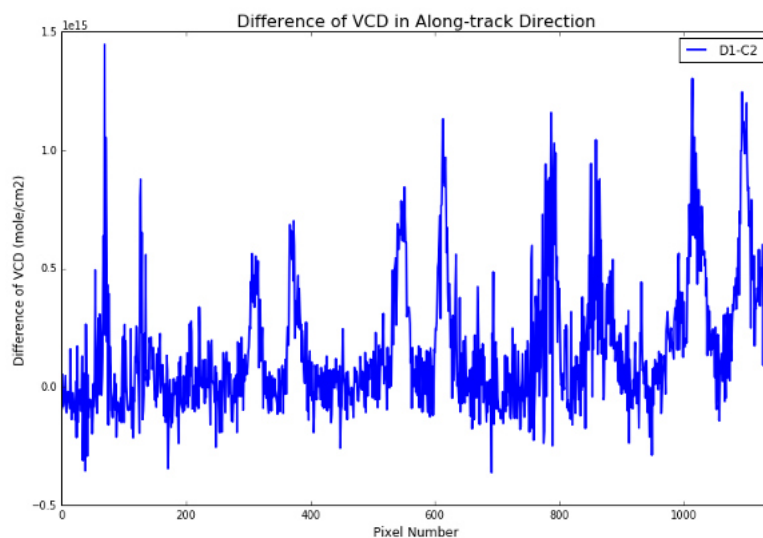


Figure 6.28: Difference of VCD in Along-track Direction with the same NO<sub>2</sub> profile height but different aerosol layer heights over Berlin in the afternoon on 21 April, 2016

$H^{\text{NO}_2}$	$H^{\text{aero}}$	$\delta H^{\text{aero}}$	$\delta \text{AMF}^{\text{aero}}_{\text{min}}$	$\delta \text{AMF}^{\text{aero}}_{\text{max}}$	$\delta \text{AMF}^{\text{aero}}_{\text{mean}}$	$\delta \text{AMF}^{\text{aero}}_{\text{std}}$
0.8	0.8	+0.8(+100%)	-0.1731(-9.21%)	0.0440(+2.34%)	-0.1004(-5.34%)	0.0412(+2.19%)
$H^{\text{NO}_2}$	$H^{\text{aero}}$	$\delta H^{\text{aero}}$	$\delta \text{VCD}^{\text{aero}}_{\text{min}}$	$\delta \text{VCD}^{\text{aero}}_{\text{max}}$	$\delta \text{VCD}^{\text{aero}}_{\text{mean}}$	$\delta \text{VCD}^{\text{aero}}_{\text{std}}$
0.8	0.8	+0.8(+100%)	$-3.63 \cdot 10^{14}$ (-7.66%)	$1.45 \cdot 10^{15}$ (+30.51%)	$1.53 \cdot 10^{14}$ (+3.22%)	$2.73 \cdot 10^{14}$ (+5.77%)

Table 6.8: Perturbation study results of maximum uncertainties ( $\delta \text{AMF}^{\text{aero}}$ ,  $\delta \text{VCD}^{\text{aero}}$ ), maximum uncertainties ( $\delta \text{AMF}^{\text{aero}}_{\text{max}}$ ,  $\delta \text{VCD}^{\text{aero}}_{\text{max}}$ ), mean uncertainties ( $\delta \text{AMF}^{\text{aero}}_{\text{mean}}$ ,  $\delta \text{VCD}^{\text{aero}}_{\text{mean}}$ ) and standards deviations ( $\delta \text{AMF}^{\text{aero}}_{\text{std}}$ ,  $\delta \text{VCD}^{\text{aero}}_{\text{std}}$ ) for one  $\text{NO}_2$  profile height scenarios with aerosol layer height perturbations in the afternoon on 21 April, 2016.



# 7

## CONCLUSION AND OUTLOOK

**Sub Question 6:** What conclusions could be made from the project? What improvements could help to obtain better results?

### CONCLUSION

The DOAS analysis revealed a median dSCD of  $4.011 \cdot 10^{15} \text{ molec/cm}^2$  and  $4.796 \cdot 10^{15} \text{ molec/cm}^2$  for the morning and afternoon overflights.  $\text{NO}_2$  dSCD obtained from Spectrolite measurements show a reasonable correspondence with those retrieved from AirMap and SWING measurements.

The results of  $\text{NO}_2$  vertical column density retrieval demonstrate very convincing spatial distribution of  $\text{NO}_2$  VCD over the city of Berlin. By projecting the data onto a satellite map, we can identify the pollution hot spots which contain much higher level of  $\text{NO}_2$  concentrations. The most significant finding is that the largest hot spot (52.53N, 13.24E) is exactly the location of the power plant Kraftwerk Reuter West which is the largest power plant owned by Vattenfall AB in Berlin and acquire approximate 5 times higher concentration than the those over the urban area of Berlin. The emission from the city mainly originates from industrial facilities such as recycling center, car components malls, transit center and energy sector around (52.52N, 13.31E) as well as commercial centers where shopping streets (52.52N, 13.45E) and arenas (52.51N, 13.45E) are located. In addition, lowest  $\text{NO}_2$  VCD is found in remote region from the city center, for example forest and farmland in the greater Berlin area. Therefore, we can come to a conclusion that Spectrolite is clearly sufficient to detect  $\text{NO}_2$  pollution sources.

Several differences can be noticed in the  $\text{NO}_2$  VCD and dSCD maps from the morning and afternoon measurements. First of all, the morning measurements demonstrate higher  $\text{NO}_2$  vertical column densities than the afternoon overflights, probably indicating the diurnal cycle of atmospheric  $\text{NO}_2$  as more  $\text{NO}_2$  is produced from pollution during the day, but since  $\text{NO}_2$  has a short lifetime, the level will decrease at night when there is much less human activities, and then the cycle repeats the next day. Besides, in the afternoon, the distribution of  $\text{NO}_2$  still keeps the plume shape, and the hot spots in morning

still remain high level of  $\text{NO}_2$  concentration while some appear above rural area. It illustrates that the wind direction is to the east and remains quite stable during the day.

The results obtained in this project indicate that the Spectrolite instrument can offer a general idea about the  $\text{NO}_2$  pollution distribution and pollution level over the urban region. However, in order to retrieve more precise  $\text{NO}_2$  absolute vertical column density, some improvements (such as detailed information of  $\text{NO}_2$  profile height and the surface reflectance sensed by Spectrolite during the measurement) have to be made.

## OUTLOOK

Several improvements could be made during the measurements and data processing to offer a better result in  $\text{NO}_2$  vertical column densities in further research.

First of all, the primary uncertainty in  $\text{NO}_2$  vertical column density retrieval is DAOS fitting which originates from the signal-to-noise ratio (SNR), which can be improved by increasing the CCD binning. However, the coarser spatial resolution caused by this binning might make it more difficult to distinguish the surface features that have been discussed previously. Furthermore, in this project, 24 adjacent pixels in along-track directions are combined to increase the signal-to-noise ratio during DOAS fit, for the same reason as CCD binning, the number of combined pixels can not be too large to maintain the ability to detect surface feature.

Subsequently, since we do not have the precise knowledge of the concentration over reference region (a rural area) for DOAS fitting, the comparisons (differential slant column density) are made with respect to a not well-known concentration which is retrieved by interpolation of OMI observation whose spatial resolution is relatively low for such small scale, resulting in uncertainty in the absolute vertical column density. In the future, flights can be supported by independent measurements (e.g. ground-base observations) over the reference region to obtain the precise absolute vertical column density.

In addition, the AMF uncertainty was difficult to ascertain with confidence, because there are more uncertainties regarding the input parameters used for DAK simulation. The majority of the AMF error is attribute to potential uncertainties in the  $\text{NO}_2$  profile height, aerosol profile height and the surface reflectance. Future flight campaigns should also aim at measuring  $\text{NO}_2$  and aerosol profiles which would valuably support the retrieval as well as the interpretation of the results. For  $\text{NO}_2$  and aerosol layer height, their vertical profiles can be retrieved simultaneously with Spectrolite measurements by using ground-base stations or balloons. It would also be optimistic if surface reflectance can be measured on board the aircraft where Spectrolite is installed. Finally,

Moreover, the Spectrolite geometry is dependent on the solar zenith angle, which causes stratospheric correction. The stratospheric correction has been made by applying only geometric air mass factor to OMI stratospheric vertical column density. A deduction in the influence of solar geometry could be realized if the measurements are conducted at noon in the summer where the solar zenith angle has smaller variation.

In conclusion, through the study of this graduation project, we can find that with airborne-based Spectrolite measurements, a high spatiotemporal variability of  $\text{NO}_2$  can be clearly revealed, allowing us to detect  $\text{NO}_2$  emission sources, obtain valuable inputs for  $\text{NO}_2$  emission modelling and understand the connection between  $\text{NO}_2$  measure-



ments and air quality models, which makes it possible to increase the knowledge on processes and characteristics of NO<sub>2</sub> tropospheric distribution as well as spatio-temporal NO<sub>2</sub> distribution.



# REFERENCES

- [1] M. Krzyzanowski. Who air quality guidelines for europe. *J Toxicol Environ Health A*, 71(1):47–50, 2008.
- [2] Kavi Kumar Khedo, Rajiv Perseedoss, and Avinash Mungur. A wireless sensor network air pollution monitoring system. *CoRR*, abs/1005.1737, 2010.
- [3] J. Philip Bromberg. *Clean Air Act handbook : "how to comply with the Clean Air Act"*. Government Institutes, Rockville, MD, 1983.
- [4] U.S. Environmental Protection Agency. *Integrated Science Assessment for Oxides of Nitrogen - Health Criteria (Final Report)*. National Center for Environmental Assessment, 2010.
- [5] WHO. Air quality guidelines, second edition. 2000.
- [6] K. L. Denman, G. Brasseur, A. Chidthaisong, P. Ciais, P. M. Cox, R. E. Dickinson, D. Hauglustaine, C. Heinze, E. Holland, D. Jacob, U. Lohmann, S. Ramachandran, P. L. da Silva Dias, S. C. Wofsy, and X. Zhang. Couplings between changes in the climate system and biogeochemistry. Report, Cambridge University Press, 2007.
- [7] J.P. Burrows, U. Platt, and P. Borrell. *The Remote Sensing of Tropospheric Composition from Space*. Physics of Earth and Space Environments. Springer Berlin Heidelberg, 2011.
- [8] C.O. Oriakhi. *Chemistry in Quantitative Language: Fundamentals of General Chemistry Calculations*. Oxford University Press, 2009.
- [9] S. C. Liew. *Principles of Remote Sensing*. 2001.
- [10] D. Loyola, W. Zimmer, S. Kiemle, P. Valks, and M. Pedernana. Gome product user manual. (2/E), 2012.
- [11] M. Gottwald and H. Bovensmann. *SCIAMACHY - Exploring the Changing Earth's Atmosphere*. Springer Netherlands, 2010.
- [12] SCIAMACHY Quality Working Group. Sciamachy product handbook, 2016.
- [13] OMI Team. Omi user's guide ozone monitoring instrument (omi) data user's guide. (OMI -DUG -5 .0), 2012.
- [14] Louisa J. Kramer, Roland J. Leigh, John J. Remedios, and Paul S. Monks. Comparison of omi and ground-based in situ and max-doas measurements of tropospheric nitrogen dioxide in an urban area. *Journal of Geophysical Research: Atmospheres*, 113(D16):n/a–n/a, 2008. D16S39.

- [15] G. Hönninger, C. von Friedeburg, and U. Platt. Multi axis differential optical absorption spectroscopy (max-doas). *Atmospheric Chemistry and Physics*, 4(1):231–254, 2004.
- [16] P. Wang, A. Richter, M. Bruns, V. V. Rozanov, J. P. Burrows, K.-P. Heue, T. Wagner, I. Pundt, and U. Platt. Measurements of tropospheric NO<sub>2</sub> with an airborne multi-axis doas instrument. *Atmospheric Chemistry and Physics*, 5(2):337–343, 2005.
- [17] Rainer M. Volkamer, Agency California Environmental Protection, Board Air Resources, Division Research, and Boulder University of Colorado. *AMAX-DOAS trace gas column observations from research aircraft over California*. 2014.
- [18] B.T.G. de Goeij, G.C.J. Otter, J.M.O. van Wakeren, J.P. Veeffkind, T. Vlemmix, X. Ge, P.F. Levelt, B.P.F. Dirks, P.M. Toet, and L.F. et al. van der Wal. *First Aircraft Test Results of a Compact, Low Cost Hyperspectral Imager for Earth Observation from Space*. 2016.
- [19] A glossary of spectroscopic terms - ocean optics, 2016.
- [20] Merlaud Magdalena, ArdeleanAlexis. Inter-comparison of airborne atmospheric imagers during the aromapex campaign, 2016.
- [21] C. Popp, D. Brunner, A. Damm, M. Van Roozendaal, C. Fayt, and B. Buchmann. High-resolution NO<sub>2</sub> remote sensing from the airborne prism experiment (apex) imaging spectrometer. *Atmospheric Measurement Techniques*, 5(9):2211–2225, 2012.
- [22] A. Schönhardt, P. Altube, K. Gerilowski, S. Krautwurst, J. Hartmann, A. C. Meier, A. Richter, and J. P. Burrows. A wide field-of-view imaging doas instrument for two-dimensional trace gas mapping from aircraft. *Atmospheric Measurement Techniques*, 8(12):5113–5131, 2015.
- [23] A. Merlaud, F. Tack, D. Constantin, C. Fayt, J. Maes, F. Mingireanu, I. Mocanu, L. Georgescu, and M. Van Roozendaal. Small Whiskbroom Imager for atmospheric composition monitorinG (SWING) from an Unmanned Aerial Vehicle (UAV): Results from the 2014 AROMAT campaign. In *EGU General Assembly Conference Abstracts*, volume 17 of *EGU General Assembly Conference Abstracts*, page 12499, April 2015.
- [24] A. Merlaud, F. Tack, and M. van Roozendaal. The aromapex campaign, 2016.
- [25] M. Bruns, S. A. Buehler, J. P. Burrows, A. Richter, A. Rozanov, P. Wang, K. P. Heue, U. Platt, I. Pundt, and T. Wagner. NO<sub>2</sub> profile retrieval using airborne multi axis uv-visible skylight absorption measurements over central europe. *Atmospheric Chemistry and Physics*, 6(10):3049–3058, 2006.
- [26] U. Platt and J. Stutz. *Differential Optical Absorption Spectroscopy: Principles and Applications*. Physics of Earth and Space Environments. Springer Berlin Heidelberg, 2008.

- [27] M. Gargaud, R. Amils, and H.J. Cleaves. *Encyclopedia of Astrobiology*. Number v. 3 in *Encyclopedia of Astrobiology*. Springer, 2011.
- [28] University of Colorado Boulder Volkamer Group. Differential optical absorption spectroscopy (doas), 2016.
- [29] The Atmospheric Trace Molecule Spectroscopy Laboratory (ATMOSpeclab) Volkamer Research Group. Differential optical absorption spectroscopy (doas), 2016.
- [30] V. Gold, International Union of Pure, and Applied Chemistry. *Compendium of Chemical Terminology: IUPAC Recommendations*. Professional and industrial computing series. Blackwell Scientific Publications, 1987.
- [31] T. Wagner, J. P. Burrows, T. Deutschmann, B. Dix, C. von Friedeburg, U. Frieß, F. Hendrick, K.-P. Heue, H. Irie, H. Iwabuchi, Y. Kanaya, J. Keller, C. A. McLinden, H. Oetjen, E. Palazzi, A. Petritoli, U. Platt, O. Postlyakov, J. Pukite, A. Richter, M. van Roozendael, A. Rozanov, V. Rozanov, R. Sinreich, S. Sanghavi, and F. Wittrock. Comparison of box-air-mass-factors and radiances for multiple-axis differential optical absorption spectroscopy (max-doas) geometries calculated from different uv/visible radiative transfer models. *Atmospheric Chemistry and Physics*, 7(7):1809–1833, 2007.
- [32] J. Z. Ma, S. Beirle, J. L. Jin, R. Shaiganfar, P. Yan, and T. Wagner. Tropospheric NO<sub>2</sub> vertical column densities over beijing: results of the first three years of ground-based max-doas measurements (2008-2011) and satellite validation. *Atmospheric Chemistry and Physics*, 13(3):1547–1567, 2013.
- [33] Susan Solomon, Arthur L. Schmeltekopf, and Ryan W. Sanders. On the interpretation of zenith sky absorption measurements. *Journal of Geophysical Research: Atmospheres (1984–2012)*, 92(D7):8311–8319, 7 1987.
- [34] J. Lenoble. *Radiative Transfer in Scattering and Absorbing Atmospheres: Standard Computational Procedures*. Studies in geophysical optics and remote sensing. A. Deepak, 1985.
- [35] Tim Vlemmix. *Tropospheric nitrogen dioxide inversions based on spectral measurements of scattered sunlight*. Eindhoven : Technische Universiteit Eindhoven, 2011.
- [36] E.F. Vermote, D. Tanre, J.L. Deuze, M. Herman, and J.-J. Morcrette. Second simulation of the satellite signal in the solar spectrum, 6s: an overview. *IEEE Transactions on Geoscience and Remote Sensing*, 35(3):675–686, 1997.
- [37] A.V. Rozanov, V.V. Rozanov. *User's Guide for the Software Package SCIATRAN (Radiative Transfer Model and Retrieval Algorithm)*. Institute of Remote Sensing, University of Bremen, 3 edition, 2016.
- [38] E. Vermote, D. Tanré, J. L. Deuzé, M. Herman, J. J. Morcrette, and S. Y. Kotchenova. *6S User Guide*. Laboratoire d'Optique Atmosphérique, 3 edition, 2016.

- [39] J. P. Lawrence, J. S. Anand, J. D. Vande Hey, J. White, R. R. Leigh, P. S. Monks, and R. J. Leigh. High-resolution measurements from the airborne atmospheric nitrogen dioxide imager (andi). *Atmospheric Measurement Techniques*, 8(11):4735–4754, 2015.
- [40] J. F. de Haan, P. B. Bosma, and J. W. Hovenier. The adding method for multiple scattering calculations of polarized light. 183:371–391, September 1987.
- [41] J.P. BURROWS, A. RICHTER, A. DEHN, B. DETERS, S. HIMMELMANN, S. VOIGT, and J. ORPHAL. Atmospheric remote-sensing reference data from gome—2. temperature-dependent absorption cross sections of o<sub>3</sub> in the 231–794nm range. *Journal of Quantitative Spectroscopy and Radiative Transfer*, 61(4):509 – 517, 1999.
- [42] Ann Carine Vandaele, Christian Hermans, Paul C Simon, Michel Carleer, Réginald Colin, Sophie Fally, Marie-France Merienne, Alain Jenouvrier, and Bernard Coquart. Measurements of the no<sub>2</sub> absorption cross-section from 42 000 cm<sup>-1</sup> to 10 000 cm<sup>-1</sup> (238–1000 nm) at 220 k and 294 k. *Journal of Quantitative Spectroscopy and Radiative Transfer*, 59(3):171–184, 1998.
- [43] Eric F. Vermote. Atmospheric effect in the solar spectrum, 2015.
- [44] Palanisamy Shanmugam Rakesh Kumar Singh. A novel method for estimation of aerosol radiance and its extrapolation in the atmospheric correction of satellite data over optically complex oceanic waters. *Remote Sensing of Environment*, 142:188 – 206, 2014.
- [45] C Mobley, E Boss, and C Roesler. Ocean optics web book, 2010.
- [46] A.C. Vandaele, C. Hermans, S. Fally, M. Carleer, M.-F. Mérienne, A. Jenouvrier, B. Coquart, and R. Colin. Absorption cross-sections of no<sub>2</sub>: simulation of temperature and pressure effects. *Journal of Quantitative Spectroscopy and Radiative Transfer*, 76(3–4):373 – 391, 2003.
- [47] E. Spinei, A. Cede, W. H. Swartz, J. Herman, and G. H. Mount. The use of no<sub>2</sub> absorption cross section temperature sensitivity to derive no<sub>2</sub> profile temperature and stratospheric–tropospheric column partitioning from visible direct-sun doas measurements. *Atmospheric Measurement Techniques*, 7(12):4299–4316, 2014.
- [48] NASA Glen Research Center, 2016.
- [49] K. Chance and R.L. Kurucz. An improved high-resolution solar reference spectrum for earth’s atmosphere measurements in the ultraviolet, visible, and near infrared. 2010.

# A

## VISUALIZATION OF SCALED SURFACE REFLECTANCE

The retrieved surface reflectance after vicarious calibration under different aerosol layer height scenarios (0.2km, 0.5km, 0.8km, 1.6km) in the morning and afternoon.

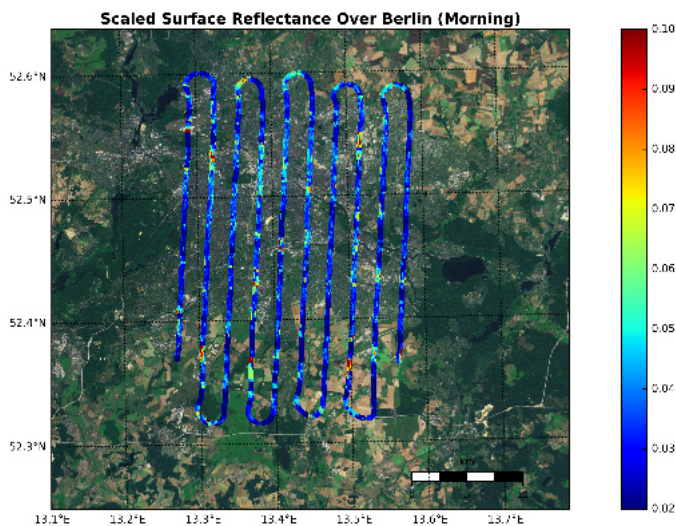


Figure A.1: Scaled surface reflectance retrieved after vicarious calibration with 0.2km aerosol layer height over Berlin in the morning on 21 April, 2016

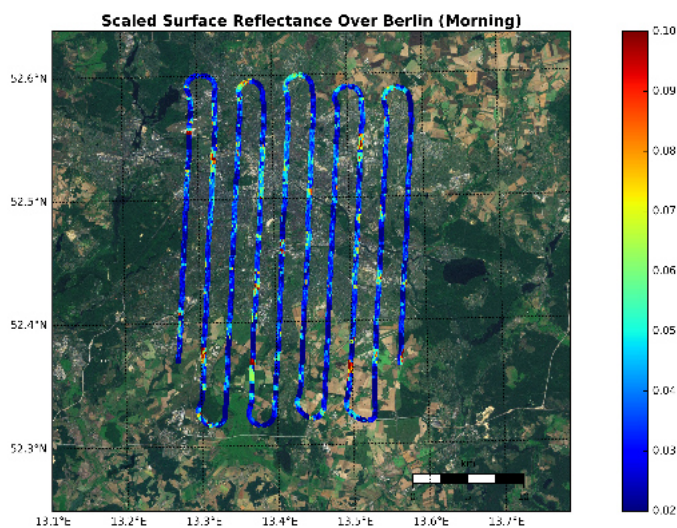


Figure A.2: Scaled surface reflectance retrieved after vicarious calibration with 0.5 km aerosol layer height over Berlin in the morning on 21 April, 2016

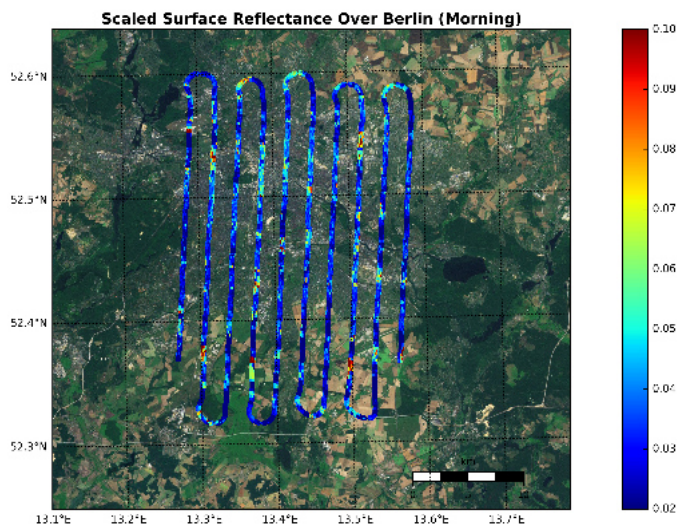


Figure A.3: Scaled surface reflectance retrieved after vicarious calibration with 0.8 km aerosol layer height over Berlin in the morning on 21 April, 2016



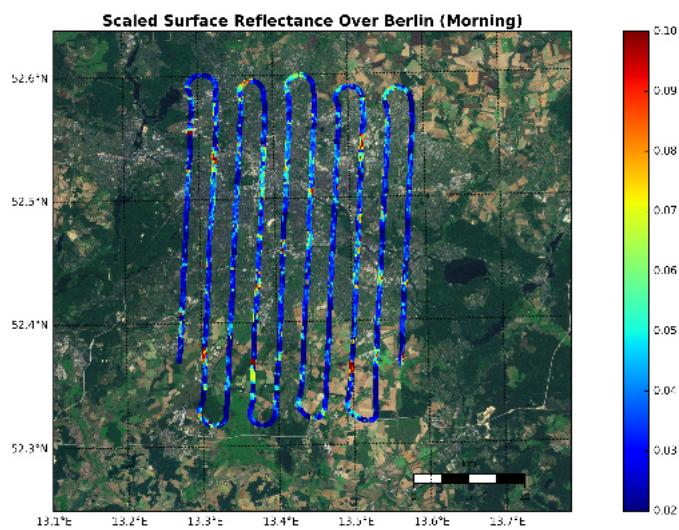


Figure A.4: Scaled surface reflectance retrieved after vicarious calibration with 1.6km aerosol layer height over Berlin in the morning on 21 April, 2016

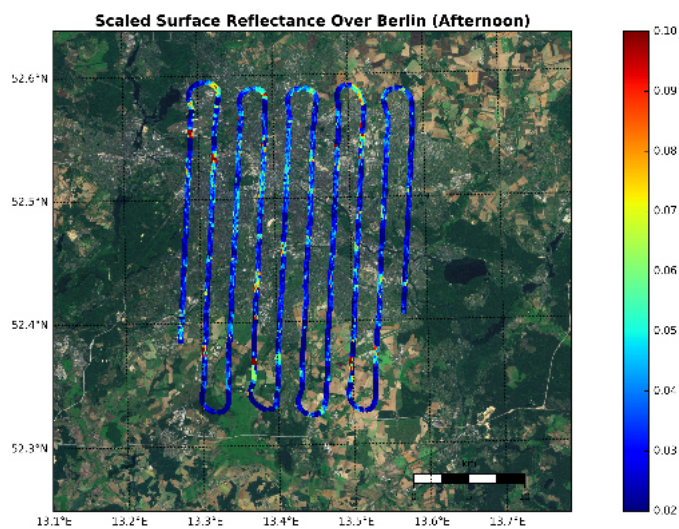


Figure A.5: Scaled surface reflectance retrieved after vicarious calibration with 0.2km aerosol layer height over Berlin in the afternoon on 21 April, 2016

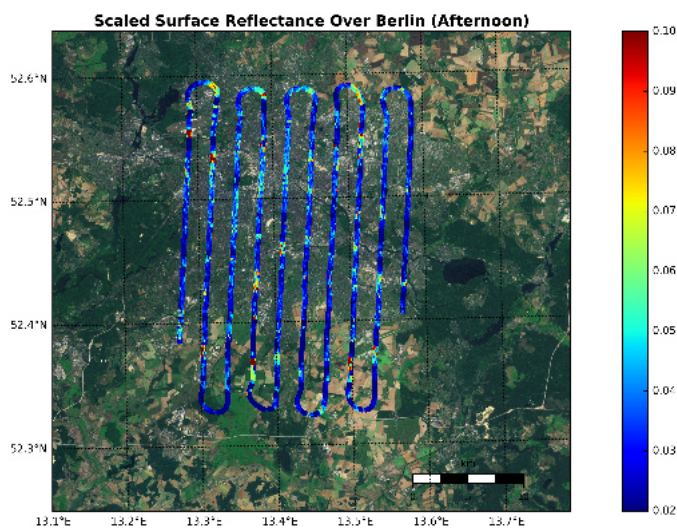


Figure A.6: Scaled surface reflectance retrieved after vicarious calibration with 0.5 km aerosol layer height over Berlin in the afternoon on 21 April, 2016

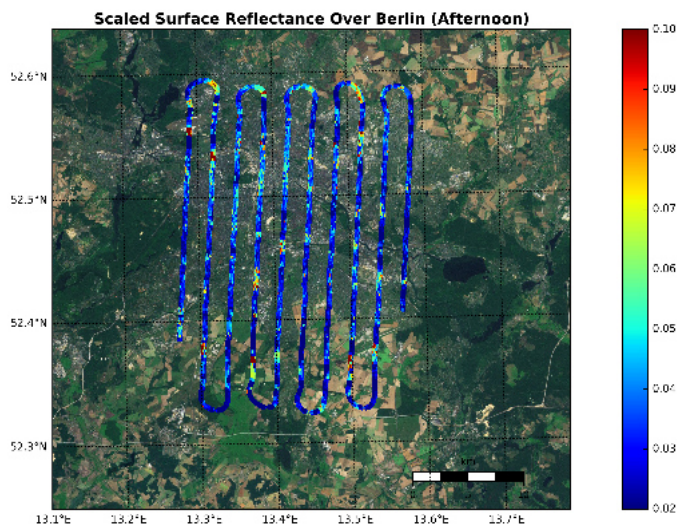


Figure A.7: Scaled surface reflectance retrieved after vicarious calibration with 0.8 km aerosol layer height over Berlin in the afternoon on 21 April, 2016

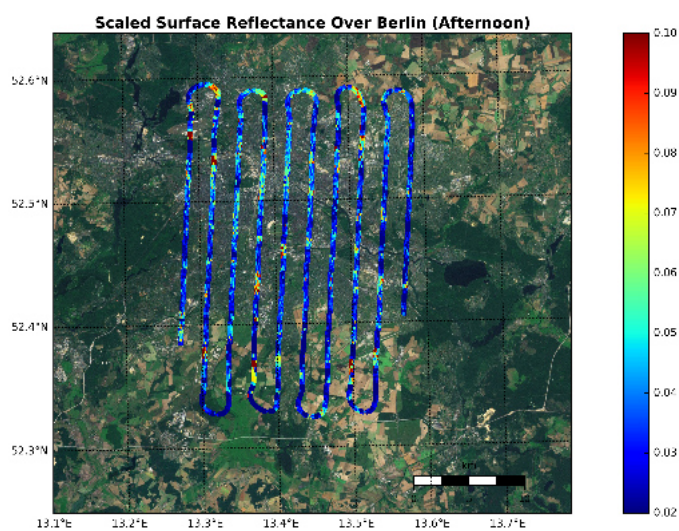


Figure A.8: Scaled surface reflectance retrieved after vicarious calibration with 1.6km aerosol layer height over Berlin in the afternoon on 21 April, 2016



# B

## VISUALIZATION OF AIR MASS FACTOR

The obtained air mass factor under different aerosol layer height scenarios (0.2km, 0.5km, 0.8km, 1.6km) and NO<sub>2</sub> profile height conditions (half of or the same as aerosol layer height) in the morning and afternoon.

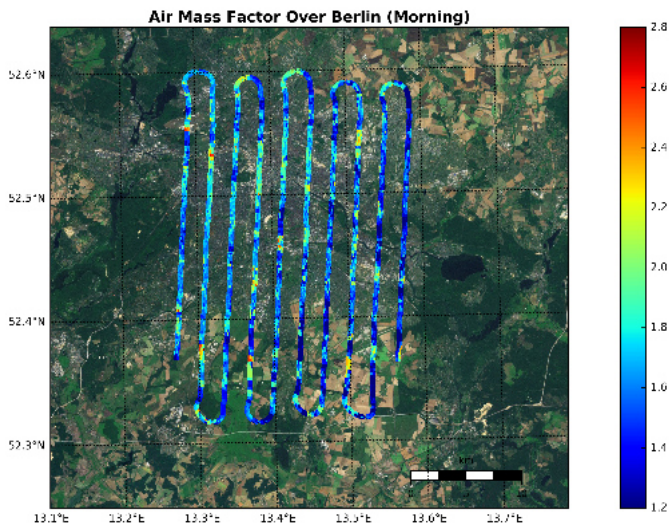


Figure B.1: Air mass factor under scenario with 0.2km aerosol layer height and 0.1km NO<sub>2</sub> profile height over Berlin in the morning on 21 April, 2016



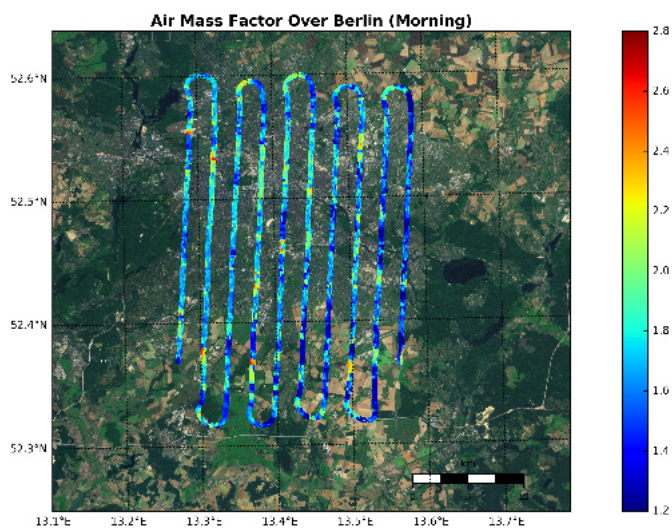


Figure B.2: Air mass factor under scenario with 0.2km aerosol layer height and 0.2km NO<sub>2</sub> profile height over Berlin in the morning on 21 April, 2016

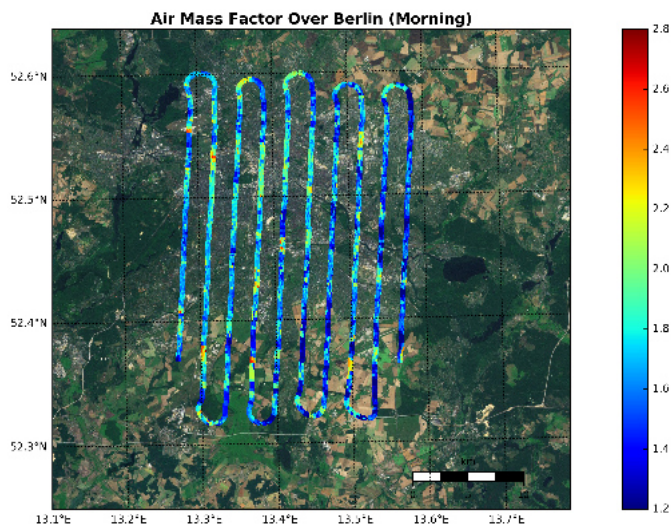


Figure B.3: Air mass factor under scenario with 0.5km aerosol layer height and 0.25km NO<sub>2</sub> profile height over Berlin in the morning on 21 April, 2016

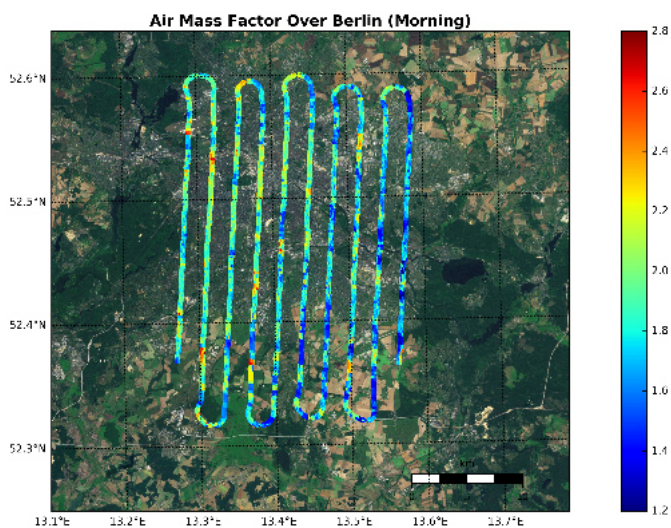


Figure B.4: Air mass factor under scenario with 0.5km aerosol layer height and 0.5km NO<sub>2</sub> profile height over Berlin in the morning on 21 April, 2016

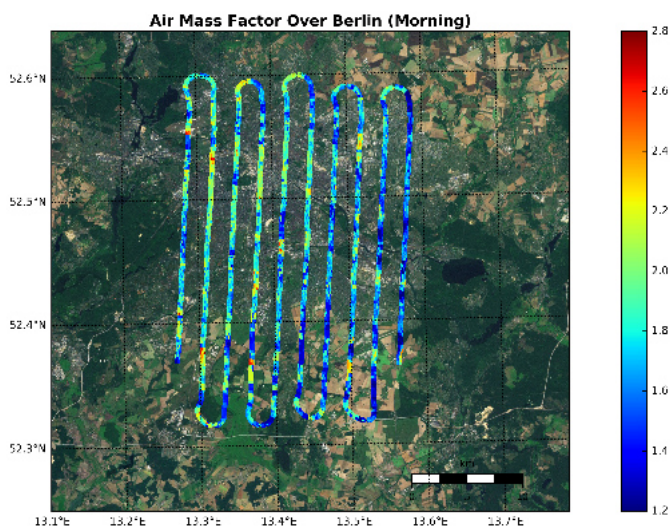


Figure B.5: Air mass factor under scenario with 0.8km aerosol layer height and 0.4km NO<sub>2</sub> profile height over Berlin in the morning on 21 April, 2016

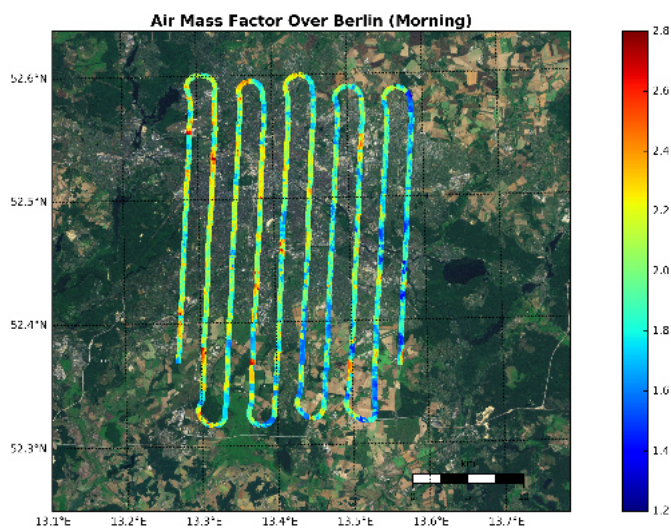


Figure B.6: Air mass factor under scenario with 0.8km aerosol layer height and 0.8km NO<sub>2</sub> profile height over Berlin in the morning on 21 April, 2016

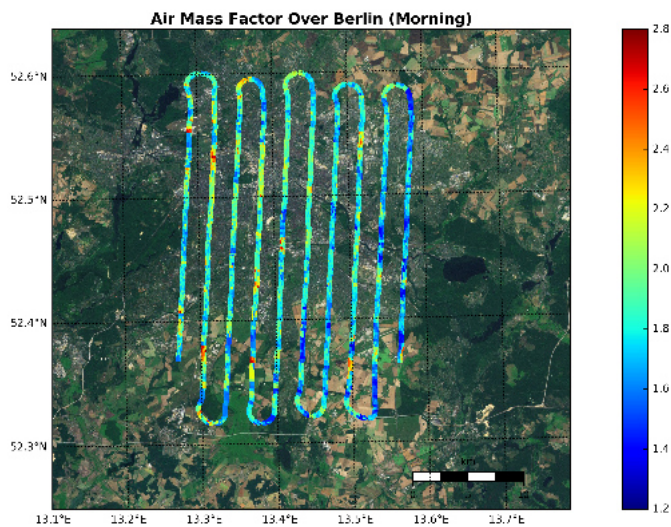


Figure B.7: Air mass factor under scenario with 1.6km aerosol layer height and 0.8km NO<sub>2</sub> profile height over Berlin in the morning on 21 April, 2016



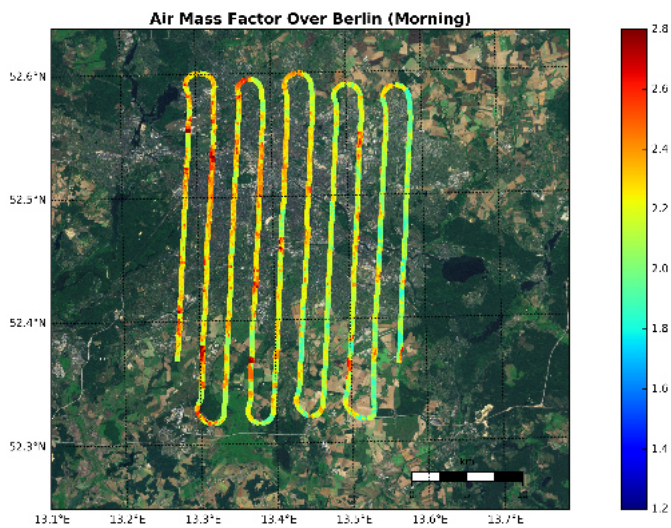


Figure B.8: Air mass factor under scenario with 1.6km aerosol layer height and 1.6km NO<sub>2</sub> profile height over Berlin in the morning on 21 April, 2016

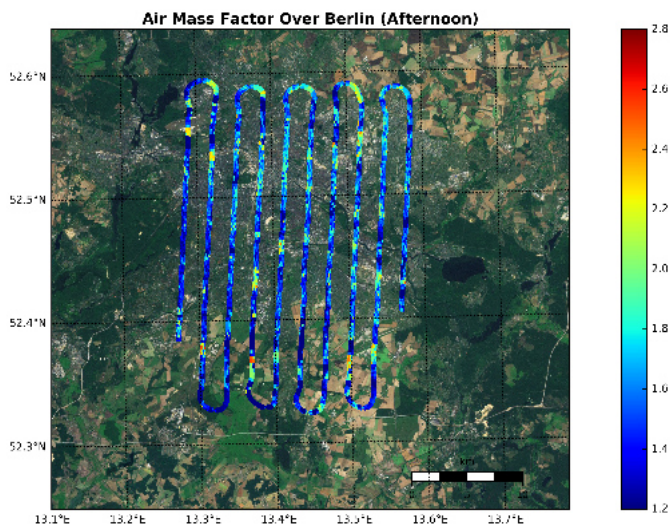


Figure B.9: Air mass factor under scenario with 0.2km aerosol layer height and 0.1km NO<sub>2</sub> profile height over Berlin in the afternoon on 21 April, 2016

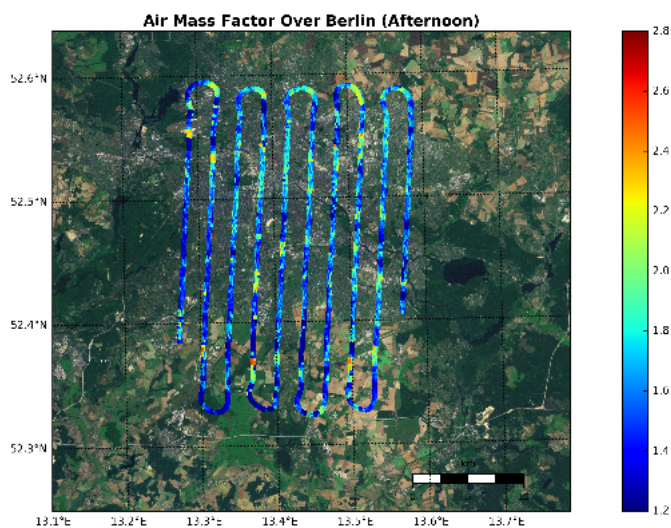


Figure B.10: Air mass factor under scenario with 0.2km aerosol layer height and 0.2km NO<sub>2</sub> profile height over Berlin in the afternoon on 21 April, 2016

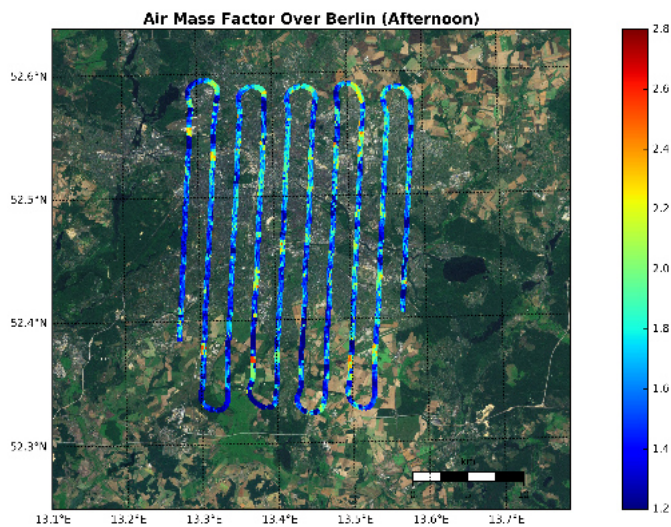


Figure B.11: Air mass factor under scenario with 0.5km aerosol layer height and 0.25km NO<sub>2</sub> profile height over Berlin in the afternoon on 21 April, 2016

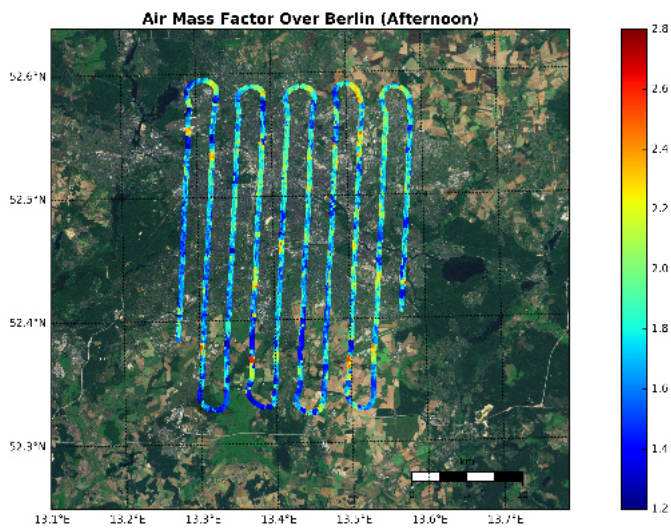


Figure B.12: Air mass factor under scenario with 0.5km aerosol layer height and 0.5km NO<sub>2</sub> profile height over Berlin in the afternoon on 21 April, 2016

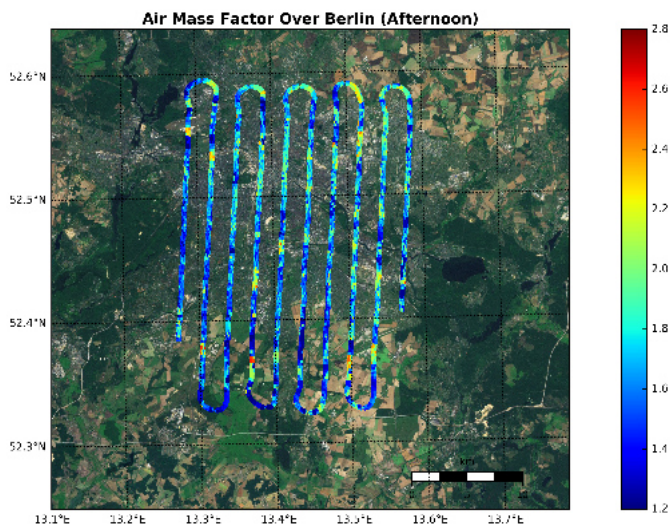


Figure B.13: Air mass factor under scenario with 0.8km aerosol layer height and 0.4km NO<sub>2</sub> profile height over Berlin in the afternoon on 21 April, 2016



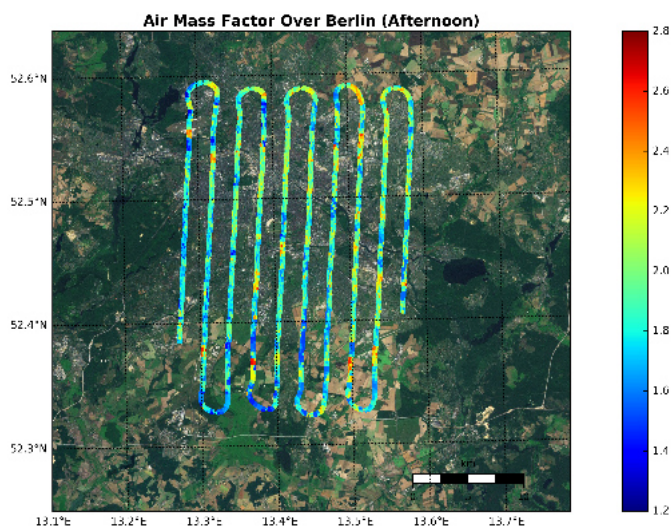


Figure B.14: Air mass factor under scenario with 0.8km aerosol layer height and 0.8km NO<sub>2</sub> profile height over Berlin in the afternoon on 21 April, 2016

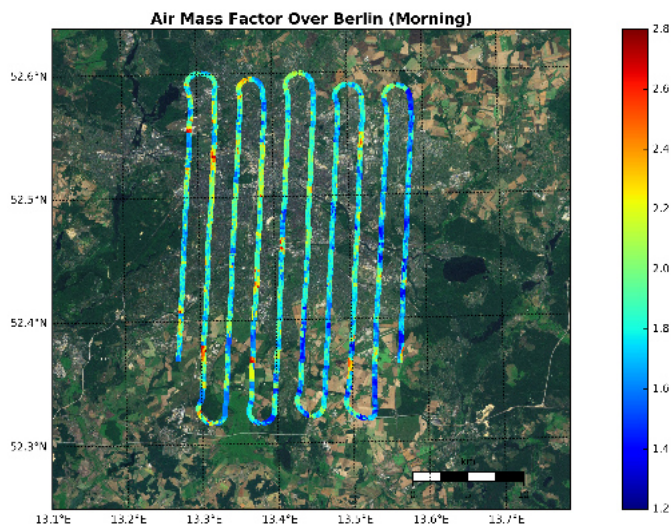


Figure B.15: Air mass factor under scenario with 1.6km aerosol layer height and 0.8km NO<sub>2</sub> profile height over Berlin in the afternoon on 21 April, 2016

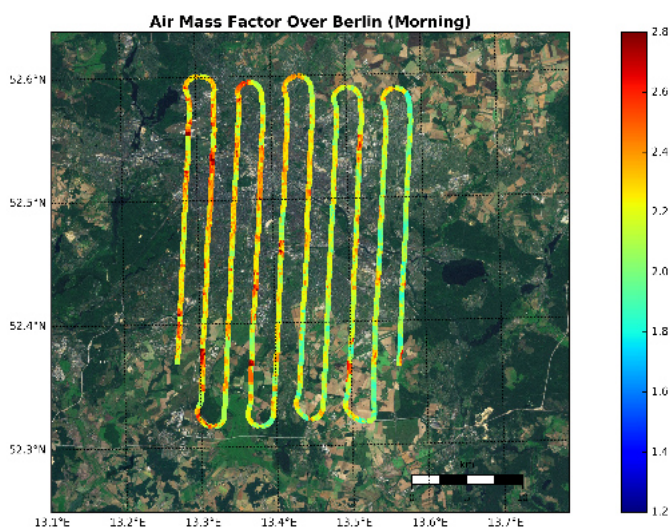


Figure B.16: Air mass factor under scenario with 1.6km aerosol layer height and 1.6km NO<sub>2</sub> profile height over Berlin in the afternoon on 21 April, 2016



# C

## VISUALIZATION OF NO<sub>2</sub> VERTICAL COLUMN DENSITY

The final product tropospheric NO<sub>2</sub> vertical column density under different aerosol layer height scenarios (0.2km, 0.5km, 0.8km, 1.6km) and NO<sub>2</sub> profile height conditions (half of or the same as aerosol layer height) in the morning and afternoon.

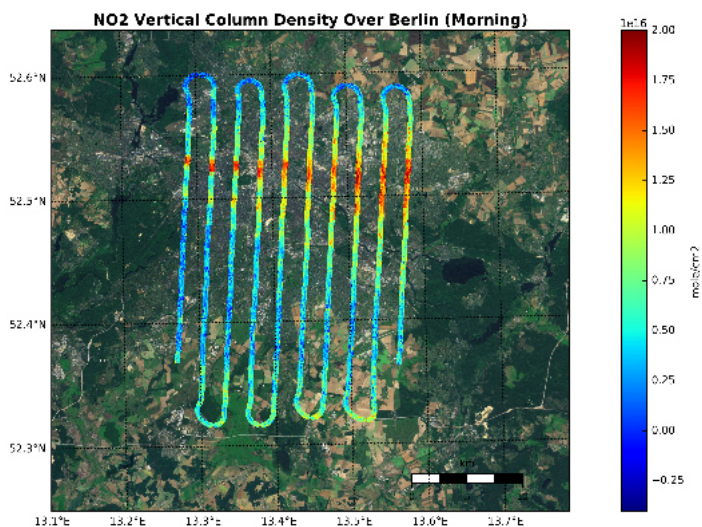


Figure C.1: NO<sub>2</sub> vertical column density under scenario with 0.2km aerosol layer height and 0.1km NO<sub>2</sub> profile height over Berlin in the morning on 21 April, 2016

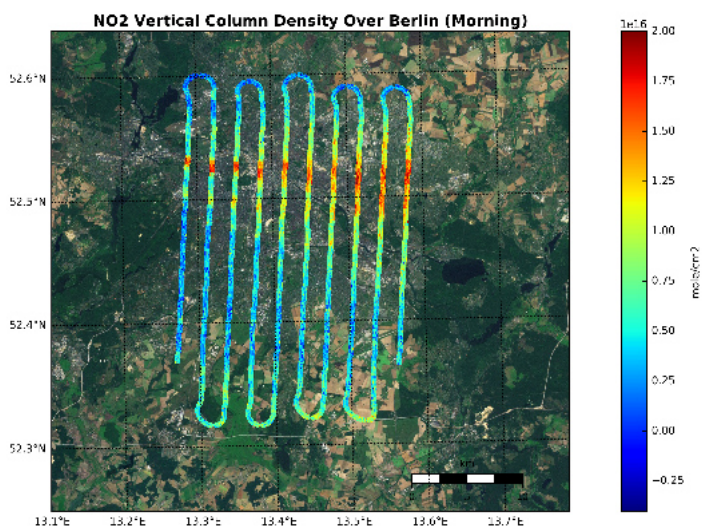


Figure C.2: NO<sub>2</sub> vertical column density under scenario with 0.2km aerosol layer height and 0.2km NO<sub>2</sub> profile height over Berlin in the morning on 21 April, 2016

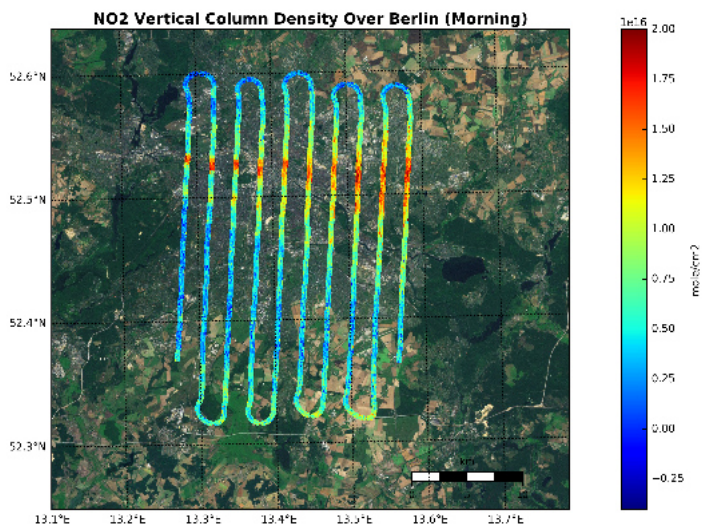


Figure C.3: NO<sub>2</sub> vertical column density under scenario with 0.5km aerosol layer height and 0.25km NO<sub>2</sub> profile height over Berlin in the morning on 21 April, 2016



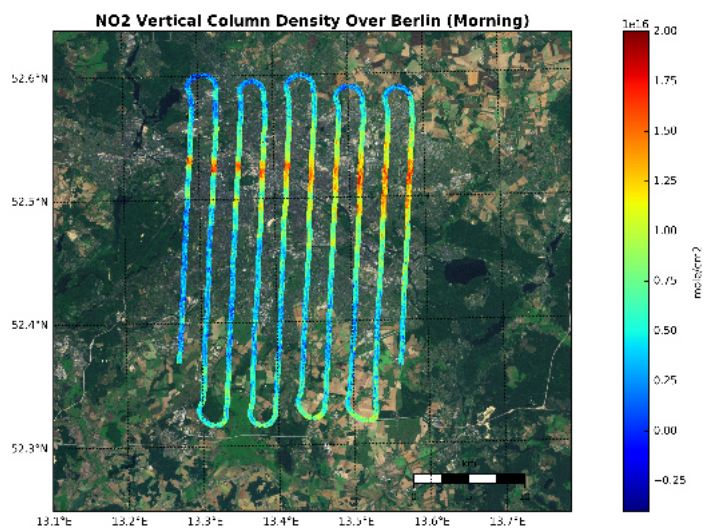


Figure C.4: NO<sub>2</sub> vertical column density under scenario with 0.5km aerosol layer height and 0.5km NO<sub>2</sub> profile height over Berlin in the morning on 21 April, 2016

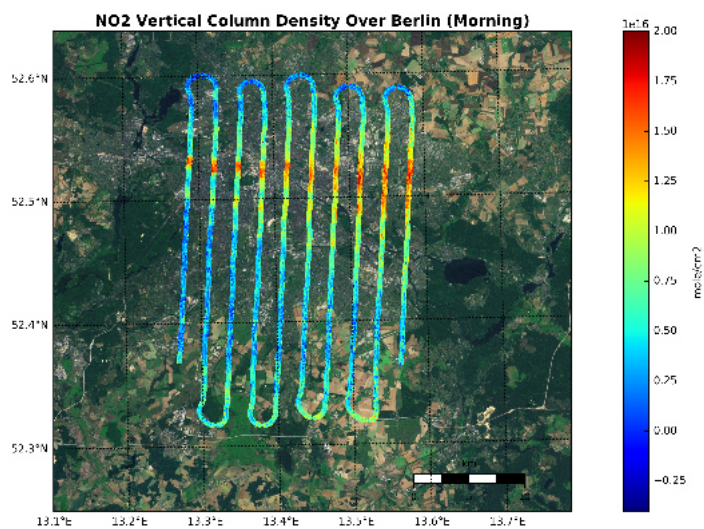


Figure C.5: NO<sub>2</sub> vertical column density under scenario with 0.8km aerosol layer height and 0.4km NO<sub>2</sub> profile height over Berlin in the morning on 21 April, 2016

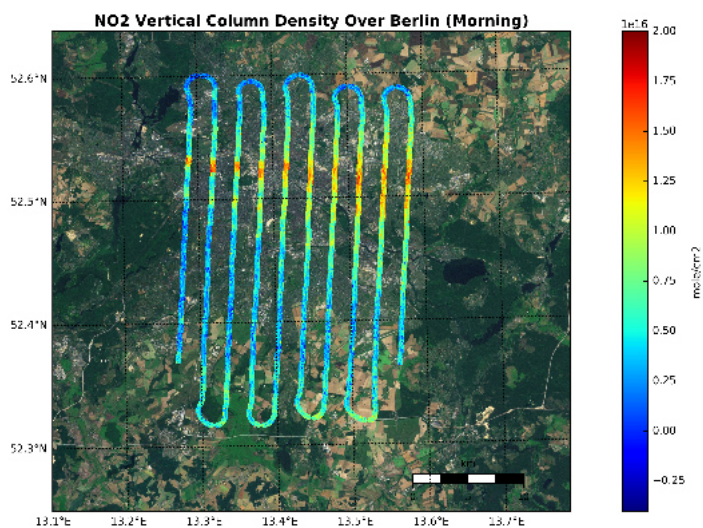


Figure C.6: NO<sub>2</sub> vertical column density under scenario with 0.8km aerosol layer height and 0.8km NO<sub>2</sub> profile height over Berlin in the morning on 21 April, 2016

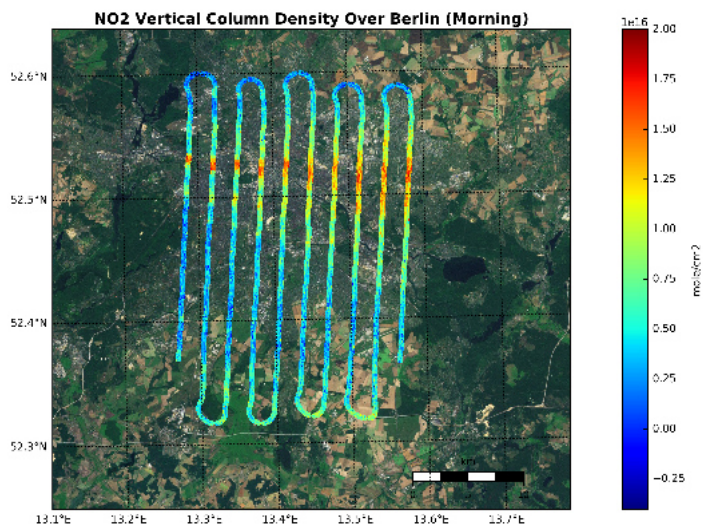


Figure C.7: NO<sub>2</sub> vertical column density under scenario with 1.6km aerosol layer height and 0.8km NO<sub>2</sub> profile height over Berlin in the morning on 21 April, 2016

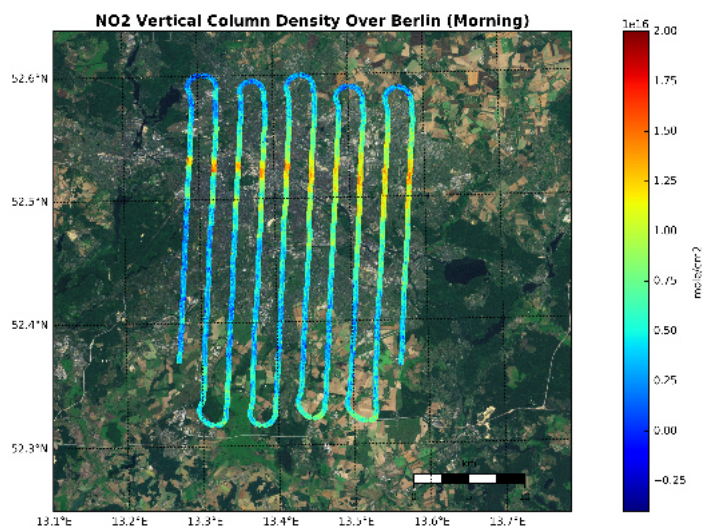


Figure C.8: NO<sub>2</sub> vertical column density under scenario with 1.6km aerosol layer height and 1.6km NO<sub>2</sub> profile height over Berlin in the morning on 21 April, 2016

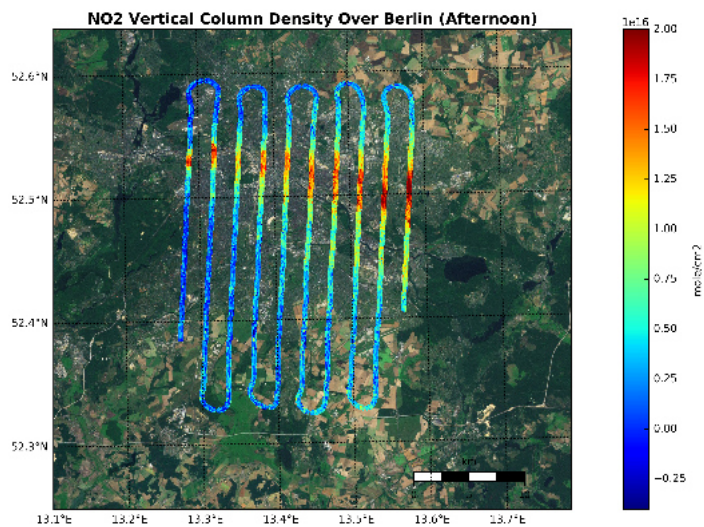


Figure C.9: NO<sub>2</sub> vertical column density under scenario with 0.2km aerosol layer height and 0.1km NO<sub>2</sub> profile height over Berlin in the afternoon on 21 April, 2016



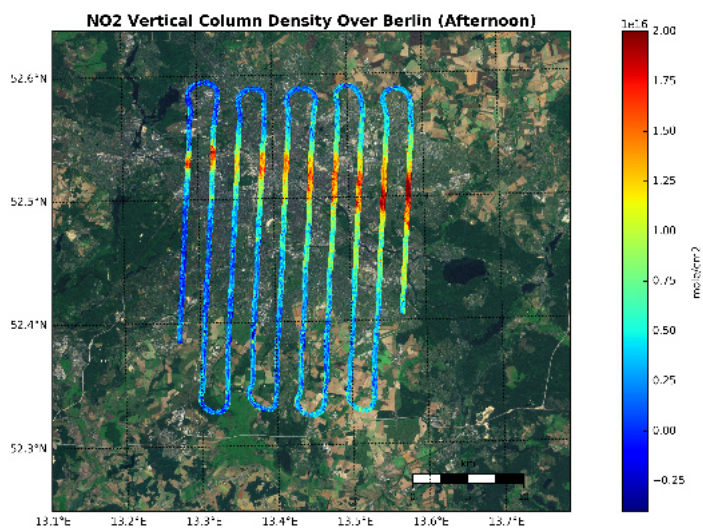


Figure C.10: NO<sub>2</sub> vertical column density under scenario with 0.2km aerosol layer height and 0.2km NO<sub>2</sub> profile height over Berlin in the afternoon on 21 April, 2016

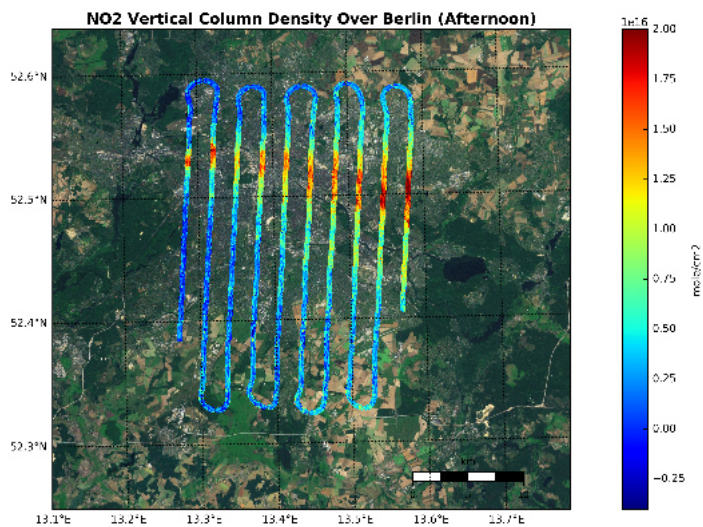


Figure C.11: NO<sub>2</sub> vertical column density under scenario with 0.5km aerosol layer height and 0.25km NO<sub>2</sub> profile height over Berlin in the afternoon on 21 April, 2016

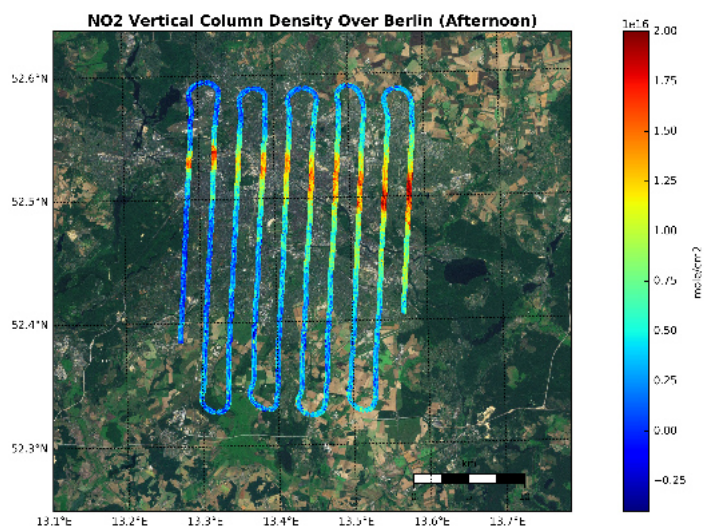


Figure C.12: NO<sub>2</sub> vertical column density under scenario with 0.5km aerosol layer height and 0.5km NO<sub>2</sub> profile height over Berlin in the afternoon on 21 April, 2016

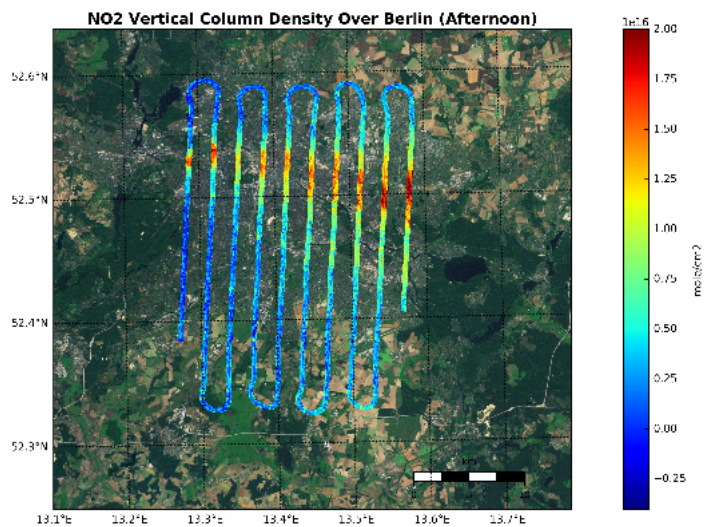


Figure C.13: NO<sub>2</sub> vertical column density under scenario with 0.8km aerosol layer height and 0.4km NO<sub>2</sub> profile height over Berlin in the afternoon on 21 April, 2016

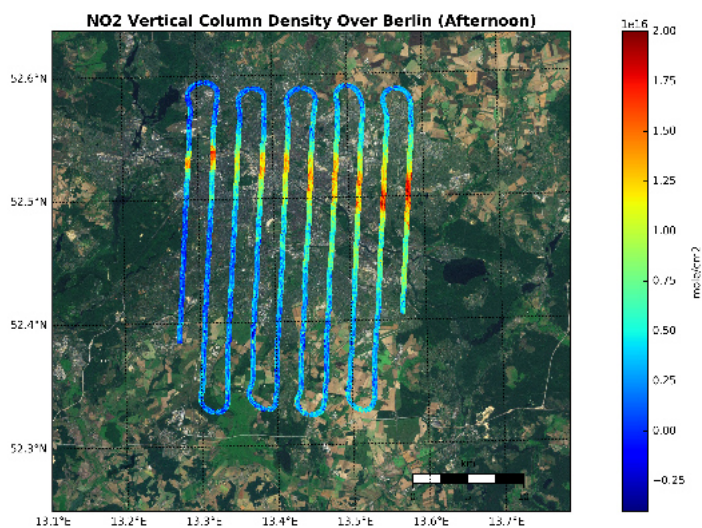


Figure C.14: NO<sub>2</sub> vertical column density under scenario with 0.8km aerosol layer height and 0.8km NO<sub>2</sub> profile height over Berlin in the afternoon on 21 April, 2016

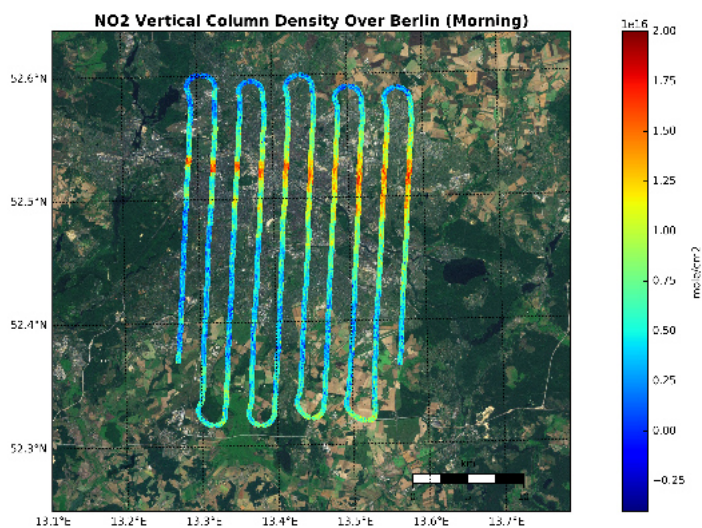


Figure C.15: NO<sub>2</sub> vertical column density under scenario with 1.6km aerosol layer height and 0.8km NO<sub>2</sub> profile height over Berlin in the afternoon on 21 April, 2016



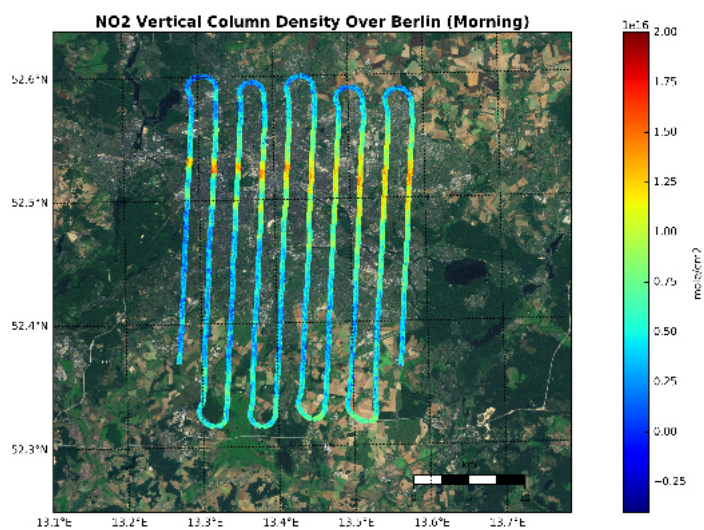


Figure C.16: NO<sub>2</sub> vertical column density under scenario with 1.6km aerosol layer height and 1.6km NO<sub>2</sub> profile height over Berlin in the afternoon on 21 April, 2016